Freie Universität Berlin

Structural Investigation of Amyloid Oligomers

via

IM-MS and Infrared-Spectroscopy

Master Thesis

accomplished
at the Institute of Chemistry and Biochemistry
Freie Universität Berlin

and the Fritz Haber Institute of the Max Planck Society
(Berlin, Germany)

Sebastian Malerz (B. Sc.)

Berlin, 13.04.2017

Accomplished in the time from

05.09.2016 - 13.04.2017

First Examiner: Prof. Dr. Kevin Pagel
Second Examiner: Prof. Dr. Beate Koksch

Advisor: Waldemar Hoffmann (M. Sc.), Ph. D. student

Statutory Declaration

I, Sebastian Malerz, born February 3, 1987 in Lutherstadt Wittenberg, confirm that I have prepared the master thesis "Structural Investigation of Amyloid Oligomers *via* IM-MS and Infrared-Spectroscopy" independently and entirely by myself using only the referred sources and support. I additionally assert that this thesis has not been part of another examination process.

Berlin, 13rd April 2017

_____

Sebastian Malerz

Abstract

A hallmark of the Alzheimer´s disease (AD) is the spontaneous transition of Abeta peptides from soluble, unstructured monomers into insoluble amyloid fibrils. Recent evidences increasingly suggest that not the mature fibrils but rather polydisperse Abeta 42 oligomers represent the toxic species. H/D exchange experiments, which rely on the solvent accessibility, have shown that especially the central hydrophobic core as well as the C-terminus are highly involved in the aggregation cascade. Furthermore, the Abeta 42 peptide, which just differs in two additional C-terminal amino acids, is more cytotoxic than the Abeta 40. A fundamental understanding of all involved structures is crucial for the development of effective drugs. Traditional condensed-phase methods, however, only provide averaged information of the assembly. On the other hand, gas-phase techniques are able to isolate and characterize one species in the presence of many others without affecting their underlying equilibrium. Especially, ion mobility-mass spectrometry (IM-MS) is routinely applied for the structural characterization of amyloid oligomers. It provides information on the ion´s shape and size and it can further serve as a filter for a subsequent analysis by orthogonal methods such as infrared (IR) spectroscopy. IR spectroscopy depends on intramolecular vibrations and is therefore highly sensitive towards the secondary structure, adopted by proteins and peptides. The combination of IM-MS and IR spectroscopy therefore allows to obtain tertiary/quaternary as well as secondary structure information of individual oligomers. In this thesis, fragments derived from the central hydrophobic core and the C-terminus of the Abeta peptide as well as the full-length Abeta 40 and Abeta 42 peptides were investigated. The data show that the last alanine residue (Ala 42) play the most important role for the aggregation into β-sheet rich aggregates. Both full-length Abeta monomers and the Abeta 40 dimer adopt turn-like conformations in the gas phase and therefore the characteristic transition into highly structured aggregates occurs through higher oligomers.

Acknowledgement/Danksagung

Ein besonderer Dank gilt meinen Eltern, die mich nicht nur während meiner Schul- und Ausbildungszeit, sondern auch während meines gesamten Studiums ausnahmslos und liebevoll unterstützten und immer für mich da sind.

Mein größter Dank geht an meine Ehefrau, Patricia Malerz, die mich stets mit Liebe und Hingabe unterstützt, mir Rückhalt während des gesamten Studiums gab, viel Verständnis zeigte und mich mit motivierenden und hilfreichen Worten seelisch und moralisch aufbaute.

Table of Contents

1. Introduction

More than 20 neurodegenerative disorders such as Parkinson´s and Alzheimer´s disease are the result of misfolded peptides.[1-5] The peptide monomers undergo a spontaneous transition from soluble, partially folded structures to transient intermediates to insoluble so-called amyloid fibrils (plaques). Although those amyloidogenic plaques are found in the brain cortex of Alzheimer patients, new studies show that early, soluble oligomeric intermediates represent the toxic species.[4] The structural characterization of those transient amyloidogenic intermediates is challenging due to their polydisperse behavior. Instead of adopting one defined oligomeric state, they form different oligomeric sizes (dimer, trimer, hexamer etc.). In addition, they are also polymorph, i.e. several conformers coexist for the same oligomeric state. This polydisperse and polymorphic nature makes their characterization by traditional condensed-phase methods very challenging, because those methods only provide an average result of all species in the probed sample.[2] Soft ionization methods, however, are capable of transferring those large biomolecules in the gas phase, whereby covalent bonds and non-covalent complexes remain intact.[6-8] Gas-phase methods, such as ion mobility spectrometry (IMS), separate oligomers based on their charge, size and shape, and can be coupled to mass spectrometry (MS), which further allows to disentangle polydisperse and polymorphic species based on their mass.[9] Although ion mobility-mass spectrometry (IM-MS) provides information about the overall shape of the oligomers, it gives no information about secondary structure motifs. To overcome this problem, IM-MS can be used as a preselection tool to perform secondary structure sensitive IR spectroscopy in the gas phase on conformer and *m/z* selected species. Especially the vibration mode of the backbone carbonyl groups (amide I band) are very sensitive for secondary structure motifs adopted by peptides and proteins.[3, 10, 11]

In this thesis, the structural morphology of several fragments of Abeta 40 and 42, which are the main actors in Alzheimer´s disease, were investigated. Traditional condensed-phase as well as elaborate gas-phase structural analytical techniques were employed to study the structural origin of their aggregation behavior.

2. Amyloid and its Definition

In 19th century the German scientist and pathologist Rudolph Virchow investigated brain and spinal cord tissues of humans suffering from memory loss. During this investigations he discovered abnormal macroscopic deposits that exhibit a positive iodine straining similar to starch (lat. amylum).[12] Based on this observation, he concluded that the major component of these deposits is cellulose and therefore he introduced the term "amyloid". Later, Friedreich and Kékulé performed an elemental analysis of those deposits and observed a nitrogen content up to 15 %.[13] Carbohydrates are, however, mainly composed of the elements hydrogen, carbon and oxygen, which cannot explain such high nitrogen content. Consequently, Friedreich and Kékulé suggested that the major components of these deposits are proteins and peptides, which was later confirmed.[14, 15]

Pathologists describe amyloids as unbranched fibers, which are present in extracellular tissues *in vivo*. In addition, these fibrils must be able to bind the dye Congo Red, which leads to an unique green birefringence (shown in Figure 1).[16] These criteria are, however, only fulfilled for ~25 proteins associated with neurodegenerative disorders like Parkinson´s and Alzheimer´s disease.[12, 17] Despite the vast difference in size and sequence, in principle all peptides and proteins are able to form amyloids under certain conditions *in vitro*.[2] Thus, biophysics refer to amyloids, when they show the characteristic cross-β fiber diffraction pattern in X-ray diffraction experiments (XRD) (Figure 2).[17]
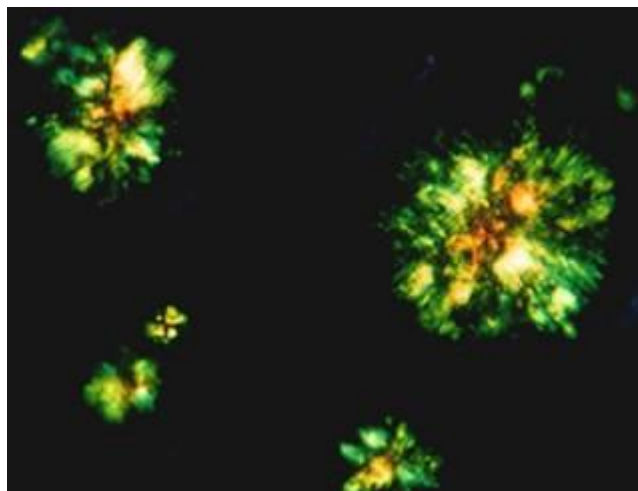
Figure 1: Congo Red stained brain tissue of an Alzheimer patient. Stained fibrils show a characteristic green birefringence under polarized light.[16]

This pattern was first observed by Astbury ET AL. in 1935, during the overlap of a denaturized egg white with an X-ray beam.[18] Moreover, it is also observed for other amyloid fibrils.[17, 18] The pattern showed a weak vertical and strong horizontal diffraction pattern, which indicated a highly ordered structure. It was also observed for proteins which are not directly related to neurodegenerative diseases, which indicates that the formation as well as structures of those amyloid deposits are often very similar. Based on the XRD results, the fibrils are composed elongated of β-sheets, stacked in register along the fiber axis. The interspacing of two β-strands is usually ~4.8 Å, whereas the intersheet distance is around 10 Å (Figure 2).[17, 18] However, the mechanism of these stacking and the initial event was not well understood at this point.
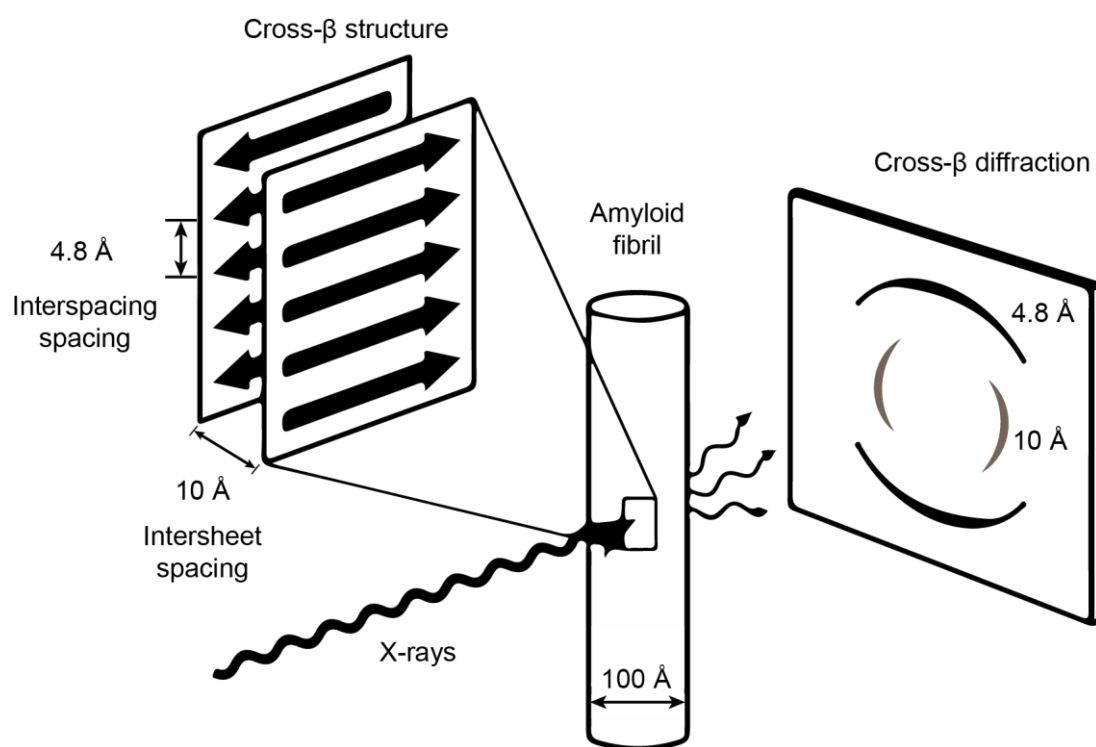
Figure 2: Schematic representation of the *cross*-β fiber pattern for well oriented fibrils. The pattern is observed, when X-rays are focused onto an amyloid fibril. Due to the diffused reflection, two values for distances are obtained. For the vertical diffraction, which reflected a repeating interspacing between β-strands, 4.8 Å were found. The horizontal diffraction of ~10 Å represent the intersheet spacing. Drawing according to the review of D. Eisenberg and M. Jucker.[17]

2.1 Amyloid Formation

All proteins are able to form amyloid fibrils under certain conditions and they all share similar assembly characteristics.[2, 19] It is supposed that the formation of an amyloid fiber from a solution of monomeric precursors requires at least two fundamental steps. The first assumed step is the nucleation of monomers in a solution, which may undergo an unfolding/misfolding. The second step is the elongation of the fibril which subsequently results in the formation of insoluble fibrils.[20] Various factors, such as inter-chain interactions, polarity, hydrogen bonding and several more can facilitate this elongation process.[21, 22] To monitor these fibril formations in real-time, kinetic experiments with dye molecules like thioflavin T (ThT) are commonly used. Usually, photo exited free ThT does not show strong fluorescence, since its high structural flexibility leads to large non-radiative relaxations. However, the binding of ThT, more precisely the intercalation into the amyloid fibrils, increases the fluorescence by restricting the structural flexibility and blocking non-radiative relaxation pathways whereas the quantum yield increased.[23] This leads to a detectable fluorescence, which increase with the amount of fibrils.[24] Typically, monitoring the ThT fluorescence suggest, that the formation of amyloid fibrils in solution follows a sigmoidal growth profile, which can be divided into three phases: a lag-, growth-, and a final saturation-phase (final plateau regime)[1, 19, 20] (Figure 3).[2] During the lag-phase, small, transient, and soluble oligomers (precursors) are supposed to be present. Those early oligomers maintain a large number of structural species with diverting sizes in uneven amounts (polydisperse). Moreover, the precursors can further exchange subunits to each other (dynamic interconversion) or undergo conformational transitions, which lead to the presence of diverse conformers (polymorph). With these dynamic interconversions, some precursors can form nuclei which are able to grow to large fibrils. Once, the nuclei are formed and an autocatalytic growth-phase is initiated up to the presence of mature amyloid fibrils (saturation-phase). Those nuclei (seed) works as a template to resemble monomers into amyloid fibrils.[2, 20] The duration of the lag-phase highly depends on environmental conditions such as temperature, pH-value, solvent conditions, mechanical impacts etc.[20] However, the formation of an amyloid seed is a relatively rare event. Hence, the duration of the lag-phase can be out of the experimental time scale. To circumvent the lag-phase, an external nucleus can be used to initiate the autocatalytic growth-phase (seeding).

On the other hand, small molecules can also disturb the formation of the nuclei, which leads in an inhibition for the fibril formation.
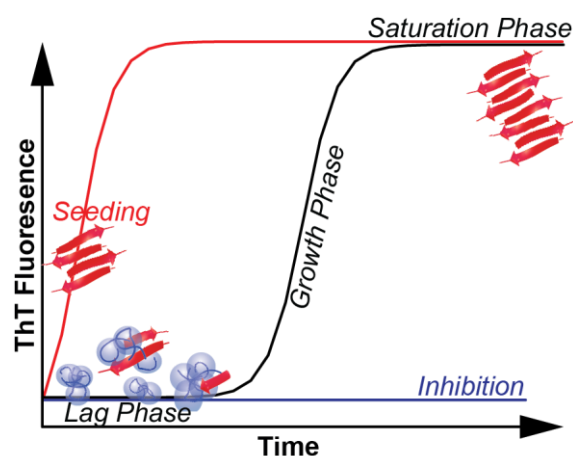
Figure 3: Features of amyloid formation. This formation can be divided into three phases: lag-, growth-, and saturated-phase (black line). During the lag-phase, no fibrils are found and only soluble intermediates are present. Under certain conditions, a so-called nucleus is formed which initiated an autocatalytic growth-phase which runs up to mature fibrils (saturation-phase). To reduce or skip the lag-phase, the growth-phase can be initialized by the addition of an external nucleus, so-called seeding (red line). In the presence of an inhibitor, no fibril formation is observed (blue line).[2]

2.2 Structural Characteristics of Amyloids

Structural characterizations of amyloid fibrils are important to get evidences of the assembly pathway and the structure of their intermediates. By understanding this pathway well, drug development could be accelerated to treat neurodegenerative diseases. In the last few decades, research provides a good understanding about the fundamental structures of amyloid fibrils. This information is mainly provided by X-ray diffraction (XRD) and nuclear magnetic resonance (NMR) experiments on fibril structures of small[5, 25] and larger proteins such as amyloid-beta protein (Abeta).[26, 27] All investigated fibrils contain a similar core structure, the steric-zipper. This core structure is build-up of a pair of β-sheets, with facing side chains which look each other (Figure 4)[28]. At first, this feature was observed for the peptide GNNQQNY from the prion Sup35 by the group of Eisenberg.[5] This peptide fibril structure is composed of parallel β-sheets, stacked in register along the growth axis (Figure 5a). Additional hydrogen

bonds are formed between asparagine (Asn – N) and glutamine (Gln - Q) residues and are responsible for the stability of the fibril.
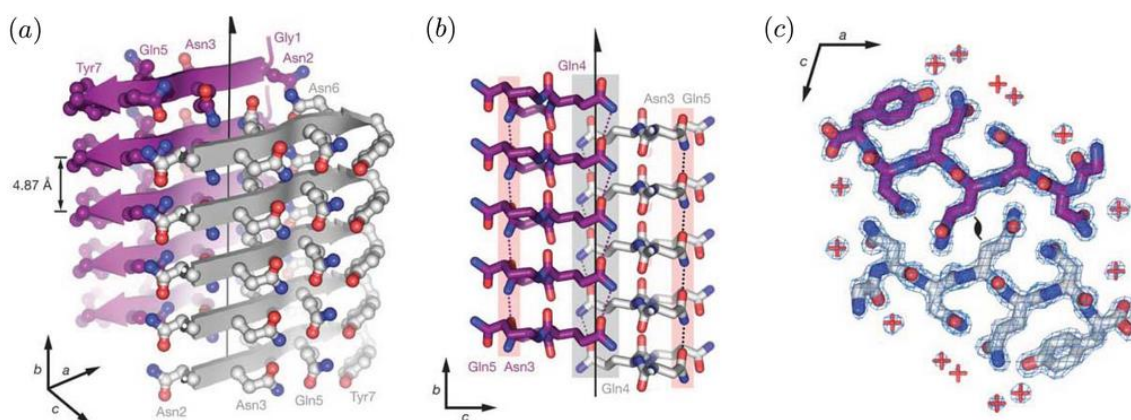
Figure 4: Representation of the fibril structure, formed by the GNNQQNY peptide derived from the prion Sup35. Carbon atoms are labelled purple/grey/white; nitrogen atoms are shown in blue and the oxygen atoms are displayed red. (a) The backbone of the GNNQQNY peptide adopts parallel β-sheets within the fibril structure. Both strands are parallel orientated to each other and perpendicular to the growth axis (black arrow in between). (b) Side view of the fibril were the hydrogen bonds are indicated between the red carbonyl groups and the blue amine group. (c) Top view of the fibril shows water molecules which are assigned by red +. As shown, the sidechains of the peptides interlock like a sterically zipper. Figure taken from Schreck ET AL. which was reprinted from Sawaya ET AL.[5, 17, 28]

Due to the electrostatic interactions of these aligned hydrogen bonds, the other amino acids polarized each other which leads to even stronger hydrogen bonds than those in ice (cooperative effect).[29] Furthermore, the sidechains of the faced peptides interlock like a steric-zipper which also increased the stability. Furthermore, hydrogen/deuterium exchange- (HDX) and XRD experiments showed, that the region between the sheets are inaccessible for water molecules, which is the reason why these form of β-sheet stacking also is referred "*dry steric-zipper*".[16, 17, 28] In addition, the resulting fibrils respectively small parts of fibrils are able to function also as a seed. Hence, when a small part of a fibril is added to a solution of early oligomers, the fibril elongation continued and the growth phase will initiate. This fact also proves the stability of the fibrils. In conclusion, the formation of a steric-zipper illuminates the stability of amyloid fibrils, their self-seeding characteristic and their tendency to form polymorphic structures.[17] *Via* XRD experiments, dozens of those dry steric-zippers have been determined which share the following same properties:[17]

(1) They form sequences in which their sidechains can interdigitate like a steric-zipper. These sequences can be polar or nonpolar with small or large sidechains, but they fit together in complementary fashion.

(2) The interface between the sheets is free of water. Thus, steric-zippers have a dry interface between two sheets.

(3) The β-strands are often in register and the hydrogen bonding is maximized.[17]

Furthermore, Eisenberg and co-workers investigated 30 fibril-forming peptide sequences taken from 14 disease-related proteins using atomic-resolution crystallographic methods.[5] For 13 peptides, they observed fibrils or needle-shaped microcrystals. With that, they distinguished eight classes of steric-zippers, whereas only five were observed at this point.[5] After many studies in the recent years, only for class 3 no examples were observed yet.[16] In general, the eight classes of different steric-zippers can be distinguished by the following:

(I) The packing of the sheets (the strands in their sheets) can be parallel or anti-parallel.

(II) The packing of sheets can be either with the same ("face-to-face") or different ("face-to-back") surfaces adjacent to one other.

(III) The orientation of sheets can be either in parallel ("up-up") or antiparallel ("up-down") fashion, with respect to one another.

According to this, the eight different classes of steric-zippers are schematically shown in Figure 5.
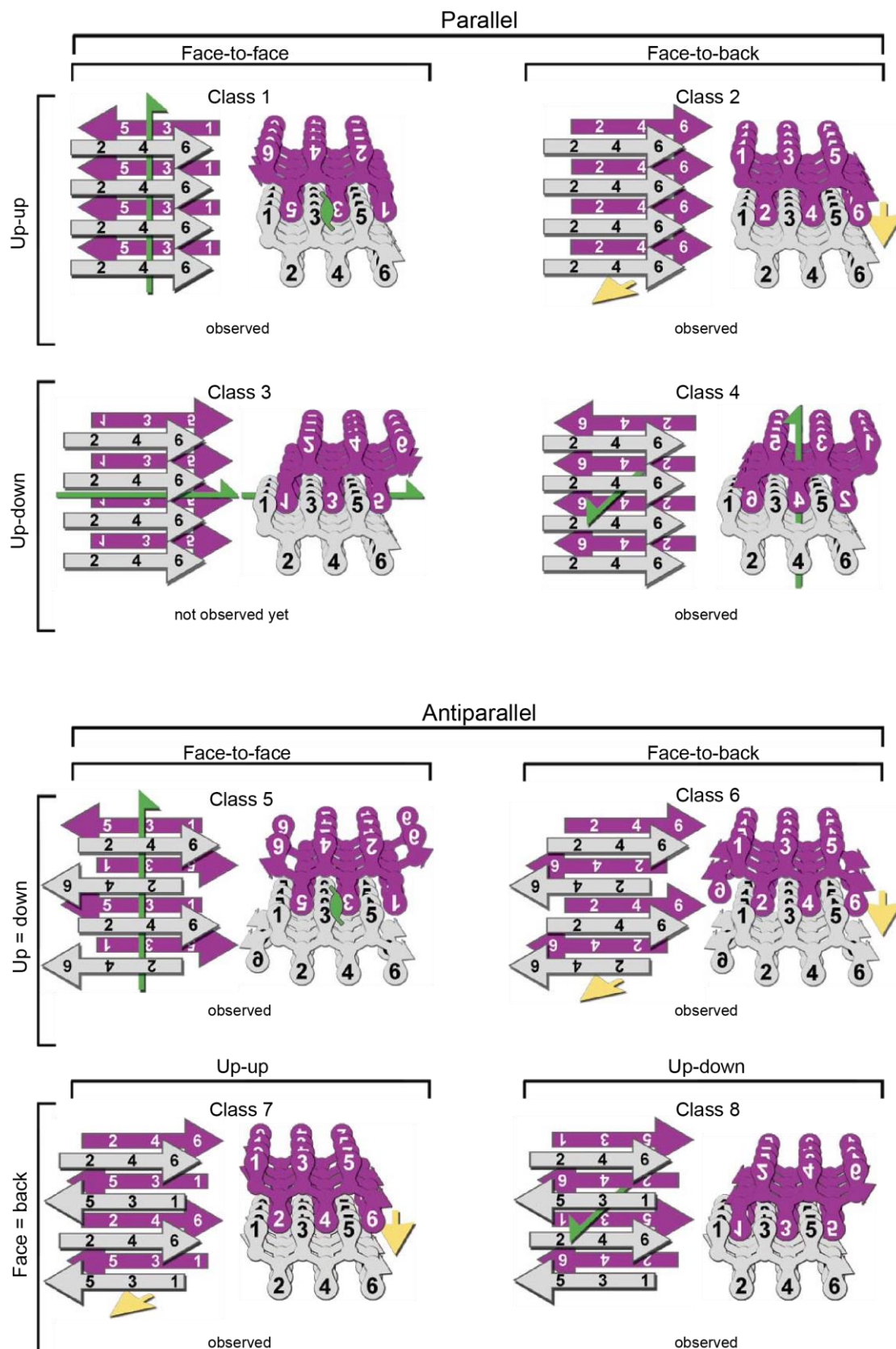
Figure 5: The eight classes of steric-zippers. The classes can be distinguished by (I) the packing of strands within the sheets (parallel or antiparallel), (II) the packing of the sheets with the same ("face-to-face") or different ("face-to-back") surface adjacent to one other and (III) the orientation of the sheets itself ("up-up" and "up-down").[5, 17, 30] Figure according to the publication of Sawaya ET AL.[5]

Furthermore, a fibril can be formed due to the stacking of these zippers in one direction (in register). The stacking, however, is not a static process which leads to a long mature fibril. Hydrogen/deuterium exchange (HDX) experiments coupled with several nuclear magnetic resonance (NMR) and mass spectrometry (MS) methods by Dobson and co-workers[31] showed, that the fibrils which are build up by in register stacked steric-zippers, undergo a permanently dissociation and re-association of monomer units at both ends of the fibril in an equilibrium. Thus, the formation of fibrils is a dynamic growth process.

However, all observed steric-zippers are formed due to the interlock of the sidechains of the same sequences. Theoretically a steric-zipper can also be formed out of different interdigitated sequences. Especially in the case of Abeta, which is a relatively long peptide, solid-state NMR studies showed some close interactions between β-strands which differ in their sequence. Due to the high stability of steric-zippers, it is assumed that those "heterogenic-zippers" play a role for the Abeta aggregation. Otherwise, this kind of zippers was only observed in NMR-studies, but not in X-ray diffraction (XRD) experiments so far.[30] Due to the fact, that a homogeneous crystal is needed for XRD measurements makes it difficult to investigate the structural features of such long peptides like Abeta. A common way to get information of structural motifs, is to investigate smaller fragments. But also here, homogeneous crystals are difficult to obtain and NMR experiments take too long and need a relative high sample concentration,[32] which could lead to aggregations and thus provides biased spectra. In general, solid state methods such as XRD require homogeneous crystals. However, oligomers do not form such crystals easily because they are transient and undergo an equilibrium. Therefore, only average information about the crystal structure is obtained and clear structural information about the fibril forming oligomers and their assembly pathway cannot be acquired. Condensed-phase methods, on the other hand, only obtain an average result of the sample. Individual information about singly conformers or species are not obtainable with those methods. Thus, it is not clear, which oligomeric states are involved in the structural transitions which are responsible for initiating the fibril formations. These facts lead to a new approach. Recently, gas-phase techniques such as ion mobility-mass spectrometry (IM-MS), which is able to separate ions based on their charge, size, shape, and mass, were coupled with infrared (IR) spectroscopy to get individually secondary structure information of early oligomeric states of peptides.[3] This method was also used in this thesis.

3. Methods

3.1 Ion Mobility-Mass Spectrometry (IM-MS)

Ion mobility spectrometry (IMS) is a gas-phase separation technique which allows to separate ions under the influence of an electric field based on differences in their size, shape and charge state. Initially, IMS was implemented (as a stand-alone technique) by US and UK defense agencies to observe human activities during the Vietnam War in the 1960s. Nowadays, it has a wide range of applications in the civil sector, e.g. for airport security, food control, air quality analysis, medical diagnostic etc.[33] In the field of chemistry and biology, IMS is routinely used for the separation and structural characterization of conformers and isomers in the gas phase.[9, 32] Especially for the individual structural characterization of transient and complex mixtures, as they occur for amyloid forming sequences, this method has the unique advantage to serve as a filter for a subsequent investigation by orthogonal technique. In this thesis, IMS is coupled with a time-of-flight mass spectrometer (TOF) as an analyzer, which is called ion mobility-mass spectrometry (IM-MS). By combining of these two methods, information on size, shape, mass, and charge of the analyte can be obtained.[32]

A typical IM-MS experiment starts with the ionization of the sample *via* electro spray ionization (ESI). The generated ions are injected into the ion mobility cell (also called drift-cell), which is filled with an inert buffer gas such as helium or nitrogen (Figure 6). Generally, the pressure of the used buffer gas is between 1 to 15 mbar or at atmospheric pressure.[9] Under the influence of an applied weak electric field, the ions traverse the drift-cell. During this migration, larger and extended ions undergo more frequently collisions with the buffer gas and therefore they need more time to traverse the drift cell. Hence, smaller and more compact ions need less time to traverse the drift-cell. This called drift time t_d of particular ions is recorded by measuring the ion current at the detector and further converted to a rotationally collision cross-section (CCS). Due to the fact, that the arrival time of each conformer of a molecule is different, a distribution of time is obtained which is called arrival time distribution (ATD).
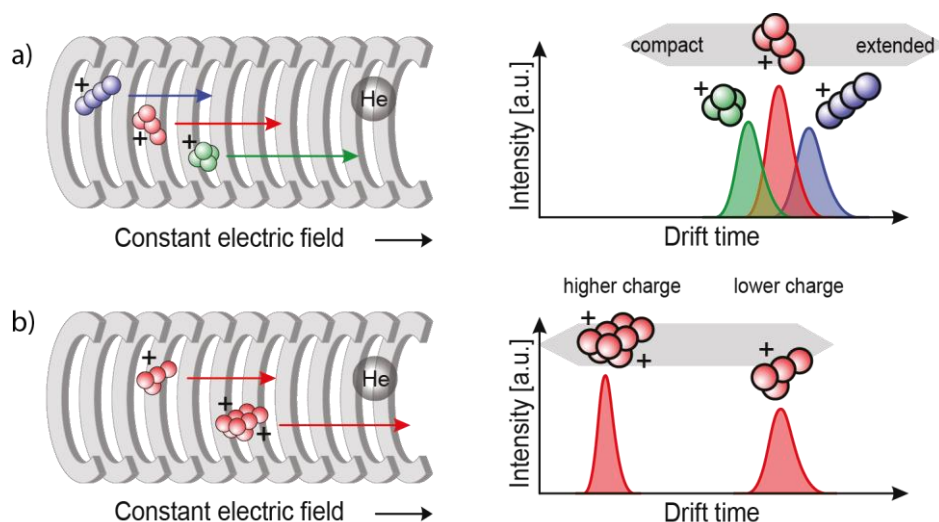
Figure 6: Principle of an IMS separation. Ions are guided by a weak electric field through a drift-cell, which is filled with an inert gas (here Helium). The arrival time distribution (ATD) depends on the size and charge of an ion (right panels). (a) Smaller molecules traverse the drift-cell faster than larger ones, when having the same charge. (b) In addition, higher charged molecules travel faster than lower charged molecules and have thus shorter drift times.

3.2 Collision Cross-Section (CCS)

The transport of ions under the influence of an electric field was first observed in the beginning of the 20th century and studied by *Paul Langevin*, which is the basis of the current view on diffusion of ions in the gas phase.[14, 15, 33] The time that the ions need to traverse the ion mobility cell (IM), the drift time t_d, depends on instrument parameters like the length of the drift region, pressure and temperature. In order to introduce an instrumentally independent value which describe the size and the shape of a molecule, the drift time t_d can be converted into a collision cross-section (CCS). Hence, CCS values provided from different instruments are comparable and databases can be realized. The CCS, typical given in $Å^2$ or nm^2, is defined as the area around a particle in which the center of another particle must be placed in order for a collision to occur.[34, 35] It is also the average of the shadow area of a particle in different positions. Figure 7 shows an old sketch of the first method to determine the CCS of an object.[36]
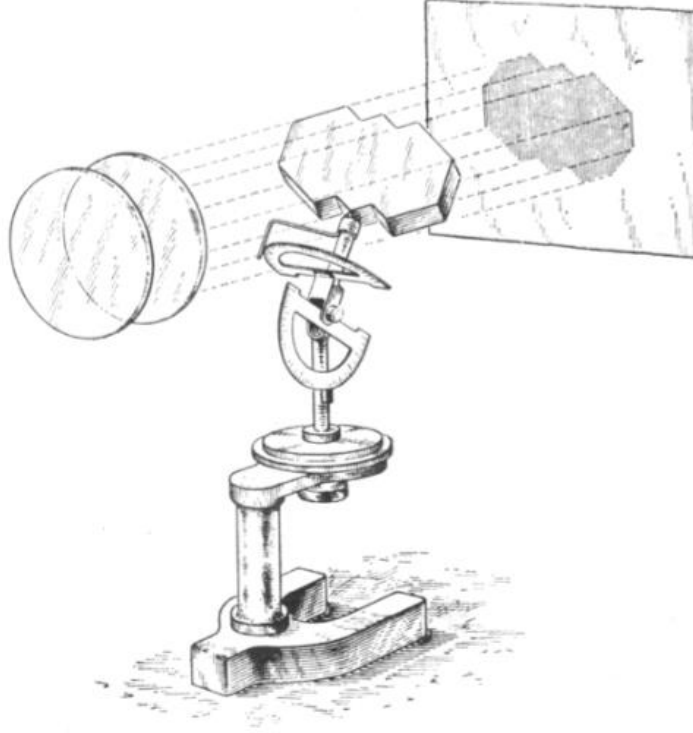
Figure 7: Simple representation to determinate the collision cross-section (CCS) of an object at the middle of the 1920s. The object correlates to anthracene.[36]

When ions travel through a gas-filled chamber (drift-cell) under the influence of a weak electric field, the drift velocity v_d of an ion is proportional to the applied electric field E and therefore the voltage V, and further the ion mobility K. Here, the ion mobility K is usually expressed in $cm^2\ V^{-1}\ s^{-1}$.

$$v_d = KE \tag{1}$$

The ion mobility K is related to the collision cross-section (CCS, Ω) and the drift-gas number density N. According to the theory of *Chapman–Enskog*[33], the *Mason-Schamp* equation is obtained:

$$K = \frac{v_d}{E} = \frac{3}{16}\sqrt{\frac{2\pi}{\mu k_B T}} \cdot \frac{ze}{N\Omega} \tag{2}$$

$$\Omega = \frac{3e}{16N}\sqrt{\frac{2\pi}{\mu k_B T}} \cdot \frac{z}{K_0} \tag{3}$$

where k_B is the Boltzmann constant, T the drift gas temperature [K], z is the number of elemental charge [dimensionless], e is the elementary charge and μ is the reduced mass ($m_i \cdot m_g / (m_i + m_g)$) of the ion-molecule system. Here in equation 3, K_0 is the reduced mobility, which takes the standard pressure ($p_0 = 760$ torr) and temperature ($T_0 = 273.15$ K) into account to make the CCS values comparable between different instruments.[33, 37, 38] According to this, a higher charge state z of the ion leads to a higher mobility K and hence to shorter drift times. Thus, IMS allows the separation of ions based on their CCS values, which can be correlated to the size, shape and charge of ion.

3.3 Determination of the Collision Cross-Section

In practice, the measurement of the drift time t_d at one particular drift voltage V_d does not allowed to calculated exact CCS values, because an additional flight time t_0 to the detector is always appended after the IM separation and t_0 cannot be determined accurately. The observed drift time t_d is given by equation 4,

$$t_d = \frac{L}{KE} + t_0 \tag{4}$$

where L is the length of the drift region and t_0 is the additional flight time. A more convenient expression for the observed drift time t_d is given by the linear equation 5.

$$t_d = \frac{L^2}{K} \frac{1}{V_d} + t_0 \tag{5}$$

Hence, t_d can be plotted as a function of $1/V_d$ for several different applied voltages V_d and this yields a linear regression, in which L^2/K represents the slope and t_0 correspond to the intercept of the fit with the ordinate (Figure 8).
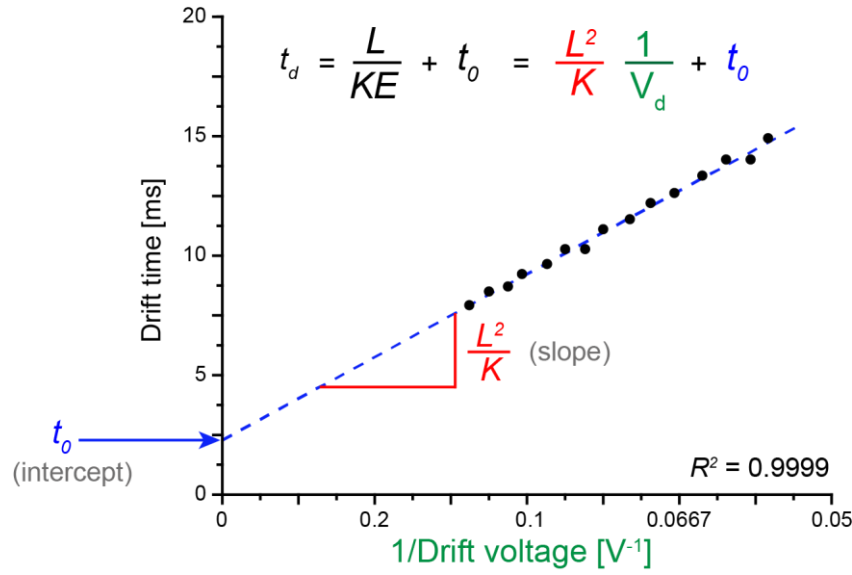
Figure 8: Schematically representation of the determination of the mobility K of an ion. The measured drift times t_d are plotted *versus* the invert drift voltages $1/V_d$. The slope is given by L^2/K and the dead time t_0 is given by the intersection of the linear regression with the ordinate.

Using this approach, the ion mobility K is determined and can be used subsequently in the *Mason-Schamp* equation to calculate the collision cross-section of the ion.[32, 33, 39]

3.4 IM-MS Approach to Investigate Oligomer Growth and Fibril Assembly

The CCS values can be used to deduce information of the self-assembly of oligomers. Amyloid forming sequences usually form unstructured aggregates (during the lag-phase), following by a nucleation dependent growth into highly linearly, structured fibrils. Unstructured aggregates usually resemble special structures and their CCS can therefore be predicted by a theoretical isotropic growth model (equation 6). This model assumes, that the density of aggregates does not change during the aggregation into bigger spheres.[40, 41]

$$\Omega_n = \Omega_1 \cdot n^{2/3} \tag{6}$$

Here, the number of monomers (oligomeric state) is given by n, Ω_1 is the measured CCS value of the monomer, and Ω_n is the estimated CCS value of the theoretical isotropic cluster of n monomers. A fibrillary assembly can be easily distinguished from the isotropic model. As

15

mentioned above, oligomers grow in one direction to form a fibril and therefore their CCS would also increase linearly with the oligomer number n as shown in equation 7.

$$\Omega_n = x \cdot n + m \tag{7}$$

The fibril shell area per monomer unit is describe by the slope x and m is related to the fibril base given by the fibril diameter.[41] Figure 9 shows the linearly dependency of the oligomeric state *versus* the CCS of a fibril formation.
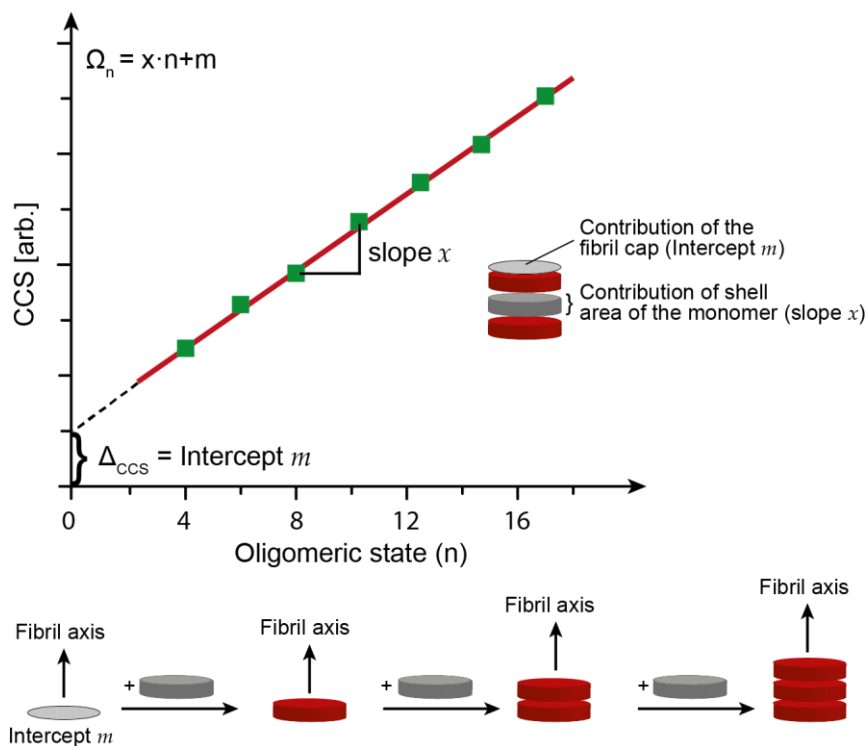
Figure 9: Theoretical CCS fibril growth model. The CCS increase linearly with the number of monomer units n in the fibril. This theoretical CCS fibrillary growth can be describe by the formula $\Omega_n = x \cdot n + m$ where the slope x is the change in the shell area which is depended by adding or removing a monomer unit along the fibrils axis (lower panel). The intercept k described the contribution of the fibril cap and can determine by extrapolation. Figure according to Bleiholder ET AL.[41]

A model peptide YGGFL, called leucine-enkaphalin, forms an isotropic crystal. If this peptide is investigated by IM-MS, the CCS values of the observed oligomers also follows the theoretical CCS values predicted by the isotropic growth model. Furthermore, oligomers of fibril forming sequences such as VEALYL, derived from the B-chain of insulin, were shown to deviate from this isotropic growth model. Those oligomers were shown to adopt more extended structures,

where the CCS values grow linearly with increasing oligomer number. Later it was also shown, that extended oligomers exhibit β-sheet content than more compact conformers.[3, 11, 41] In Figure 10, the growth trend of YGGFL and VEALYL are compared with the theoretical one (isotropic growth).[41]
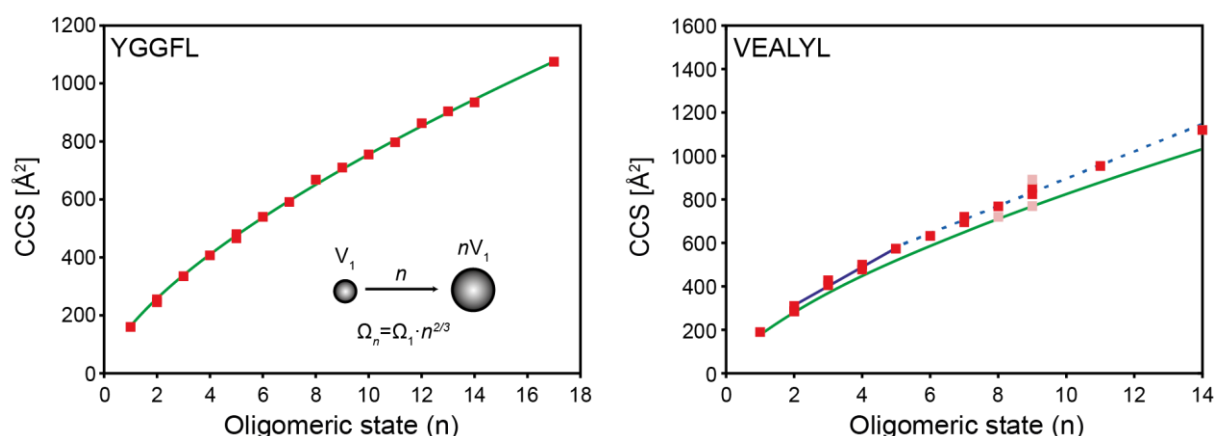
Figure 10: Measured collision cross-sections (CCSs) as a function of the oligomeric state (n) for YGGFL and VEALYL. On the left panel, YGGFL growth isotropically with $n^{2/3}$ (green line). The VEALYL peptide on the right panel, however, growths linearly, which suggests an assembly like in a single fibril (from dimer to the pentamer; solid line) Furthermore, the data indicate a second linear growth behavior, which suggests a growth into a doublestrand, as it occurs for "steric-zippers" (dashed line). Figure according to Bleiholder ET AL. 2007.[41]

Ion mobility-mass spectrometry (IM-MS) is sensitive towards the overall shape of an ion. Theoretical models for the CCS growth can further help to deduce secondary structure information. However, extended structures observed in an IM-MS experiment could also be formed in the gas phase due to *Coulomb* repulsion and therefore IM-MS on its own is only guessing for the secondary structures. To address this problem, IM-MS can be used as a preselection tool for orthogonal techniques, which are more sensitive to the fine structure. In particular, infrared (IR) spectroscopy can be used to probe intermolecular vibrations, such as C=O stretching mode (amide I band; $\tilde{v}$ = 1620 – 1640 cm^{-1}),[3, 10] which is highly depend on the secondary structure, adopted by peptides and proteins. The combination of IM-MS and gas-phase IR spectroscopy allows to obtain IR spectra of *m/z* and drift time selected oligomers.

3.5 The Drift Tube-Ion Mobility-Mass Spectrometer (DT-IM-MS)

To achieve structural information, the used drift cell is coupled with a time-of-flight mass spectrometer (TOF) and a second off-axis electron multiplier detector to acquire the mass spectra and the arrival time distribution (ATD) simultaneously of the separated oligomers.[42] Figure 11 shows the instrumental setup which was used in this thesis.[10, 43]

Ions are generated in a nano-electrospray ionization source (nESI) and transferred into the gas phase. Due to a potential between the nESI source and the entrance-capillary, the ions are guided into the instrument. The injected ions are collected (over tens of milliseconds) by a radio-frequency (RF) funnel (entrance funnel) and further pulsed into the drift cell (drift-tube, length: 80.55 cm). Under the influence of a weak linear electric field (10-20 V/cm), the ions traverse the buffer gas filled drift cell (helium, p ~ 4 mbar) and are separated based on their size, shape, charge, and mass. After this, a second RF funnel (exit funnel) focuses the diffused ion clouds and provides radial confinement as well as ensures the transport of the ions through a series of ring electrodes (ion guides) to the high vacuum region of the instrument.
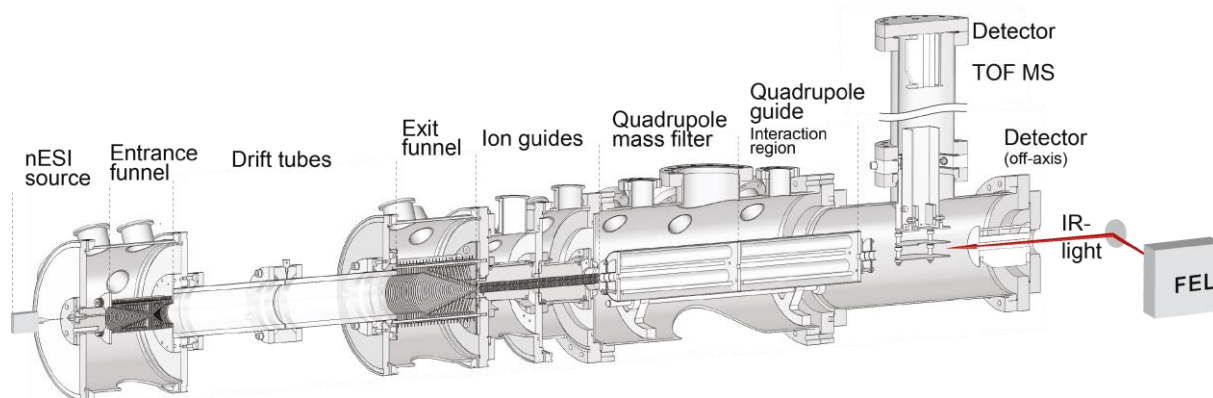
Figure 11: Schematic representation of the setup of the home-built drift-tube ion-mobility-mass spectrometer (DT-IM-MS). In the interaction region, the ions are irradiated and fragmented by the photons, which are provided by the free electron laser (FEL).[43]

Subsequently, two quadrupoles follow, where the first one selects the ion clouds on their mass to charge ratio (m/z), the second one is used as an ion trap. Steering lenses allows to manipulate the flight as well as the horizontal and vertical direction of the ions to improve the trajectory to the detectors (ATD and TOF-detector). Finally, to provide light into the instrument for the infrared multi photon dissociation spectroscopy (IRMPD), a KRS-5 (thallium bromide-iodide) window with an optical transparency of ~70 % is mounted at the end of the instrument. To perform m/z and conformer selected IRMPD spectroscopy, a narrow drift time window is used for the ions by electrostatic deflection at the end of the exit funnel.[43] The preselected conformers were irradiated by high intense IR radiation provided by a tunable, high coherent free electron laser (FEL). Due to the high intense IR radiation of the FEL, multiple photon absorption induces a subsequent fragmentation, which is detected by the time-of-flight mass analyzer (TOF). The IRMPD spectra are provided by displaying the fragmentation yield as a function of the wavelength.[10, 43]

3.6 Infrared Multiple Photon Dissociation Gas-Phase Spectroscopy

Infrared (IR) spectroscopy is a powerful method that is widely used for structure determination of unknown substances. With this method, the vibrational modes of molecules are investigated and structural information such as on the bond lengths and on the hydrogen bonding pattern of molecules can be obtained. The fact that molecules and ions are non-rigid leads to several possibilities of movements (*bending and stretching*) and thus to an integer number of vibrational degrees of freedom. Every molecule with N atoms in a three-dimensional space (x, y, and z direction) had 3N degrees of freedom. This is necessary because three coordinates are needed for each atom to determine their position in the space. These degrees of freedom can be distinguished in translation, rotation and vibration terms. Depending on the numbers of atoms N in a molecule, 3N-5 and 3N-6 vibrational modes of freedom are obtained for linear and for non-linear molecules, respectively. If a vibrational mode of a molecule is in resonance with the IR radiation, an absorption of photons occurs which leads to vibrational excitation. Usually, the radiation frequency is described in wavenumbers ($\tilde{v}$) and is given as reciprocal centimeters (cm^{-1}). In first proximity, a molecule bond can be expressed as a helical spring, which obeys Hooke´s law (equation 8)

$$F = -Dx \tag{8}$$

where F is the force, D a real number, which is characteristic for the spring (bond) and x describes the displacement. In quantum mechanics, this spring model leads to the important model of the harmonic oscillator, in which vibrational states are equal with defined energy levels:

$$E_v = \hbar\omega \left(v + \frac{1}{2} \right) \tag{9}$$

with ω as the frequency of the oscillator and the integer of vibrational quantum number v. However, this theory fails for higher energy levels, especially for dissociation processes, as the vibrational modes of a molecule do not behave like a harmonic oscillator with well-defined energy levels. A more elaborated model to describe the disharmonic nature of molecular bonds is the *Morse* potential. Here, the energy levels are not equally spaced and the dissociation

energy can be determined. A schematic comparison between both potentials is shown in Figure 12.
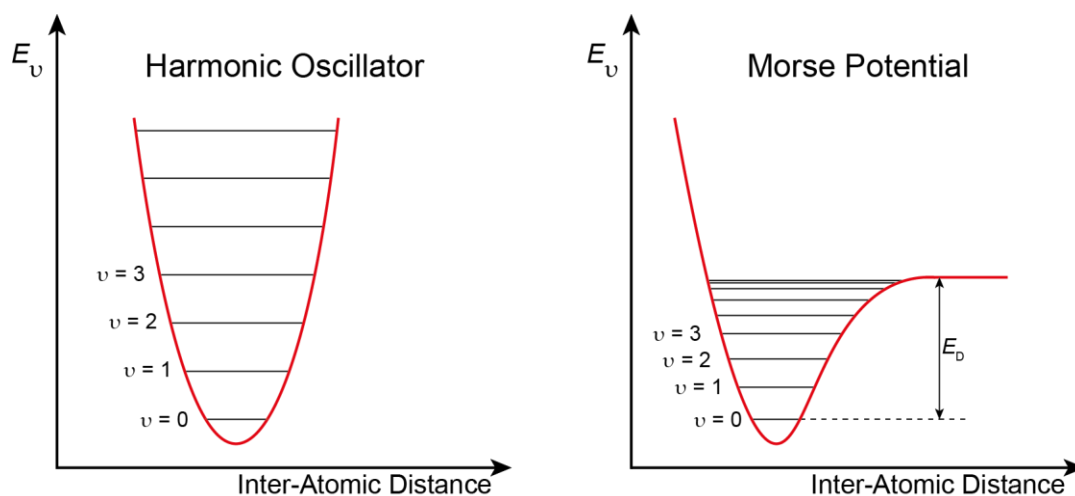
Figure 12: Sketch of the harmonic oscillator (left) and the *Morse* potential (right). Energy levels are equally spaced (equidistant) in the harmonic oscillator, whereas in the case of the *Morse* potential the distance of energy levels decreases with increasing energy. The dissociation energy E_D can be determined using the *Morse* potential.

A typical experimental setup to investigate vibrational modes of molecules is the measurement of the attenuation of light which is caused by the absorption resonance of photons. In this so-called *absorption spectroscopy*, the wavelength dependent absorption, which is usually given as Extinction E_λ, can be expressed by the concentration c, the dimension d of the sample and the specific absorption coefficient ε_λ. This coherence was first observed 1852 by *August Beer* and leads to the *Lambert-Beer´s law*, which is given in equation 10.

$$E_\lambda = -ln\left(\frac{I_1}{I_0}\right) = \varepsilon_\lambda \cdot c \cdot d \tag{10}$$

The attenuation of the light is described by the term (I_1/I_0), where I_0 is the intensity of the light before and I_1 the intensity after passing the sample. Since the classic vibrational spectroscopy approach measures the change in photon density, a relatively high amount of analyte molecules is necessary to detect differences between the incoming light before and after passing the sample. In the gas phase, however, the molecule concentration is limited due to a space-charge limit of approximately 10^6 ions per cm³, and therefore the changes in light is hardly observable.[44] Hence, instead of classical absorption spectroscopy, a so-called action

spectroscopy is used. Action spectroscopy monitors the influence of the light on the molecules, i.e. a light induced dissociation. One of these methods is the infrared multiple photon dissociation spectroscopy (IRMPD) which can be used also in the gas phase. IRMPD is an activation technique to induce vibrations into a probed molecule by irradiation with IR light. This multistep mechanism is based on fast intermolecular vibrational energy redistribution (IVR), whose timescale is usually shorter than several nanoseconds.[44-46] A schematic energy diagram of the IRMPD mechanism is shown in Figure 13. Here, a polyatomic molecule absorbs a single photon (in the range of hundreds of meV), which is resonant with the frequency of a vibrational mode. The absorbed energy of this induced vibration is immediately distributed over different disharmonic vibrational modes in the background *via* IVR, which acquire more and more energy.[45] This enables the molecule to reabsorb energy from the IR radiation. This iterative process leads to an energy surge above the dissociation energy E_D and hence to the fragmentation of the molecule. Displaying the obtained fragmentation yield as a function of the wavelength provided at last the IR spectra of the irradiated molecule.[10]
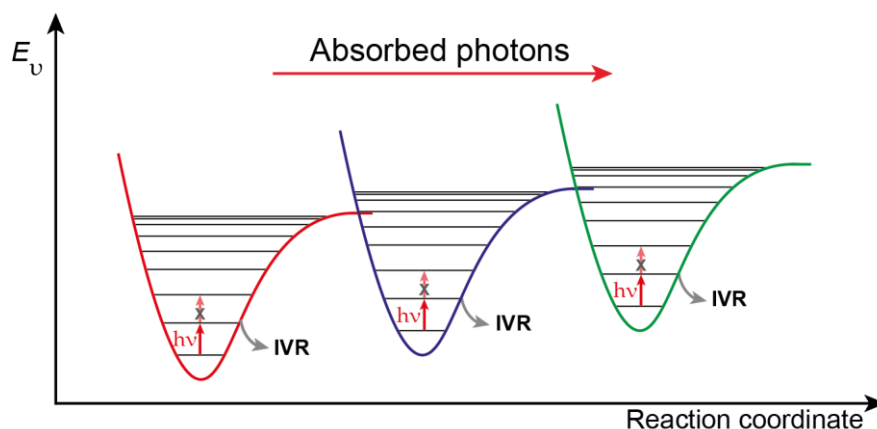
Figure 13: Schematic energy diagram of the IRMPD mechanism. The principle of the mechanism is on the fast distribution of vibrational energy after the photon absorption *via* intermolecular vibrational energy redistribution (IVR). The IVR effect leads to an increasing internal energy, which induces the fragmentation of the radiated molecule.[10]

For those multiple photon absorption and dissociation techniques, a high intensity photon source is needed. A tunable free electron laser (FEL) provides enough intensity of coherent mid-IR radiation, which can induced IR multiple photon dissociation (IRMPD).[44]

3.7 The Free Electron Laser (FEL)

In the 1970s, the group of Madey and coworkers at the Stanford University (U.S.A.) designed a novel laser source, which provides a high photon flux over a board spectroscopic range: the free electron laser (FEL).[47] Further improvements of these new technique leaded to a reliable high intensity photon source. In 2013, the Fritz Haber Institute (FHI) Berlin took also into operation such a photon source[48] which was used for the experiments in this thesis. The FEL provides intense and tunable photon pulses (~ 100 mJ/puls) throughout the infrared region (3 to 50 μm).
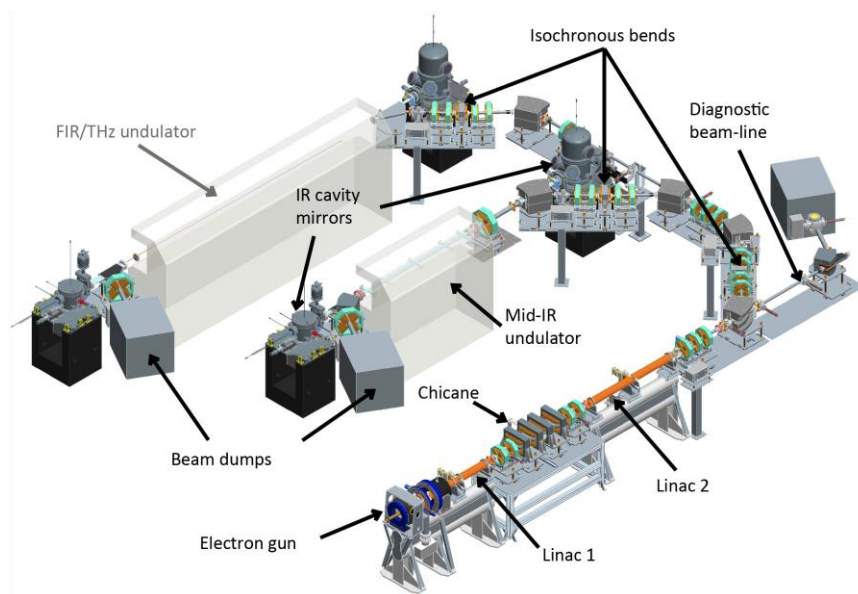
Figure 14: Schematic depiction of the FHI-FEL. The greyed, far-IR undulator is planned but not installed yet.[48]

Figure 14 depicts the general setup of the FHI-FEL[10, 48] where electrons are provided by an electron gun and are accelerated close to the speed of light (15-50 MeV) due to two linear accelerators (Linac I and Linac II). Subsequently, the electrons are injected into the resonator consisting of two high-reflectivity mirrors at each end of the undulator, where strong alternating magnets lead to a periodic deflection of the electron beam into a "wiggling" motion. Due to this deflection, the coherent monochromatic high intense radiation is provided. The gap of the undulator is tunable, which allows to achieve different wavelengths of the emitted radiation.[48, 49]

3.8 Infrared Spectroscopy of Peptides

Recently, it was shown that the structure of peptides and proteins can be investigated *via* IR spectroscopy, especially in the gas phase.[3, 10, 11] In this regard, the amide I and the amide II mode are two typically observed modes for these biomolecules shown in Figure 15.
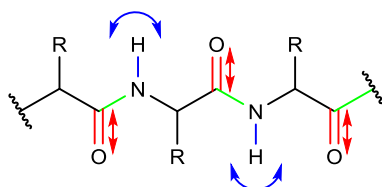
Figure 15: Scheme of a peptide backbone with the typically occurring bending and stretching modes. The amide I mode is given in red with the characteristic stretching mode of the C=O bond, the amide II mode is given in blue with the bending mode of N-H. The green bonds indicate the peptide bond of the peptide backbone.

The amide I mode corresponds to the C=O stretching mode of the peptides with wavenumbers between 1620 – 1680 cm^{-1}, whereas the amide II mode describes the N-H bending and is detected around 1500 - 1550 cm^{-1}.[48, 50] Higher intensities at particular wavenumbers allow the assignment of structural motifs. In this regard, it was reported that the amide I band occurs at 1620-1640 cm^{-1} for a β-sheet rich structure of peptide oligomers.[3, 51] On the other hand, wavenumbers at around 1650-1660 cm^{-1} are expected for an unordered structure such as α-helices, turn or random coil.[3, 51-53] The environment of the peptides influences the bond strength D and hence the vibrational frequency (equation 11). As expected, the frequency increases with D (the stiffness of the bond) and decreases with μ (the reduced mass: $(m_1 \cdot m_2/(m_1 + m_2))$.

$$v = \frac{1}{2\pi}\left(\sqrt{\frac{D}{\mu}}\right) \tag{11}$$

For the vibrational modes of peptides, hydrogen bonds play a major role for the amide I band ($\tilde{v}$ = 1620 – 1680 cm^{-1}) as well as for the amid II band ($\tilde{v}$ = 1500 – 1550 cm^{-1}).[3, 17] As a result, especially in larger oligomers with an increases hydrogen bond network, the amide I band is shifted to lower (red shift), the amide II band to higher (blue shift) wavenumbers. Therefore, it is possible to receive structural information of the three-dimensional folding of peptides using of IR spectroscopy, especially in the gas phase.

4. Aim

Non-covalent associated peptide oligomers of amyloid-beta (Abeta) 42 have recently been identified as the major toxic species in Alzheimer´s disease (AD). Interestingly, the shorter peptide version Abeta 40, inhibits the aggregation of Abeta 42 and is therefore believed to be cytoprotective. This indicates that the last two amino acids (isoleucine and alanine) of Abeta 42 have a huge influence on the aggregation behavior. In addition, the central hydrophobic core of Abeta is a major driving factor for amyloid peptides.

In this thesis, small Abeta fragments, derived from the central hydrophobic core and the C-terminal end, as well as full-length Abeta monomers were investigated. A combination of condensed-phase methods such as FT-IR spectroscopy and gas-phase methods such as IM-MS coupled with IR spectroscopy were applied. Those methods are highly sensitive towards the secondary and tertiary structure adopted by peptides and proteins. The aims of this thesis are to understand the aggregation characteristics of the central hydrophobic core, the influence of the last two amino acids on the assembly pathway of the Abeta peptides and the structural characterization of Abeta monomers.

5. Experimental Section

5.1 Solvents, Chemicals, Reagents and Samples

Methanol (MeOH) was purchased from Merck KGaA (Darmstadt, Germany). The used water (H₂O - HPLC grade) was purchased from VWR (Radnor, Pennsylvania, U.S.A.). All other solvents, chemicals, and reagents were purchased from Sigma-Aldrich (Taufkirchen, Germany). The peptide with the sequence $_{16}$KLVFFAE$_{22}$ was synthesized *via* solid phase peptide synthesis (SPPS) and purified by Waldemar Hoffmann (M. Sc.), as were also the two peptides $_{37}$GGVVIA$_{42}$ and $_{35}$MVGGVV$_{40}$. For a further purification of these peptides, a preparative and analytical computer-controlled high pressure liquid chromatography (HPLC) was used (see chapter 5.2 Peptide Purification).

The peptides $_{36}$VGGVVI$_{41}$ and $_{35}$MVGGVVIA$_{42}$ were obtained from CENTIC BIOTEC (Heidelberg, Germany). The Abeta 40 and Abeta 42 samples were purchased from Genscript Biotech Corporation (People´s Republic of China). All commercial ordered substances and solvents were used without further purification.

5.2 Peptide Purification

The $_{16}$KLVFFAE$_{22}$ peptide was synthesized and purified by W. Hoffmann (M. Sc.). $_{37}$GGVVIA$_{42}$ and $_{35}$MVGGVV$_{40}$, were also synthesized by him and the purification and analysis is described in the following.

Before the purification with a preparative-reversed phase HPLC, the peptides were dried by lyophilization. After dissolving the peptides in water/acetonitrile (H₂O/ACN, 1:1, v/v) the purification was performed by using a LaPrep low-pressure HPLC system (VWR, Darmstadt, Germany). To dissolve the peptide $_{37}$GGVVIA$_{42}$ completely, 2.5 Vol% DMSO was added to the solution. A Kinetex RP-C18 endcapped (5 µM, 100 Å, 250 x 21.2 mm, Phenomenex®, USA) was used as HPLC column and a Security Guard™ PREP Cartridge Holder Kit (21.20 mm, ID, Phenomenex®, USA) served as pre-column. Deionized water (Milli-Q Advantage® A10 Ultrapure Water Purification System, Millipore®, Billerica, MA, USA) and ACN were used as eluents, both containing 0.1 % (v/v) trifluoroacetic acid (TFA). The preparative HPLC runs to

purified the crude peptides were performed with an isocratic gradient over 5 minutes, 5 % ACN with a flow rate of 10.0 mL/min, then over 25 minutes, 5-70 % ACN with a flow rate of 20.0 mL/min. UV-detection was performed at 220 nm to determine pure peptide fractions with an online data analysis (EZChrom Elite-Software, Version 3.3.2 SP2, Agilent Technologies, Santa Clara, CA, USA). The collected fractions were evaporated and lyophilized to obtain the peptides as a colorless powder.

Analytical HPLC was carried out on a Chromaster 600 bar DAD-System with CSM software (VWR/Hitachi, Darmstadt, Germany). The system works with a low-pressure gradient containing a HPLC-pump (5160) with a 6-channel solvent degaser, an organizer, an autosampler (5260) with a 100 µL sample loop, a column oven (5310), and a diode array flow detector (DAD) (5430). A Kinetex C_{18} column (5 µm, 250 Å ~ 4.6 mm, Phenomenex®, Torrance, CA, USA) was used. Water and ACN, both containing 0.1 % (v/v) TFA, were used as eluents. A flow rate of 1 mL/min was used and the column was heated up to 24°C. The UV-detection of the peptides occurred at 220 nm. A linear gradient of 5–70 % ACN + 0.1 % TFA in 18 min was applied. The data were analyzed with EZ Chrom ELITE software (version 3.3.2, Agilent Technologies, Santa Clara, CA, USA) (see Appendix, Figure 45 and Figure 46).

Mass-to-charge ratios (*m/z*) were determined with an Agilent 6220 ESI-TOF MS instrument (Agilent Technologies, Santa Clara, CA, USA). The peptides were dissolved in MeOH/ACN (1:1, v/v) and the peptide solution was injected with a *Hamilton* 1 mL syringe. Spray voltage was set to 4000 V, drying gas flow rate was 5 L/min and gas temperature was set to 300°C to evaluate the purification of $_{37}$GGVVIA$_{42}$ and $_{35}$MVGGVV$_{40}$ (see Appendix, Figure 47 and Figure 48).

5.3 Fourier Transform Infrared Spectroscopy in Solution (FT-IR)

To determine the β-sheet content of the peptides in the condensed phase, the FT-IR instrument BRUKER IFS66v (Ettlingen, Germany) spectrometer with a Globar™ (SiC) as infrared source was used. The samples were dissolved in deuterated water and methanol (D_2O/MeOD, 1:1, v/v) to the final concentration of 5 mM and injected into an IR transparent sample holder (CaF_2 windows) with a sample layer thickness of $d = 0.025$ mm. To avoid water absorption, the optics was evacuated and the sample chamber was flushed with a continuous nitrogen flow. Each

spectrum was averaged by 32 scans and recorded from 800 - 2500 cm^{-1}. To show a trend over the time of the β-sheet formation of the probed peptides, the measurements were repeated after several hours, days, and weeks. All spectra were baseline-corrected and are shown in a range of 1580 – 1720 cm^{-1}.

5.4 Drift-tube Ion Mobility-Mass Spectrometry and Gas-Phase Infrared Multiple Photon Spectroscopy (DT-IM-IRMPD)

The measured peptides were dissolved in water and methanol (H$_2$O/MeOH, 1:1, v/v) to a final concentration of 5 mM and the entire amyloid-beta sequences (Abeta 40 and Abeta 42) were dissolved in an aqueous 10 mM ammonium acetate solution (pH = 7) to a final concentration of 50 µM. Roughly 8 µL of the sample were loaded into an in-house-prepared Pt/Pd-coated borosilicate needle and voltages of 0.6 - 1.2 kV were applied on the *n*ESI source to inject the ions into a home-built drift tube device (described above).[10, 42, 43] Helium (~4 mbar) was filled in the drift-tube as a buffer gas for the ion mobility separation. The device is coupled with a nitrogen flushed beam line to provide IR radiation from the FHI-FEL.[43] IRMPD spectra were recorded from 1400 to 1800 cm^{-1}. The power was in a range between 10-50 mJ/pulse with a pulse length of 10 µs and an operating frequency of 10 Hz. All shown spectra are averaged at least of two measurements and were wavelength and power corrected.

5.5 Deconvolution of the IRMPD-Spectra

Infrared spectroscopy is an established tool for the characterization of the protein secondary structure in the condensed phase.[53, 54] The protein backbone exhibits two strong vibrational modes, namely the amide I and amide II band. The amide I absorption predominantly originates from the C=O stretching mode, whereas the amide II absorption is arising from a combination of N-H bending and C-N stretching mode. Since the amide I band is a rather "pure" mode, it is more sensitive towards the secondary structure of proteins and peptides.[2] Typical amide I frequencies are given in Table 1.

Table 1: Correlations between common protein structures and amide I frequency.[2, 51, 53, 54]

Secondary structure	Amide I band (cm^{-1})
Aggressed strands	1610–1628
β-sheet	1610–1640
Random coil	1640–1648
α-Helix	1648–1660
3_{10}-Helix, type II β-turn	1660–1685
Antiparallel β-sheet and aggregated strands	1675–1695

Both the amide I and II regions are, however, broad bands and it is not possible to resolve individual bands corresponding to different secondary structure elements. Therefore, a deconvolution procedure of the respective bands is commonly applied in the condensed phase to extract the secondary structure content of each motif.[55] Recently, a similar approach was also performed for the deconvolution of the amide I band of gas-phase IR spectra of peptides.[3] IR features in the 1600 – 1700 cm^{-1} region were fit with multiple *Gaussian* functions as shown in equation 12.

$$I = \sum_n \frac{A(n)}{\sigma(n) \cdot \sqrt{\pi/2}} \cdot exp\left[-\frac{2\{x - x_C(n)\}^2}{\sigma(n)^2}\right] \tag{12}$$

However, the IR absorption process is more complicated in the gas phase (IRMPD process) and a linear correlation of the IR intensities does not exist. Thus, the actual secondary structure content cannot be obtained and instead the fraction of β-sheet IR signature (*F(β)*) in the amide I region is calculated according to equation 13, where $A_{(n)}$ denotes the area of n-th *Gaussian*.

$$F(\beta) = \frac{A(1) + A(2) + A(6)}{\sum_{n=1}^{6} A(n)} \tag{13}$$

The amide I region was fitted with six *Gaussian* (1-6) using constraints in the peak center (x_c) and width (σ) as shown in Table 2. The constraints were set, based on the known IR band positions for the individual secondary structure elements as shown in Table 1. One additional

Gaussian at 1560 – 1600 cm^{-1} (0) is used to correct the baseline below 1600 cm^{-1}. R-square values (R^2) in the shown spectra are larger than 0.92 and gives the goodness of the fits.

Table 2: Constraints in the peak center x_c and width σ for the fitting amide I with multiple *Gaussians* according to Seo ET AL.[3]

n	Peak center	Peak width (σ)
0	1560–1600 cm^{-1}	0–30 cm^{-1}
1	1600–1630 cm^{-1}	0–30 cm^{-1}
2	1620–1640 cm^{-1}	0–30 cm^{-1}
3	1640–1660 cm^{-1}	0–30 cm^{-1}
4	1650–1680 cm^{-1}	0–30 cm^{-1}
5	1660–1690 cm^{-1}	0–30 cm^{-1}
6	1680–1710 cm^{-1}	0–30 cm^{-1}

For antiparallel β-sheet structure forming peptides, the last *Gaussian* A$_{(6)}$ is essential to determine the content for this structural motif, whereas for parallel β-sheet structures only *Gaussian* $A(1)$ and $A(2)$ is needed. This is because $A(6)$ describes the native band position for antiparallel β-sheet (Table 1).[3]

5.6 Data Analysis

The obtained raw data (measured drift times, FT-IR and IRMPD spectra) were analyzed with the software OriginPro 2015 (OriginLab Corporation, Nothhambton, MA, U.S.A.). To depict the data, Adobe Illustrator CC 2015 (Adobe Systems GmbH, Munich, Germany) was used. The collision cross-sections (CCSs) were calculated with Excel (*Microsoft*, Redmond, U.S.A.)

6. Results and Discussions

The amyloid formation is a hallmark of various diseases such as type II Diabetes or Parkinson´s and Alzheimer´s diseases (AD). The involved peptides and proteins undergo a conformational transition and assemble from soluble oligomers into insoluble deposits, often referred to amyloid fibrils (plaques). These plaques can be found for example in the cerebral cortex of Alzheimer patients and they mainly consist of the amyloid-beta (Abeta) peptide (sequence shown in Figure 16). In particular, AD is the second most important, widespread disease in industrialized countries in the Western world.[4] In 2015, 46.8 million people were known to suffer from this neurodegenerative disorder. In addition, it is predicted that in 2030 roughly 74.7 million will be affected.[56] Although many people suffer from this disease, a universal treatment is not available yet. Drug development is challenging due to an insufficient understanding of the structure, amyloid assemblies and the pathological mechanism.

$$^+H_3N-DAEFRHDSGY^{10}EVHHQ\underline{KLVFF}^{20}\underline{AE}DVGSNKGA^{30}IIGL\underline{MVGGVV}^{40}\underline{IA}-COO^-$$

Figure 16: Sequence of the Abeta 42 peptide in one letter code. The central hydrophobic core (blue section) and the C-terminus (green section) were shown to be directly involved in the aggregation cascade of Abeta 42. Based on the green underlined section, the peptides $_{37}GGVVIA_{42}$, $_{35}MVGGVV_{40}$, $_{36}VGGVVI_{41}$, and $_{35}MVGGVVIA_{42}$ were investigated in this thesis.

The amyloid cascade hypothesis (ACH) assumes that Abeta accumulation and further fibril formations are the main event in AD pathogenesis. Here, the amyloid precursor protein (APP), which normally provides soluble Abeta 40 and Abeta 42 in a non-critical and non-toxic amount by proteolytic cleavage, undergoes a *missense* mutation. This uncommon behavior leads to an imbalance and an increase of Abeta production. Especially higher concentrations of the Abeta 42 variant trigger the aggregation into insoluble amyloid plaques. In addition, environmental changes can also initiate the aggregation cascade. Those plaques lead to cognitive impairments, respectively the loss of memory (dementia) due to neuronal/neurotic dysfunctions and cell death with transmitter deficits.[57] Consequently, many studies focus on removing or inhibiting the formation of Abeta plaques. Those studies have, however, shown that a plaque removal does not improve memory loss. Furthermore, they revealed that no correlation exists between the amount of plaques inside the brain tissue and the loss of

memory. These facts weaken the ACH. Thus, alternative approaches are required to get a boarder perspective of this hypothesis. Recent investigations indicate, that not mature fibrils but rather early soluble intermediates represent the toxic species.[51] Indeed, a study using transgenic mice and rats shows that extracellular accumulation of a soluble Abeta 42 assembly with the mass of 56 kDa impairs long-term memory by an unknown mechanism.[4, 58] Further IM-MS experiments provide a suitable candidate for this assembly, which is similar to the dodecamer of Abeta 42.[4, 59, 60] The observation, that not the mature fibrils but rather soluble intermediates of the Abeta 42 fibrils are likely to be the toxic species, leads to the modified amyloid cascade hypothesis (MACH).

The monomeric state of the amyloid-beta peptides (Abeta 40 and Abeta 42) exhibit an unordered structure in solution.[51] The N-terminus of the peptides can, however, bind metal ions such as Cu^{2+} and Zn^{2+} and thereby a partial helical content is induced.[61-63] Those metal ions can further produce reactive oxygen species (ROS), which can lead to cell death due to oxidative stress.[63] If Abeta 42 interacts especially with membranes of neural cells, the impairment of fundamental cellular processes and thus the loss of long-term memory be the result. Though, before the long-term memory is affected, a decline of the short-term memory is an indication for AD. Recently, it was reported[59, 64], that early low-n oligomers of Abeta 42 have also an influence of the short-term memory by rats. These results are in line with the clinical course of the AD, where at first a decline of the short-term memory (early state oligomers) and then the impairment of the long-term memory (larger oligomers) is observed. Although the amyloid-beta 40 and amyloid-beta 42 peptides just differ in two amino acids, they exhibit vastly different properties. The amyloid-beta 42 peptide aggregates faster and is more neurotoxic than the Abeta 40 variant.[65, 66] Furthermore, Abeta 40 is able to inhibit protofibril and fibril formation of Abeta 42 and is therefore believed to be cytoprotective.[65] Few information which explains these differences, are available. Due to the complexity of the full-length Abeta peptides, many studies focus on aggregation prone sequences (fragments). However, also the intermediates of smaller fragments of the peptides are challenging to characterize. Condensed-phase methods only provide ensemble average information. Gas-phase techniques, however, can isolate and characterize one species in the presence of many others.

34

Hydrogen/deuterium exchange (HDX) experiments, which depend on the solvent accessibility, in combination with mass spectrometry have shown, that the central hydrophobic core of Abeta, $_{16}$KLVFFAE$_{22}$, does not undergo an H/D exchange. Consequently, this region is highly structured and directly involved in the assembly process of Abeta. In addition, isolated $_{16}$KLVFFAE$_{22}$ also forms amyloid fibrils *in vitro*.[67, 68]

6.1 Hydrophobic Core Fragment of Abeta
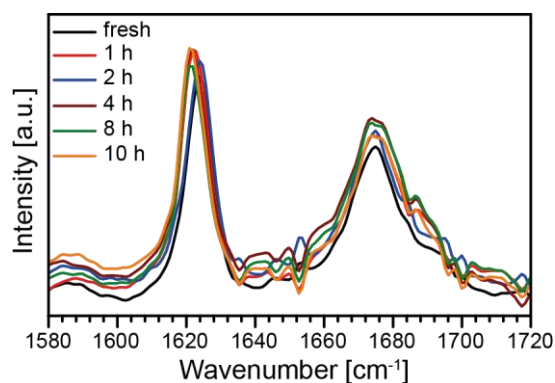
6.1.1 $_{16}$KLVFFAE$_{22}$

$_{16}$KLVFFAE$_{22}$ is reported to form amyloid fibrils *in vitro* out of a 3 mM aqueous solution at room temperature. These fibrils have a diameter in the range of 2.4 to 4.4 nm.[67, 68] Within this thesis, $_{16}$KLVFFAE$_{22}$ was dissolved in H$_2$O/MeOH (1:1, v/v, pH~3) to yield a final concentration of 5 mM. At high concentrations (5 mM), peptides often instantly form amyloid fibrils. The formation of non-specific aggregates is also often observed in the gas phase for high peptide concentrations. High concentration yields abundant clusters, which can be more easily investigated *via* IM-MS. Thus, the addition of methanol not only supports the solubility of the peptide (at this high concentration), but it also accelerates the evaporation rate of the droplets during the ESI process. It can also prevent the formation of non-specific aggregation during the nESI process, due to a smaller initial droplet size.[69] $_{16}$KLVFFAE$_{22}$ is able to form amyloid fibrils even at a concentration of 500 µM (H$_2$O/MeOH; 1:1, v/v, pH~3). Figure 17 shows the transmission electron microscopy (TEM) image of such amyloid fibrils. Thus, this solvent represents proper conditions for the study of $_{16}$KLVFFAE$_{22}$ fibril formation.
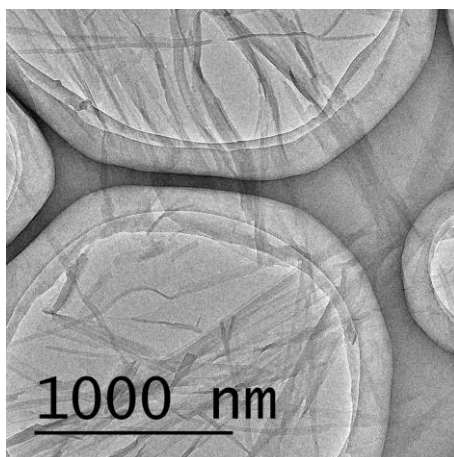
Figure 17: TEM image of $_{16}$KLVFFAE$_{22}$. Amyloid fibrils are formed at 500 μM out of H$_2$O/MeOH (1:1, v/v). The image was obtained after drying the solvent. The circles are the Cu-grid. The image was recorded by Xing Huang (Fritz Haber Institute of the Max Planck Society).

Theoretical molecular dynamic calculations (MD)[68] and X-ray diffraction experiments (XRD)[70] show, that $_{16}$KLVFFAE$_{22}$ fibrils are composed of antiparallel β-strands.[71] Another method which is sensitive toward the formation of β-sheet rich structures is Fourier transform infrared spectroscopy (FT-IR). Especially the amide I vibration which complies the C=O stretching mode, is highly sensitive towards the secondary structure, adopted by peptides and proteins. Parallel β-sheets usually show an amide I feature at around 1610 to 1640 cm^{-1}, whereas a second weak feature at around 1675 to 1695 cm^{-1} is observed for anti-parallel β-strands.[53, 54] This amide I region is unique for β-sheets and other secondary structure motifs (see Table 1). The FT-IR spectra for a 5 mM $_{16}$KLVFFAE$_{22}$ solution (D$_2$O/MeOD; 1:1, v/v) were recorded at room temperature for different incubation times and it is shown in Figure 18. As water yields absorptions within amide I and amide II region (1590 – 1690 cm^{-1}), deuterated solvents were chosen, which significantly shifts the water absorption towards lower wavenumbers.[3, 72]

Figure 18: FT-IR spectra for the amide I region of a freshly prepared ₁₆KLVFFAE₂₂ sample with a concentration of 5 mM in D₂O/MeOD (1:1, v/v) and after, 1 h, 2 h, 4 h, 8 h and 10 h incubation time at room temperature. The feature at around 1625 cm⁻¹ is given by the β-sheet motifs, the peak at around 1670 cm⁻¹ contains α-helical, turns and antiparallel β-sheet motifs.

The FT-IR spectra of the incubated ₁₆KLVFFAE₂₂ solutions show two well-separated features within the amide I region (1625 and 1670 cm⁻¹). These two features are immediately present after dissolving the sample and they do not change over time. The feature at 1625 cm⁻¹ indicates β-sheet rich species, whereas features at around 1670 cm⁻¹ represent other secondary motifs, such as α-helical and β-turn (type II).[51, 53, 54] A classical on-pathway amyloid formation occurs over three stages, i.e. lag-, growth-, and saturation-phase.[1, 19, 20] Thus, the secondary structure content in solution should also change over time. Surprisingly, no relative intensity changes between the features around 1625 and 1670 cm⁻¹ are observable. Since KLFVVAE fibrils are already formed at 500 μM, as mentioned above, the high concentration (5 mM) might immediately lead to the formation of amyloid fibrils. The lag-phase is skipped and the short growth-phase is immediately initiated. For that reason, fibrils are presumably present at the beginning of the experiment and within this saturation-phase no significant changes in the secondary structure is expected. Additionally, after ultrasonification, which was applied to dissolve the peptide (four seconds), can also trigger aggregations an initiate the fibril formation. IM-MS, which can separate different oligomeric states out of an assembly depending on their charge, size, shape and mass,[32] is further employed to explore left oligomeric states in solution. Figure 19 (left panel) shows the mass spectrum (MS) with the presence of several oligomeric states ranging from *m/z* 427 to *m/z* 1707. These range contains the singly charged monomer and dimer, the doubly charged monomer and trimer, the triply charged pentamer and the quadruply charged heptamer.
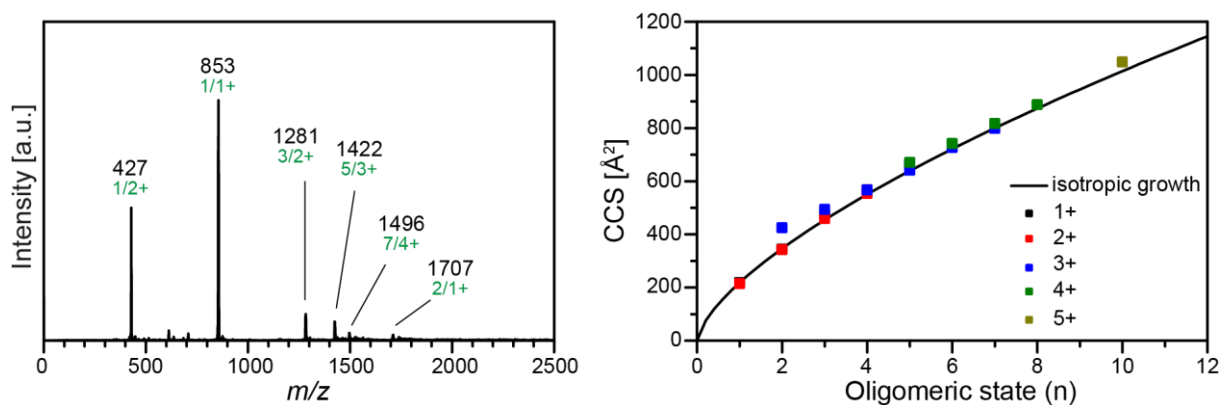
Figure 19: Mass spectrum of $_{16}$KLVFFAE$_{22}$ (left) and measured collision cross-sections (CCS) as a function of the oligomeric state (right). The most pronounced oligomers are labeled with their respective n/z (oligomer number to charge) ratio (green numbers) (left). The solid line describes a theoretical isotropic growth (i.e. spherical) pattern, the squares represent all oligomers, which were found.

The resolution of the mass analyzer is, however, too low to unambiguously assign higher oligomeric states based on their isotopic pattern appearing at the same m/z value. In the case of a high resolution TOF, ^{13}C satellites are observed next to the monoisotopic peak. Depending on the charge (z) of the species, this satellites show a distance of +1/z regarding to the monoisotopic peak. For example, a singly charged trimer (3/1) with a certain m/z would yield a satellite peak in a distance of 1. If there is a higher oligomeric state of this certain m/z, e.g. a doubly charged hexamer (6/2), the distance between the peaks is only 0.5. In addition, mass spectrometry (MS) on its own is not able to distinguish between individual conformations with the same m/z ratio. IM-MS, on the other hand, can be used to separate species with identical m/z ratio based on their differences in size, shape, charge and mass. Figure 20 shows exemplary the arrival time distribution (ATD) plot of two multiple conformation forming oligomeric states of $_{16}$KLVFFAE$_{22}$ (the 3/2+ and the 5/3+). Both species contain a compact (red line) and an extended form (blue line), which is supported by the determined CCS values. For the compact conformer of the 3/2+, a CCS value of 460 Å^2, and for the extended one a value of 475 Å^2 were determined. For the two conformers of the 5/3+ oligomeric state, a CCS of 641 Å^2 (compact) and 664 Å^2 (extended) were determined. Due to the ability to separate oligomers with the same m/z ratio, a signal for the 6/4+ oligomer is observable at around 13 to 15 ms, which also indicate a compact and an extended conformational form (Figure 20, left panel).
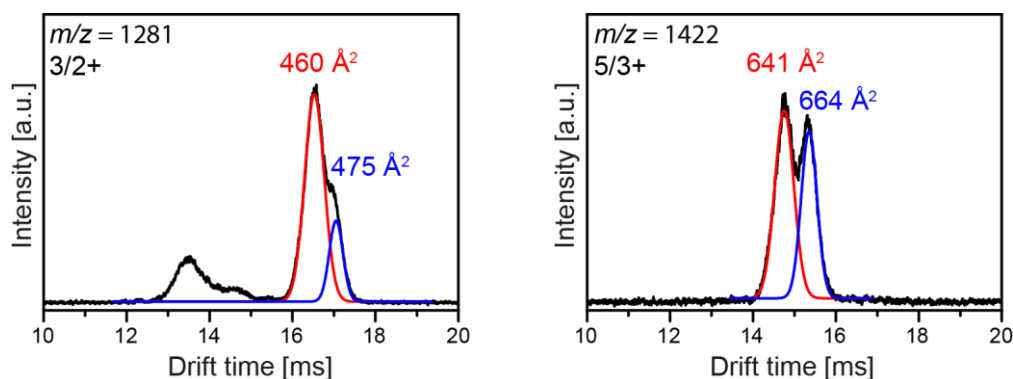
Figure 20: ATD of 3/2+ and 5/3+ (n/z) of the $_{16}$KLVFFAE$_{22}$ peptide. Left panel: The shoulder indicates an extended conformer for 3/2+. Furthermore, a 6/4+ is observable where the peak shape also indicated an extended and compact conformer. Right panel: A double peak was observed for 5/3+, which indicates the existence of a compact and an extended conformer. The colored lines represent the *Gaussian* fits to determine the conformers, whereas the red one represents the compact, the blue one the extended form. The black line represents the recorded raw data.

For all observed species, an ATD plot was recorded and the collision cross-section (CCS) of every oligomeric state was determined (see Appendix for all values and ATD plots). The CCS is plotted as a function of the oligomeric state (n) to show the growth trend of the observed oligomers shown in Figure 19 (right panel). The solid line represents an ideal theoretical isotropic growth behavior, following the equation $\Omega_n = \Omega_1 \cdot n^{2/3}$, where Ω_1 is the CCS of the monomer and *n* the oligomeric number. The molecules are assumed as ideal spheres and their packing represents the closest package of the molecules, which is possible[40, 41] (see Methods chapter). Oligomers, exhibiting an experimental CCS similar to the predicted isotropic value, adopt compact spherical conformations, which usually represent turn-like or unordered structures. In rare cases, the observed growth trend of the oligomeric states can also be below the theoretical trend line, which indicates that the monomer does not have the most compact structure. Extended oligomeric states which deviate from this isotropic growth model, are often partially structured and form helical or β-sheet rich conformations. An extended conformation might be, however, also a result of a high charge density, which leads to an unfolding of the oligomer in the gas phase. Figure 19 (right panel) shows a variety of compact (experimental CCSs close to the isotropic ones) $_{16}$KLVFFAE$_{22}$ oligomers starting from the singly charged monomer (n/z = 1/1+) up to the quintuply charged decamer (n/z = 10/5+). These compact oligomers presumably adopt turn-like or unordered conformations. Interestingly, also few more extended oligomers such as the triply charged dimer (n/z = 2/3+) are observed. These more extended conformations are, however, most likely formed due to *Coulomb* repulsions, occurring due to the high charge density. IM-MS provides reliable data on the

tertiary level, whereas secondary structure information can be obtained *via* gas-phase IR spectroscopy. However, individual secondary structure motifs often yield overlapping characteristic features, and therefore deconvolution procedure is routinely applied especially in condensed phase to deduce relative contents of certain motifs.[55] In the gas phase, relative populations cannot be directly obtained from infrared multiple photon dissociation (IRMPD) spectra without making assessments about the oscillator strengths. The IRMPD process contains complex multiple photon absorptions and the resulting IR intensity is not linear with the number of absorbed photons.[10] Instead, the gas-phase deconvolution rather represents a qualitative assignment of intensity fractions of a specific structural motif, which was reported recently.[3, 10] However, the TOF detector cannot differentiate between precursor and fragments, when different oligomeric states of the same m/z ratio (e.g. 6/3+, 4/2+) are irradiated and break into fragments which also have the same m/z ratio. In addition, secondary fragmentation pathways of generated fragments are possible, which might lead to saturated spectra. Hence, IRMPD spectra of those species are difficult to record. To avoid this problem, only the lowest charge states of the oligomers were measured. The singly charged monomer of $_{16}$KLVFFAE$_{22}$ was not measured in this thesis, because there was no evidence of β-sheet rich structures in a previous measurement. Figure 21 shows the gas-phase IRMPD spectra of drift-time- and m/z- selected species. All IRMPD spectra show two well-pronounced bands ranging from 1480 to 1550 cm^{-1} (amide II, N-H bending mode) and 1610 to 1700 cm^{-1} (amide I, C=O stretching mode). The latter is known to be more sensitive towards the secondary structure of peptides and proteins.[3, 11] All spectra were measured in the range of 1400 – 1800 cm^{-1} and the amid I region was fitted with multiple *Gaussian* curves, where potential antiparallel β-sheets and turn-like features are labeled in red and blue, respectively. The signal-to-noise ratio during the measurements was low, especially for the large oligomers. In general, all spectra exhibit the amide I feature at around 1670 cm^{-1}, which is indicative for turn-like structures. The deconvolution of the spectra did not provide significant β-sheet content. For the larger states (e.g. extended 5/3+, 7/3+ and 7/4+), the signal-to-noise ratio is very low, which makes the deconvolution process difficult and might lead to misinterpretations for the β-sheet content.
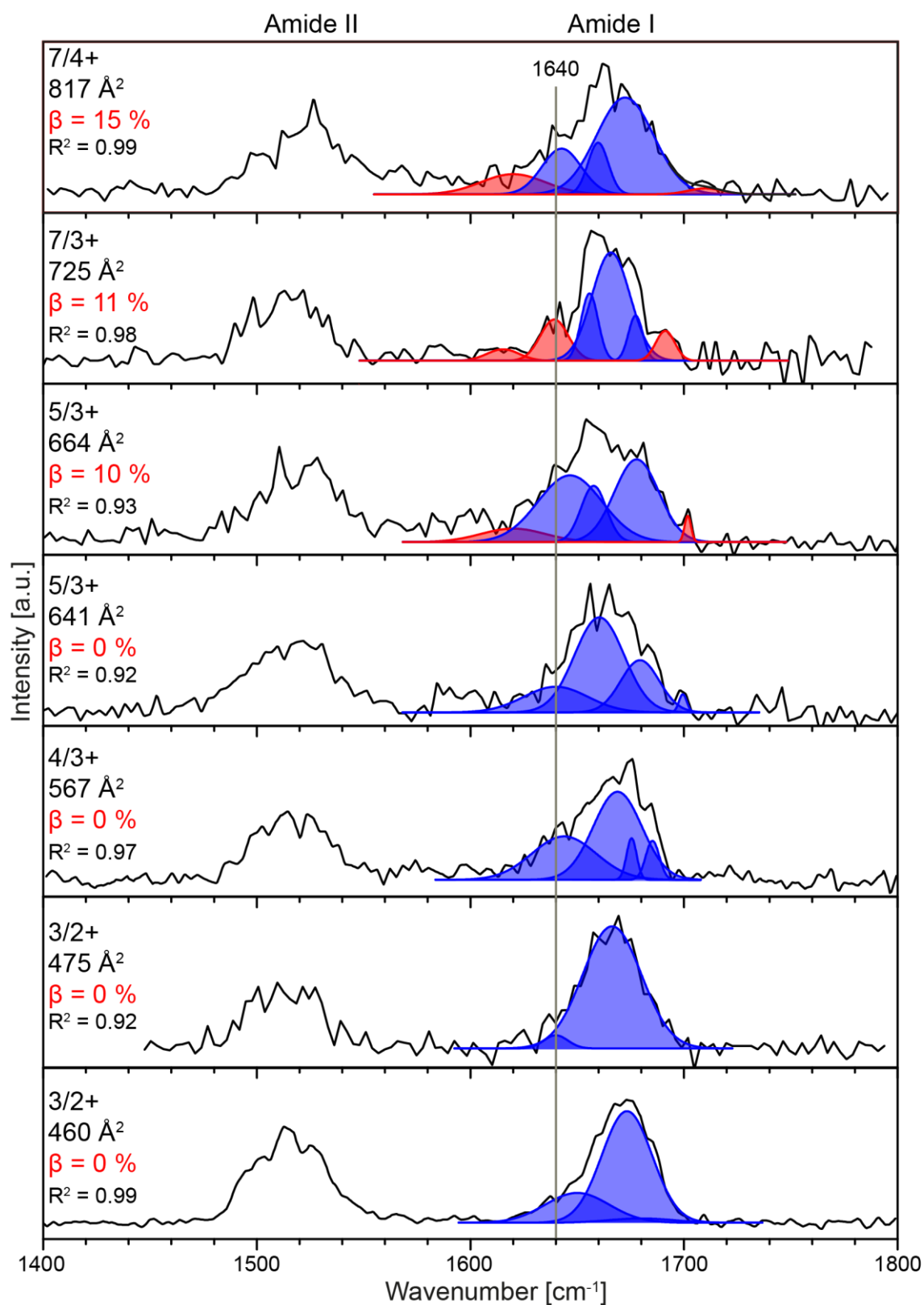
Figure 21: IRMPD spectra of the measured 16KLVFFAE22 oligomers. The amide I region was fitted with multiple *Gaussians*. Each representing an individual secondary structure motif. β-sheet (1610-1640 and ~1690 cm⁻¹) motifs are red and other structural motifs blue. The accuracy of the fits is provided in R².

Additionally, a slightly but not significant red shift (to lower wavenumbers) was observed for the amide I feature for larger oligomers. Thus, monomer data were not recorded for verification. The experimental CCS values of these oligomers are, however, in good agreement with the theoretical values for spherical, compact conformations. Thus, small non-significant β-sheet IR contents[3] in combination with a compact conformation do not reflect highly extended steric-zippers, which are commonly formed by amyloidogenic sequences. The gas-phase results show spherical unstructured aggregates, whereas condensed-phase experiments indicate high amount of ß-sheet rich species. The discrepancy between gas phase and condensed phase might be a result of an insufficient transition of large oligomers within the IM-MS instrument. Higher oligomeric states, which might exhibit a high β-sheet content, might therefore not be observed. Furthermore, β-sheet rich oligomers probably aggregate too fast into fibrils, and consequently they cannot be transferred into the gas phase.

6.2 C-terminal Fragments of Abeta

Recent hydrogen/deuterium exchange experiments (HDX) have shown that the C-terminus of Abeta does not exhibit a significant H/D exchange. Thus, it can be concluded that the C-terminus is involved in strong hydrogen bonds, which do not interchange. These strong hydrogen bonds are usually formed within highly structured aggregates and therefore the C-terminus represents an important domain, which is directly involved in the aggregation pathway.[51, 73] Furthermore, NMR experiments indicate, that the C-terminus undergoes a back folding to the middle region of Abeta as shown in Figure 22. Additionally, the formation of a salt bridge between aspartic acid (Asp 23) and lysine (Lys 28), which provides the turn (depicted in black), is assisted by this back folding. As shown, the C-terminus is mainly hydrophobic (green parts) and the (red) dashed lines in the illustration describe the side-chain packing between specific amino acids. For example, between methionine (Met 35) and alanine (Ala 42), a side-chain interaction (grey dashed line) is assumed in Abeta 42. For glycine (Gly 38), which does not contain a functional side chain, a molecular contact (such as Van-der-Waals interactions) with phenylalanine (Phe 19) is proposed.[30, 51]
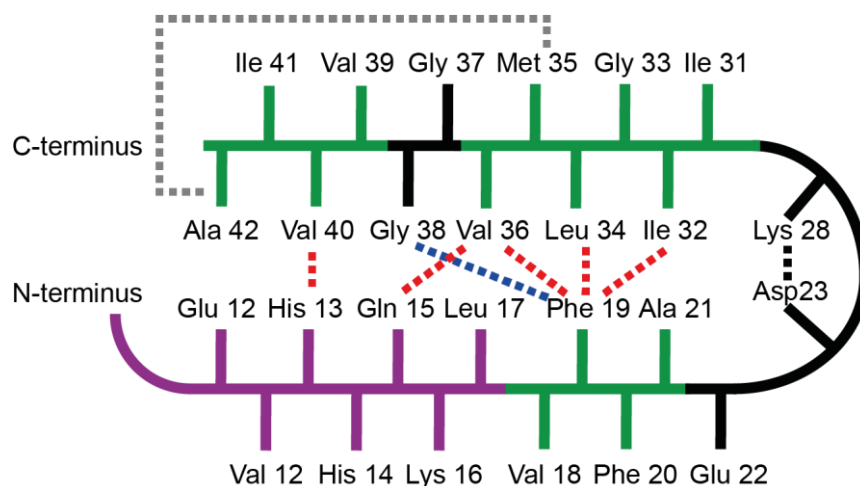

Figure 22: Sketch of the structural constrains of a monomeric Abeta 42 strand in fibrils. Due to a turn conformation, the C-terminus interacts with the middle part of the peptide. The purple region indicates the unstructured N-terminus; the green sequences are hydrophobic. The red and grey dashed lines indicate side-chain packing of the amino acids, the blue dashed line stands for the molecular contact (Van-der-Waals interactions)[30] between Phe 19 and Gly 38. The turn conformation is additionally stabilized due to hydrophobic interactions and the salt bridge between Asp 23 and Lys 28 (black dashed line).[51]

These C-terminal interactions probably have a huge influence for the aggregation of Abeta. In addition, the differences in the aggregation behavior and cytotoxicity of Abeta 40 and 42 might

be a result of the last two additional amino acids, namely isoleucine (Ile 41) and alanine (Ala 42). Therefore, individual fragments derived from the C-terminus were investigated in order to understand their influence on the aggregation pathway.

6.2.1 C-terminal Fragment - [37]GGVVIA[42]

The first investigated C-terminal peptide is [37]GGVVIA[42], which describes the last six amino acids of the Abeta 42 peptide. This sequence was shown to form amyloid fibrils (Figure 23) in aqueous solution (29 mM), containing ammonium sulfate (2 M) and hexamine cobalt(III) chloride (0.1 M).[5]
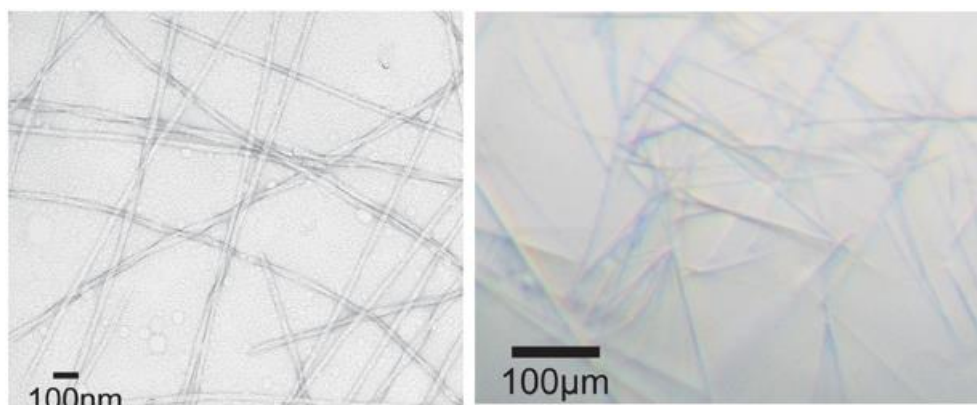

Figure 23: TEM images of the [37]GGVVIA[42] fibrils. The images were obtained using an aqueous solution (29 mM) containing ammonium sulfate (2 M) and hexamine cobalt(III) chloride (0.1 M), in a ratio of 5:4:1 (v/v). Images adapted from Sawaya ET AL.[5]

For those fibrils, X-ray diffraction experiments (XRD) and several theoretical calculations provide a parallel β-sheet structure.[5, 71, 74, 75] The fibrils are built up by class 4 steric-zippers with a face-to-back orientation of the strands and form the orthorhombic space group P2$_1$2$_1$2.[5] In this thesis, the peptide was also dissolved in H$_2$O/MeOH (1:1, v/v, pH~3) and their deuterated analogues in a concentration of 5 mM, for the reason discussed above. FT-IR spectra (Figure 24) show the presence of a band at around 1625 cm^{-1}, which clearly represent β-sheet rich structures in solution (no TEM image recorded for this sample). In contrast to [16]KLVFFAE[22] (discussed above), small variants between the relative intensities of the features inside the amide I band are observed over a period of time. This indicates that presumably

soluble β-sheet rich oligomers are immediately present, which can further evolve to amyloid fibrils. Thus, the used sample concentration, although lower as for the fibril growth in literature[5], was high enough to initiate the growth-phase.
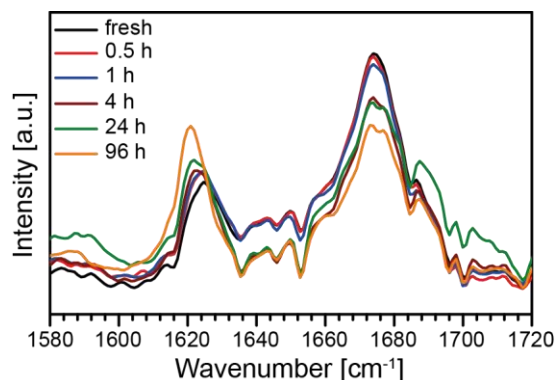

Figure 24: FT-IR spectra of the amide I region of the fresh, the 1 h, 2 h, 4 h, 8 h and 10 h incubated $_{37}$GGVVIA$_{42}$ sample at room temperature with a concentration of 5 mM in D$_2$O/MeOD (1:1, v/v). The feature at around 1620 - 1625 cm^{-1} is caused by β-sheets. The feature around 1675 cm^{-1} represents turn motifs. The intensities change over time, which assumes the formation of β-sheet rich oligomers.

To get more structural information of individual oligomeric states and to determine the CCS values of each, the sample was investigated in the gas phase in a H$_2$O/MeOH (1:1, v/v) solution using IM-MS. In the mass spectrum shown in Figure 25 (left panel), several oligomeric states were observed. In addition, impurities of the $_{38}$GVVIA$_{42}$ stop sequence with high charge states and trifluoroacetic acid (TFA) adducts were observed (green asterisks in Figure 25). The stop sequence may originate from an inefficient coupling during the solid phase peptide synthesis (SPPS). Efforts to remove them were unsuccessful. Due to the fact, that $_{38}$GVVIA$_{42}$ and $_{37}$GGVVIA$_{42}$ do not give different signals in a diode array detector (DAD, 220 nm), and their containing similar hydrophobicity, it was not possible to remove the fragment during the clean-up process *via* preparative HPLC. As for the $_{16}$KLVFFAE$_{22}$ sample, larger oligomeric states could not be observed in the mass spectrum. Hence, the ATD for each separated oligomer was recorded to compare the growth trend of the oligomeric states with their theoretical isotropic growth (Figure 25).
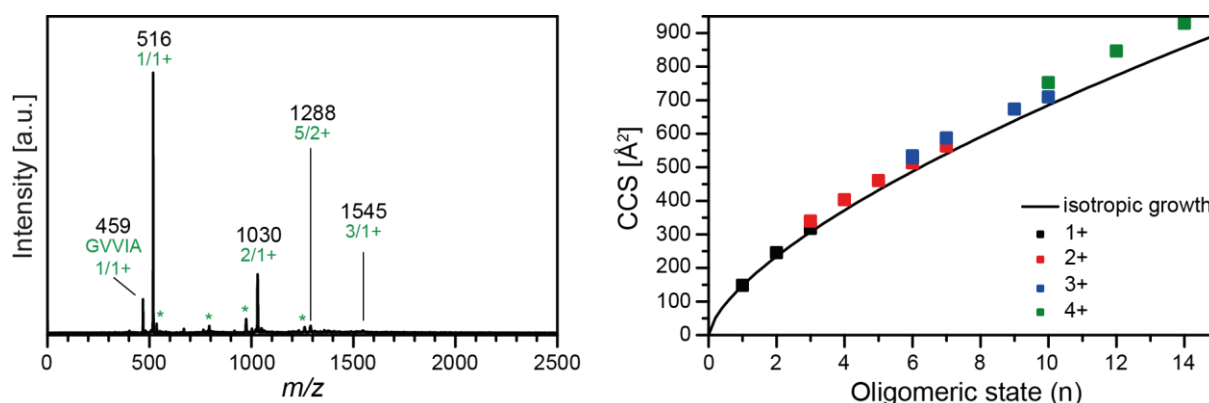
Figure 25: Left panel: The mass spectrum of $_{37}$GGVVIA$_{42}$ with peaks arising from $_{38}$GVVIA$_{42}$ oligomers and TFA adducts (shown with green asterisks *). Peaks are labeled with their n/z ratio. Right panel: measured CCSs against oligomeric state (n) plot. The black line describes the ideal isotropic growth pattern, the squares represent the oligomers which were found.

As shown in Figure 25 (right panel), oligomeric states up to the quadruply charged 14-mer were observed. The singly charged states (e.g. 1/1+, 2/1+ and 3/1+) are in line with the theoretical model (solid line), which indicates unordered or turn-like structures. Higher charge states, however, deviate significantly from the theoretical line. This deviation starts with the doubly charged trimer (3/2+) and increases for larger oligomers, which gives the evidence of highly structured oligomers which presumably contain β-sheet motifs. Especially the quadruply charged oligomers reveal a distinct deviation from the isotropic model, which could be caused by repulsive charge interactions. However, the deviation is in line with the observed FT-IR results which support the assumption for β-sheet rich oligomers. A more reliable information about the secondary structure of individual oligomers is obtained by measuring their respective IR spectra in the gas phase (Figure 26 and Figure 27). In all IR spectra, the amide I and II band is well pronounced. Furthermore, a comparison of the IRMPD spectrum of the singly charged monomer (1/1+) with the spectra of higher oligomeric states shows, the amide I and II band is significantly shifted for higher oligomers. Figure 26 shows the comparison of the two amide bands between the singly charged monomer (1/1+) and trimer (3/1+). Here, a shift around 25 cm^{-1} (amide I) and around 15 cm^{-1} (amide II) are observed, which increases for higher oligomers. The shifts are caused due to the intensive hydrogen bonds, whereby the N-H binding (amide II) gets stronger and this leads to a shift to higher wavenumbers (blue shift). Furthermore, the C=O bond gets weaker, which leads to a shift to lower wavenumbers of the amide I feature (red shift). In general, this trend can be observed for all larger oligomers compared to the monomers.
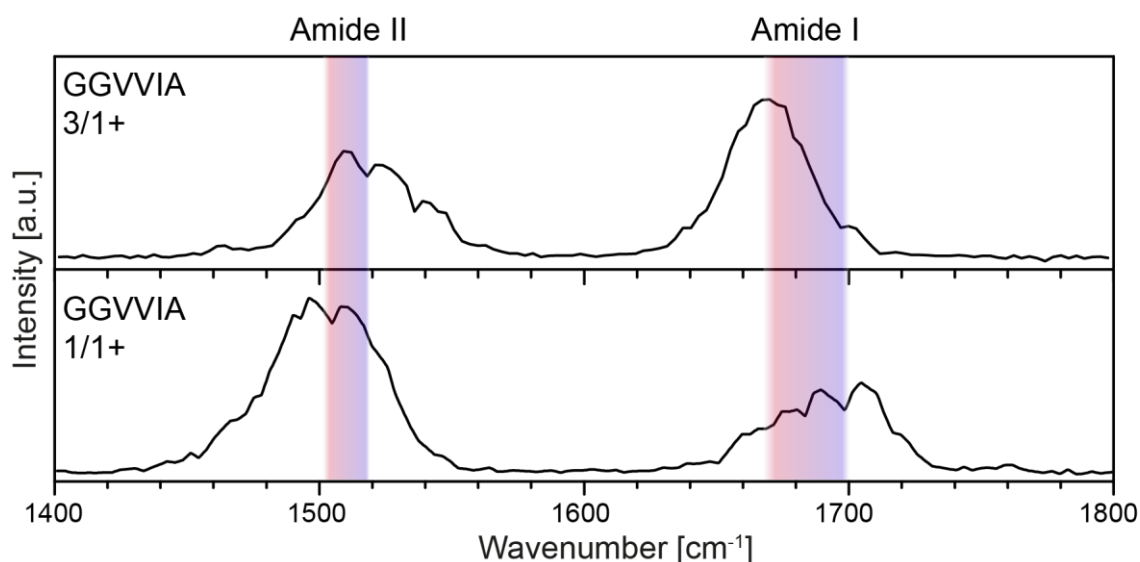
Figure 26: Comparison of a single charged monomer and trimer of $_{37}$GGVVIA$_{42}$. The amide I band is corresponding to the C=O stretching mode of the carbonyl group, the amide II represents the N-H bending mode. Through the formation of a hydrogen-bond network especially for larger oligomers, the amide II band is blue shifted due to the increased bond-strength in the N-H. Therefore, the carbonyl group interacts stronger with hydrogen donors, which leads to a weaker C=O bond strength and to the red shift of the amide I. This effect is observed for all measured peptides especially for the comparison of monomers with larger oligomers.

The comparison of the singly charged dimer (2/1+) and singly charged trimer (3/1+) (Figure 27) shows that both oligomers do not contain β-sheet motifs, which is in agreement with the isotropic model. The larger, doubly charged oligomers as well as the triply charged decamer (10/3+), which all deviated from the isotropic line, exhibit β-sheet characteristic features below 1640 cm^{-1}. Additionally, the spectrum of 3/2+ exhibits a feature at around 1715 cm^{-1}. This region is typical for the C=O stretching mode for free carboxyl groups (COOH).[50] For monomers, this mode is typically more pronounced due to missing hydrogen-bond interactions. Due to the high charge density in 3/2+, repulsive interactions could lead to an extended structure. Thus, one COOH-group might not be involved in hydrogen bonding, which provides an additional feature (at ~1715 cm^{-1}) for weakly-interacting C=O stretching mode. Moreover, the 7/3+ oligomer shows also a more pronounced band at ~1715 cm^{-1} compared to the 7/2+, which supports the previous assumption of a charge repulsion effect. Furthermore, the larger oligomers, especially the triply charged heptamer (7/3+) and dodecamer (10/3+) contain a β-sheet content of twelve and eleven percent, respectively. In general the observed β-sheet content is, as in case of the $_{16}$KLVFFAE$_{22}$ oligomers, not significant.[3] The experimental growth trend on the other hand shows an unfolding of the oligomers, like proposed for β-sheet rich structures. The deviation from the isotropic growth and the non-significant β-sheet content

indicate, however, that the formed oligomers may represent on-route species for amyloid fibrils for this peptide.
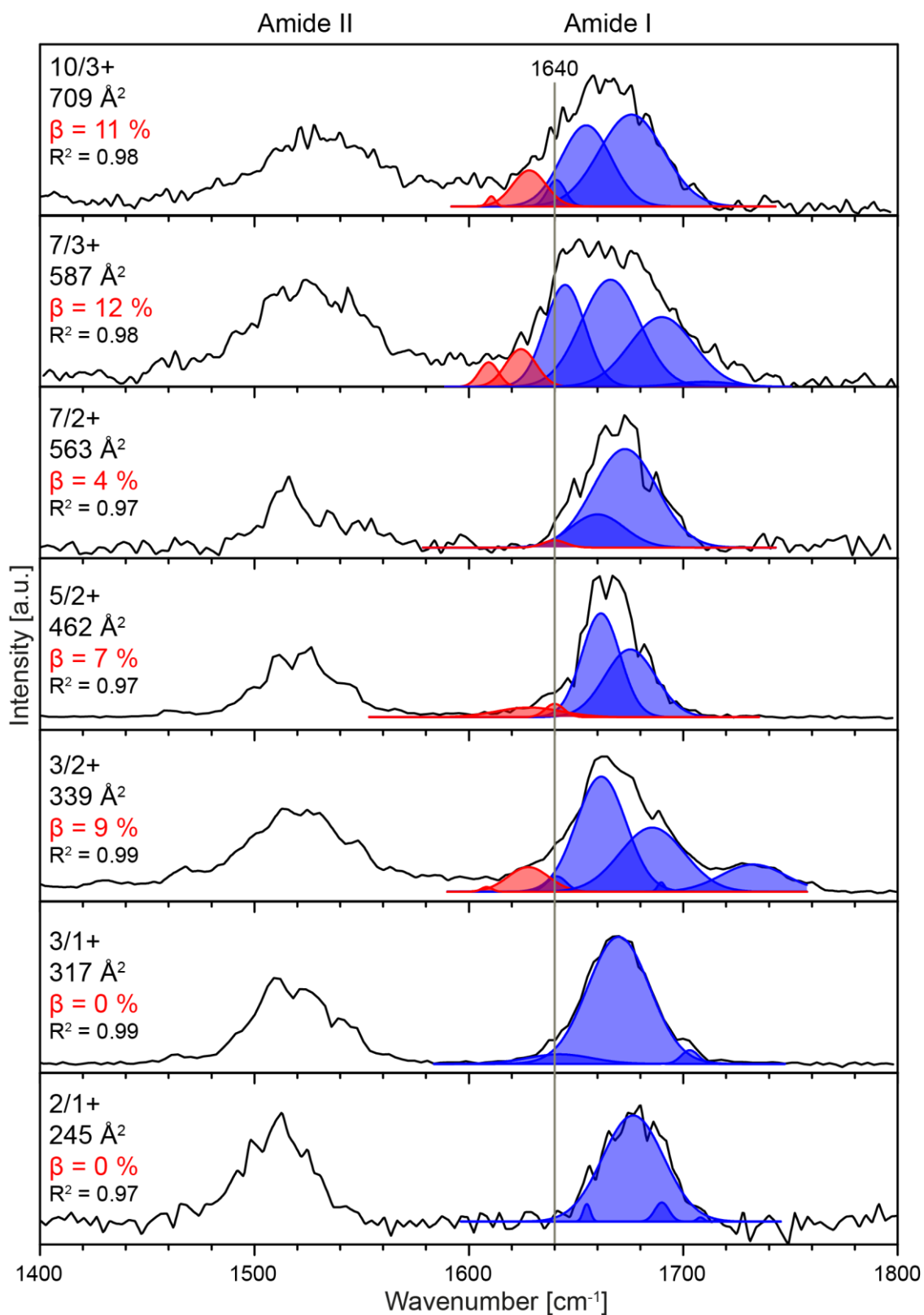
**Figure 27:** IRMPD spectra of the measured ₃₇GGVVIA₄₂ oligomers. The amide I region was fitted with multiple *Gaussians*. Each *Gaussian* represents an individual secondary structure motif. β-sheet (1610 - 1640 cm⁻¹) motifs are red and other structural motifs blue. The accuracy of the fits is given in R².

In summary, the gas-phase IRMPD spectra and the condensed-phase spectra for $_{37}$GGVVIA$_{42}$ are contradictory. The condensed-phase FT-IR spectra show a relatively high content of β-sheet motifs (Figure 24), which increase over time. Gas-phase analyses show directly unfolded oligomers (growth trend line), which contain only a small content of β-sheet motifs (IRMPD). Otherwise, these oligomers can further form larger, β-sheet rich aggregates which may be responsible for changes in intensity in the condensed phase over time. However, it is challenging to transfer those larger oligomers into the gas phase and to investigate them by IRMPD spectroscopy.

6.2.2 C-terminal Fragment - $_{35}$MVGGVV$_{40}$

The second investigated C-terminal fragment $_{35}$MVGGVV$_{40}$ represents the last six amino acids of Abeta 40. As mentioned above, Abeta 42 just differs in two amino acids, but was shown to aggregate much faster, whereas Abeta 40 might even be cytoprotective due to the inhibition of the Abeta 42 oligomerization.[4, 65] $_{35}$MVGGVV$_{40}$ fibrils (Figure 28, right panel) are built up by class 8 steric zipper motifs. Remarkable for this antiparallel class is, that two possibilities exist to form the steric-zipper in the up-down orientation of the strands.[5, 71, 74, 76] Their formation highly depends on the conditions.
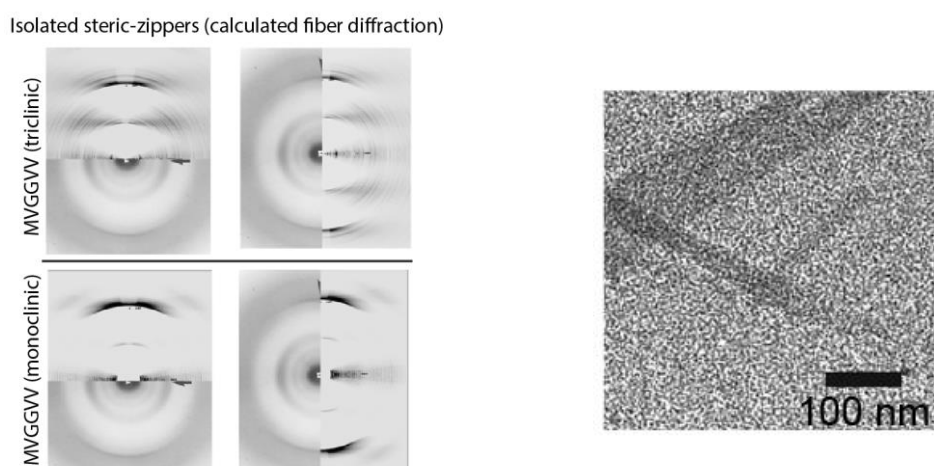
**Figure 28:** Left panel: The X-ray diffraction (XRD) pattern of the peptide $_{35}$MVGGVV$_{40}$ in the mono- and triclinic form. Right panel: TEM image of the $_{35}$MVGGVV$_{40}$ fibrils. Picture taken from Sawaya ET AL. and Colletier ET AL.[5, 71]

To obtain the triclinic crystal (Form 1) which forms the space group P_1, the peptide was incubated in a ratio 1:1 (v/v) of the aqueous peptide (53.5 mM) and an aqueous solution of $CaCl_2$ (0.02 M), 30 % of 2-methyl-2,4-pentanediol (MPD) and sodium acetate (0.1 M). For the monoclinic crystal (Form 2) which forms the $P2_1$ space group, the peptide solution (53.5 mM) was mixed with the aqueous solution of $CaCl_2$ (0.2 M), 20 % of 2-propanol and sodium acetate (0.1 M) in the ratio 1:1. For both solvents the pH-value was adjusted to 4.6.[5, 71] In Figure 28 a TEM image of the formed fibrils and the obtained XRD pattern of both crystal structures of $_{35}MVGGVV_{40}$ are shown.[5, 71] To be consistent to the above discussed peptides, $_{35}MVGGVV_{40}$ was also dissolved in H_2O/MeOH (1:1, v/v) to yield a final concentration of 5 mM. The baseline corrected FT-IR spectra in D_2O/MeOD (1:1, v/v) were recorded to study the averaged secondary-structure content present in solution and are shown in Figure 29. In addition to the freshly dissolved sample, spectra were recorded after 0.5 h, 1 h, 24 h, 48 h and one week of incubation time.
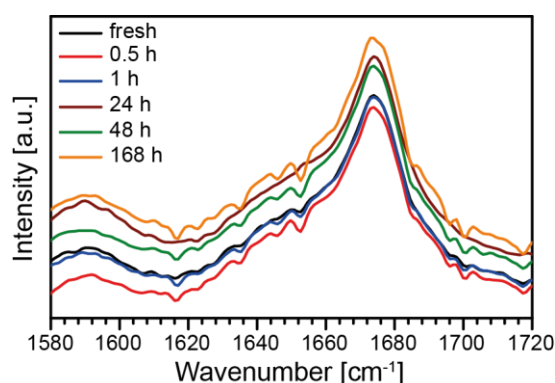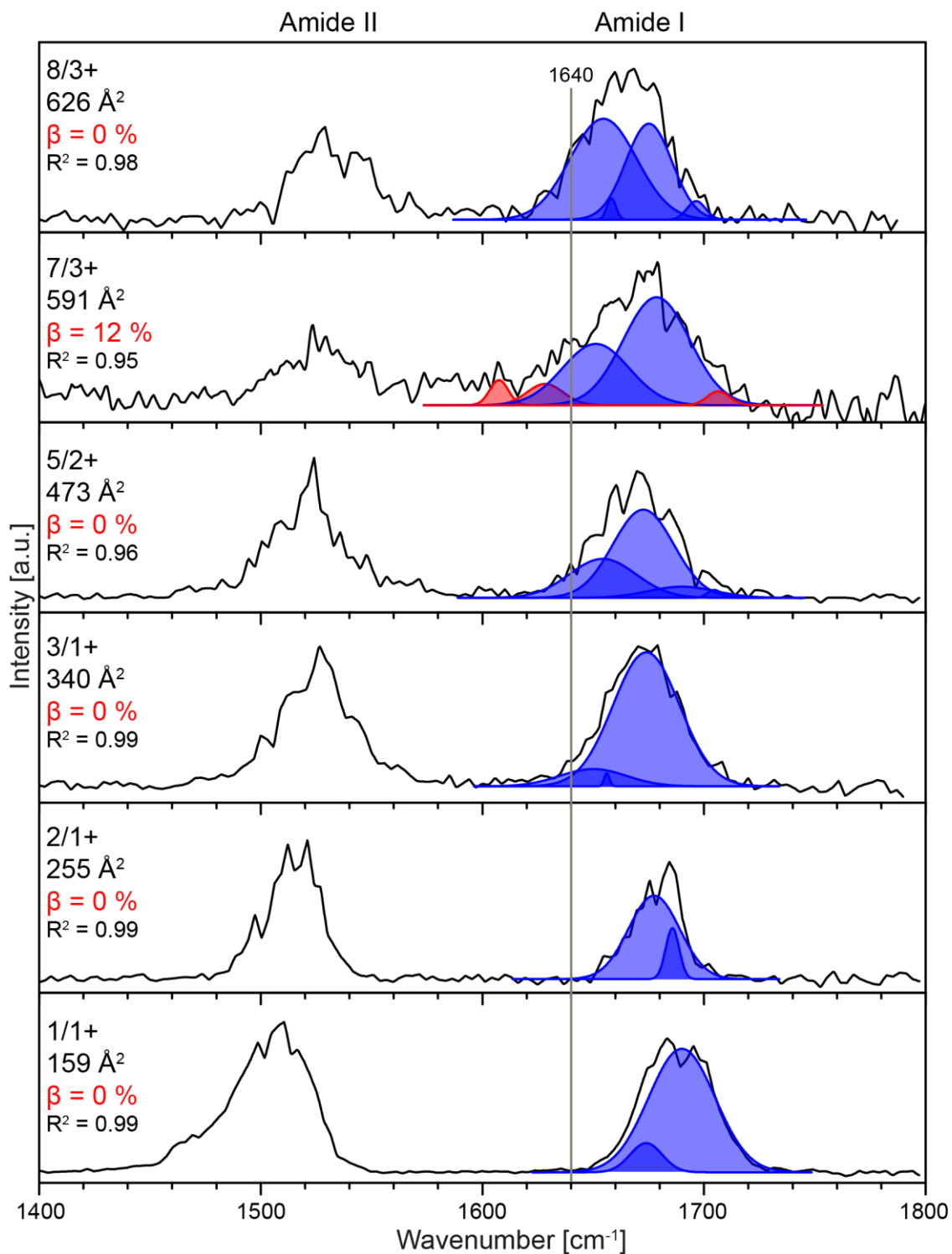

Figure 29: FT-IR spectra of the amide I region of the fresh, the 0.5 h, 1 h, 24 h, 48 h and one week incubated $_{35}MVGGVV_{40}$ at room temperature with a concentration of 5 mM in D_2O/MeOD (1:1, v/v). Only one feature at around 1675 cm^{-1} was observed for all measurements.

Here, only one broad band at ~1675 cm^{-1} was observed and its intensity did not change within one week. This feature represents the presence of turn-like structures in solution. The characteristic feature for β-sheet motifs at around 1625 cm^{-1} is not present. The addition of methanol might inhibit the aggregation of the peptide and due to different conditions (concentration, solvents) compared to a previous study,[5] no β-sheet rich fibril formation is observed. The formation of the less structured $_{35}MVGGVV_{40}$ oligomers was further studied in the gas phase *via* IM-MS techniques using a 5 mM (H_2O/MeOH, 1:1, v/v) sample solution.
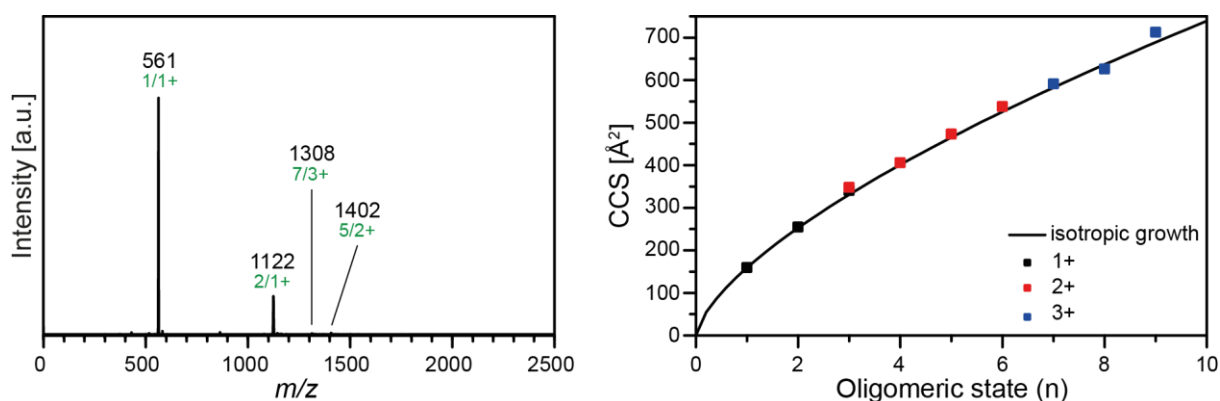
Figure 30: Left panel: The mass spectrum of $_{35}$MVGGVV$_{40}$ is shown. Peaks are labeled with their *m/z* (black) and n/z (green) ratio. Right panel: Determined CSS *versus* oligomeric state (n) plot. The black line describes the ideal isotropic growth pattern, the squares represent all found oligomers. The growth trend of the observed oligomers fits the isotropic model well.

The mass spectrum (Figure 30, left panel) shows less oligomeric states compared to the previous measured peptides. IM-MS also does not indicate the presence of multiple conformers. For $_{35}$MVGGVV$_{40}$, oligomeric states up to the n/z of 9 were detected as shown in Figure 30 (right panel). The experimental CCSs follow the theoretical isotropic growth pattern which indicate compact spherical aggregates. Furthermore, the respective gas-phase IRMPD spectra (Figure 31) also do not show amide I features, which would represent β-sheet structures. Instead an amide I frequency at 1660 to 1685 cm^{-1} is observed, which further supports turn-like aggregates. The IR spectrum of the 7/3+ oligomer shows weak features around 1620 cm^{-1}. The spectrum has, however, a low signal-to-noise ratio, which makes a reliable deconvolution challenging. Both the condensed-phase as well as the gas-phase experiments show that no highly structured or extended aggregates are formed for $_{35}$MVGGVV$_{40}$ under the conditions employed. This is unexpected, because $_{35}$MVGGVV$_{40}$ contains multiple highly hydrophobic amino acids, which usually support the aggregation into amyloid fibrils. The results, however, clearly demonstrate that the last two residues (Ile and Ala) of the full-length Abeta have a tremendous impact on the aggregation behavior. For the last six amino acids of Abeta 42 ($_{37}$GGVVIA$_{42}$) a rapid aggregation into amyloid fibrils was observed, whereas the last six amino acid fragment ($_{35}$MVGGVV$_{40}$) of the cytoprotective Abeta 40 were shown to form compact, unstructured, turn-like oligomers. To get more information which of those two last amino acids in Abeta 42 (Ile or Ala) play a major role for the aggregation of Abeta 42, additional C-terminal fragments of Abeta were investigates.

Figure 31: IRMPD spectra of the measured $_{35}$MVGGVV$_{40}$ oligomers. The amide I region was fitted with multiple *Gaussians* to determine the β-sheet content (red areas). The blue areas define other secondary structure features like turn-like structures etc. To indicate the accuracy of the fits, the R-square (R^2) values are given.

6.2.3 C-terminal Fragment - $_{35}$MVGGVVIA$_{42}$

The last two chapters have shown, that the last six amino acid fragments of Abeta 40 ($_{35}$MVGGVV$_{40}$) and of Abeta 42 ($_{37}$GGVVIA$_{42}$) have considerably different aggregation behaviors at the investigated solvent conditions. $_{35}$MVGGVV$_{40}$ only forms compact, amorphous oligomers, whereas $_{37}$GGVVIA$_{42}$ aggregates very quickly into amyloid fibrils. This observation is in line with the assembly characteristics of the respective full-length Abeta sequences. It is, however, reported, that the methionine (Met) residue has a significant influence on the aggregation behavior of both, Abeta 40 and Abeta 42. The Met oxidation inhibits the amyloid fibril formation *in vitro*.[77] Thus, in order to account for possible influence of the Met residue on the aggregation behavior (inhibition effect), the previous Abeta 42 fragment was extended by Ile and Ala ($_{35}$MVGGVVIA$_{42}$). This octapeptide is also known to form amyloid fibrils *in vitro* (Figure 32). X-ray diffraction (XRD) experiments have shown, that these amyloid fibrils are composed of either parallel or antiparallel β-strand motifs, forming two different classes of steric-zippers depending on the conditions.[71] The first belongs to the triclinic space group P1 (Form 1), whereas the second is defined by the monoclinic P2$_1$ space group (Form 2). The triclinic form is built up by parallel orientated β-sheet strands (class 2 steric-zipper), whereas the monoclinic form is build up by antiparallel β-sheet strands (class 7 steric-zipper).
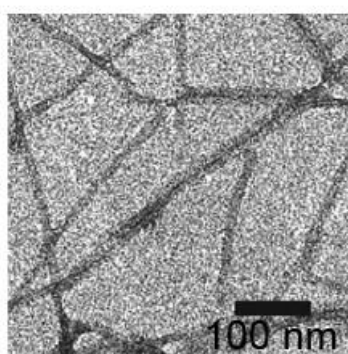
Figure 32: TEM image of $_{35}$MVGGVVIA$_{42}$ showing amyloid fibrils. Picture adopted from Colletier ET AL. [71]

The $_{35}$MVGGVVIA$_{42}$ octapeptide was also dissolved in H$_2$O/MeOH (1:1, v/v). Immediately after dissolving the peptide, the formation of insoluble aggregates is observed. The FT-IR analysis further confirms abundant features at ~1625 cm^{-1}, indicating the presence of β-sheet

structures (Figure 33). Interestingly, the feature at ~1625 cm^{-1} also increases in intensity over time. This indicates that the peptide still evolves higher β-sheet rich aggregates after dissolving.
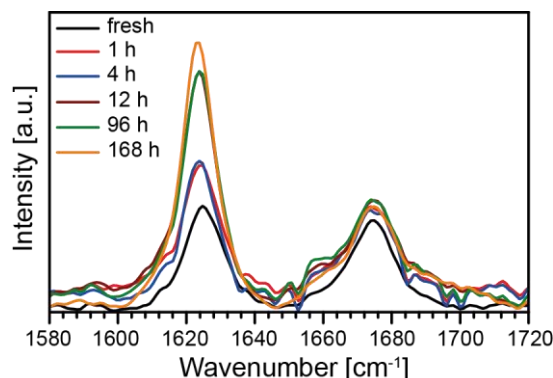
Figure 33: FT-IR spectra showing the $_{35}$MVGGVVIA$_{42}$ (5 mM in D$_2$O/MeOD, 1:1, v/v) at room temperature. The feature at around ~1625 cm^{-1} arises due to β-sheet motifs, whereas features around ~1675 cm^{-1} indicate turn-like structures.

IM-MS was further employed to obtain structural information of these oligomers which were present in solution. The recorded MS only shows one abundant peak at *m/z* 745, which corresponds to the singly charged monomer. (Figure 34, left panel). However, the IM-MS analysis (ATD) can differentiate between three present oligomeric states (1/1+, 2/2+, and 3/3+) as shown in Figure 34 (right panel).
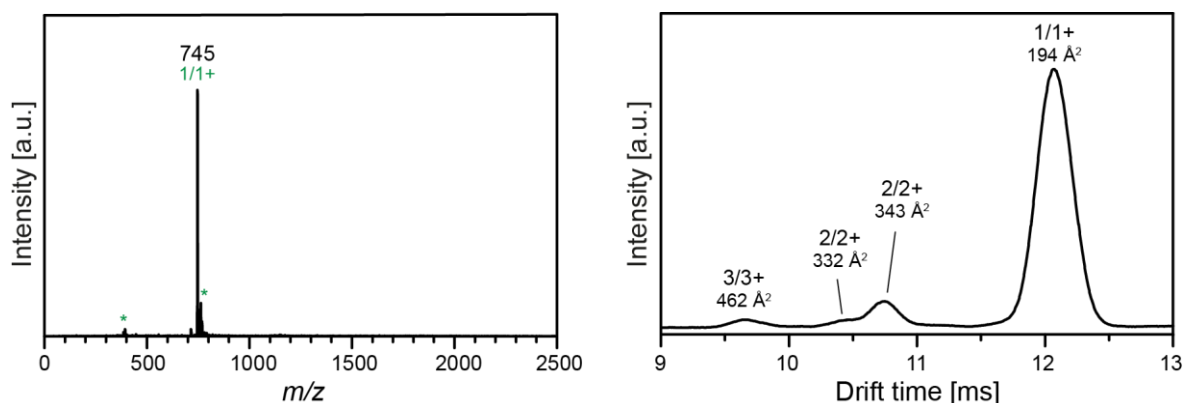
Figure 34: Left panel: The MS of $_{35}$MVGGVVIA$_{42}$ is shown. Only one well pronounced signal was observed and small unidentified impurities (green asterisks *). Right panel: Arrival time distribution (ATD) of the selected *m/z* 745. Three oligomeric states were observed, which could be identified as the 1/1+, 2/2+ and 3/3+. The ATD provides a broad signal for the 2/2+ which indicated an extended and compact conformer. The provided collision cross-sections are given in Å^2.

Their experimental collision cross-sections (CCSs) follow the expected values for compact, spherical aggregates ($\Omega_n = \Omega_1 \cdot n^{2/3}$). This is in contrast to the condensed-phase results, which show the formation of β-sheet aggregation over time. Furthermore, no changes in relative intensities or the formation of higher oligomers are observed in IM-MS. The sequence immediately forms insoluble aggregates, which prevents an efficient transfer into the gas phase. Furthermore, the rapid aggregation behavior accelerates the formation of oligomers, evolving into amyloid fibrils. As a consequence, only the monomer to trimer is left in solution and observed in the IM-MS experiment. The data clearly demonstrate, that methionine (Met) does not inhibit the formation of β-sheet structures for 35MVGGVVIA42 and therefore the aberrant aggregation behavior of 37GGVVIA42 (Abeta 42 fragment) in contrast to 35MVGGVV40 (Abeta 40 fragment) arises due to the last two amino acids Ile and Ala.

6.2.4 C-terminal Fragment - 36VGGVVI41

To determine which of these two amino acids (Ile or Ala) play the more important role for the aggregation the respective hexapeptide, shifted by one amino acid (36VGGVVI41) was investigated. The peptide was dissolved in H2O/MeOH (1:1, v/v) to the final concentration of 5 mM, and FT-IR spectra were measured after different incubation times (shown in Figure 35).
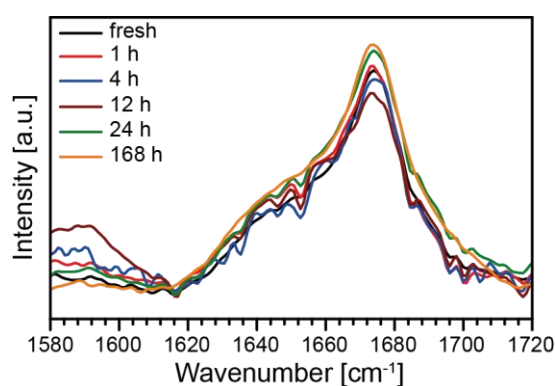
Figure 35: FT-IR spectra showing the amide I region of the 36VGGVVI41 peptide (5 mM in D2O/MeOD, 1:1, v/v) incubated for different times at room temperature. One feature at around ~1675 cm⁻¹ was observed without any changes in the intensity over time.

The FT-IR spectra show only one broad feature at ~1675 cm⁻¹ and are similar to the spectra of the non-aggregating 35MVGGVV40 peptide. This observation further supports the previous

data, which showed that Met does not necessarily inhibit the aggregation behavior and instead amyloid fibrils are only formed due to the presence of the last two amino acids Ile and Ala. For ₃₆VGGVVI₄₁, three peaks at *m*/*z* 543, 815, and 1086 are observed in the mass spectrum (Figure 36, left panel). The IM-MS analysis further revealed the presence of higher oligomers, which experimental CCSs follow the expected isotropic growth behavior (Figure 36, right panel). The observed doubly charged tetramer (n/z = 4/2+) and pentamer (n/z = 5/2+), however, exhibit an extended and compact conformation. As previously discussed, extended conformations can represent either structured aggregates or *Coulomb*-induced unfolded species.
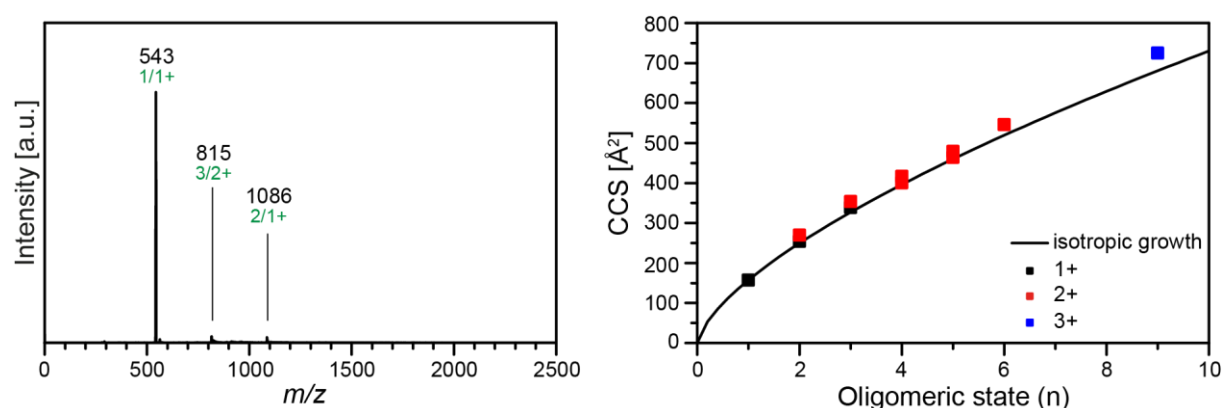
Figure 36: Left panel: MS of ₃₆VGGVVI₄₁. Peaks are labeled with their n/z (green) and *m*/*z* ratio (black). Right panel: Experimental CSS *versus* oligomeric state (n). The black line describes the ideal isotropic growth.

The secondary structure of individual oligomers was investigated by gas-phase spectroscopy and a deconvolution of the amide I band (Figure 37). No XRD-data are available for this peptide and therefore a possible, parallel β-sheet structure was assumed for the deconvolution process to avoid an overestimation of the β-sheet content. The deconvolution procedure shows that singly charged ₃₆VGGVVI₄₁ oligomers of one to three subunits do not contain β-sheets. Interestingly, an additional feature around ~1640 cm⁻¹ was observed for the doubly-charged oligomers n/z = 3/2+ and 5/2+. The deconvolution analysis indicates a β-sheet IR fraction of up to 14 %. More extended conformations are expected to exhibit higher β-sheet content then their compact isoforms. Although these oligomers show IR features, which are indicative for a small β-sheet content, they adopt very compact structures (experimental CCSs close to the isotropic growth values). Thus, these oligomers presumably will not exhibit a highly structured

steric-zipper conformation and instead form non-specific oligomers, similar to one previously shown amylolidogenic sequence (VEALYL).[3]
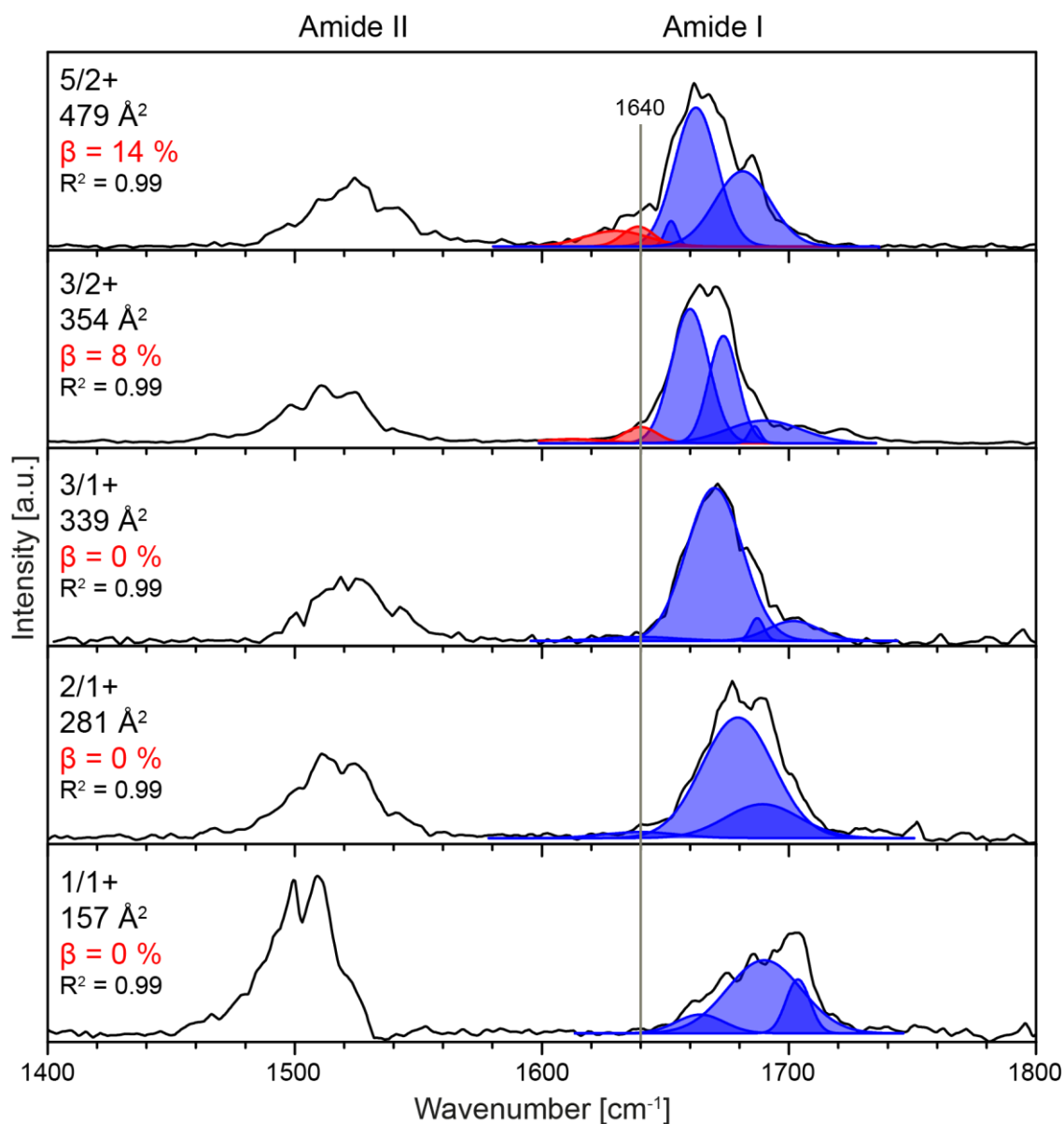
Figure 37: IRMPD spectra of the measured $_{36}$VGGVVI$_{41}$ oligomers. The amide I region was fitted with multiple *Gaussians*. Each representing an individual secondary structure motif. β-sheet (1610 - 1640 cm^{-1}) motifs are red and other structural motifs blue. The accuracy of the fits is given in R^2.

The results of $_{36}$VGGVVI$_{41}$ indicate that alanine (Ala) plays the major role for the aggregation behavior and therefore might also be responsible for the toxicity of Abeta 42.

6.3 The Full-Length Abeta-Peptides

The previously discussed results on short Abeta fragments account for differences for the aggregation behavior of full-length Abeta peptides. It is, however, also important to understand the involved structures of the full-length oligomers as well as its monomeric conformation. The monomer is the first structure, which is involved in the entire aggregation cascade. Therefore, the previously discussed methods were employed to obtain structural details of the monomer and a few dimers of the Abeta peptides. Both full-length Abeta peptides form amyloid fibrils composed of parallel β-strands at buffered conditions (pH = 7.4).[78-80] TEM images of Abeta 40 and 42 fibrils are shown in Figure 38. To compare the obtained results of the investigated Abeta fragments with the full sequence of it, both Abeta 40 and 42 were investigated.
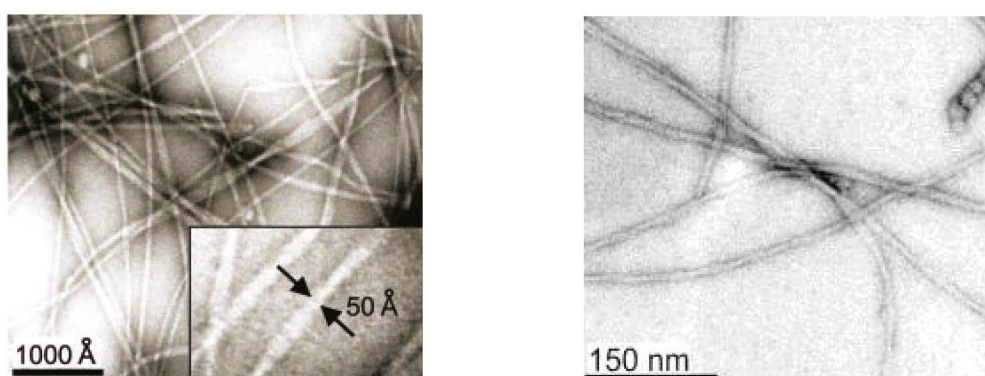
Figure 38: Left panel: TEM of negatively stained Abeta 40 fibrils after 14-day incubation of an aqueous 0.5 mM sample solution, adopted by Petkova ET AL. [79, 80] Right panel: TEM image of negatively stained Abeta 42 fibrils 0.5 mM aqueous sample solution adopted by Antzutkin ET AL.[79] Both samples were incubated in buffered conditions at pH = 7.4.

In this thesis, Abeta was therefore measured in buffered conditions (ammonium acetate, 10 mM, pH ~7) at a concentration of 50 μM. These conditions provide a spray-able sample solution with a physiologic pH value. To avoid rapid aggregations, both samples were cooled during the experiments. FT-IR spectra of the samples were not measured, because the sample concentration was too low and the peptides aggregate immediately at higher concentrations. Instead, early Abeta intermediates were investigated *via* IM-MS and gas-phase IR spectroscopy.
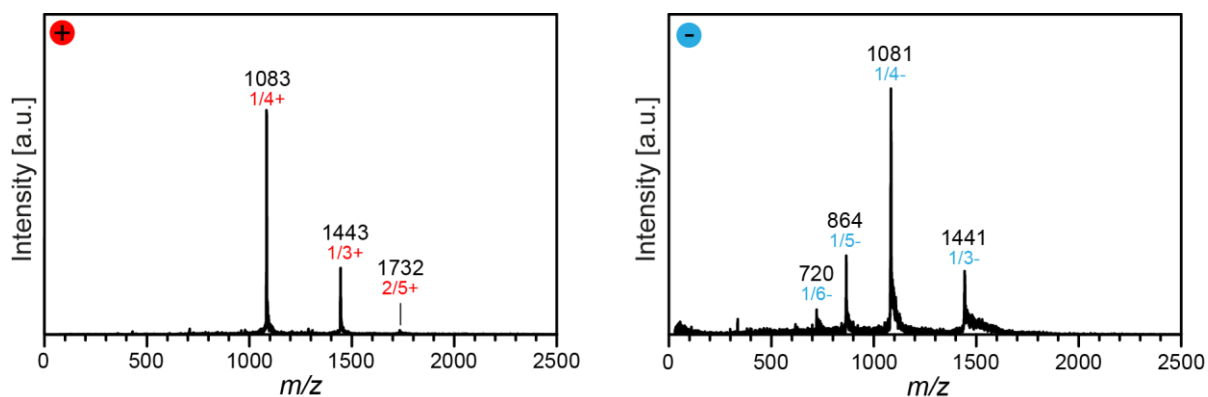
Figure 39: Mass spectrum of the Abeta 40 peptide in the positive mode (red) as well as the negative mode (blue). For the negative mode, more species with higher charge states were observed. The samples (50 µM) were sprayed from aqueous ammonium acetate solution (10 mM).

Both samples were sprayed in the positive as well as the negative ionization mode. At first, the Abeta 40 peptide was investigated and its MS spectra in both ionization modes are shown in Figure 39. Especially under neutral conditions (pH ~7.0) it is assumed that Abeta 40 occurs favorably in negative charge states. Thus, it was recently investigated in the negative ionization mode.[4, 65] For these conditions, higher oligomeric states were observed up to the tenfold charged tetramer (4/10-). In addition, also different charge states were observed (z = 2- , 3-, 4-) for the Abeta 40 monomer.[4] As shown in Figure 39 (right panel), higher oligomers were not observed, but monomers in higher charge-states. These higher charge states are typically for denatured peptides. Interestingly, in the positive ionization mode the charge-distribution pattern in the MS (Figure 39, left panel) is, especially for the monomers, similar to the reported MS in negative ion mode.[4] Due to the complexity of the peptides and their polymorph characteristics, the ATDs are rather broad. This makes the discrimination of different conformers as well as the estimation of discrete CCS values challenging. However, to give a size range for the respective conformations, the time-axis (x-axis) was converted into a CCS axis (Figure 40). In the positive ionization mode, the triply charged monomer shows one conformation (~629 Å^2), whereas the quadruply charged species show three different conformers in a CSS range between ~610 to ~740 Å^2. For the quintuply charged dimer (2/5+), the ATD plot also suggests one conformer (~1023 Å^2). In the negative mode, three charge states were observed for the monomer (right panel), whereby the triply and quintuply charge state each exhibit one conformer (red and green). The quadruply charged monomer (blue), however, shows at least three different conformers in a CCS range of ~620 Å^2 to ~800 Å^2, which is similar to the positive mode.
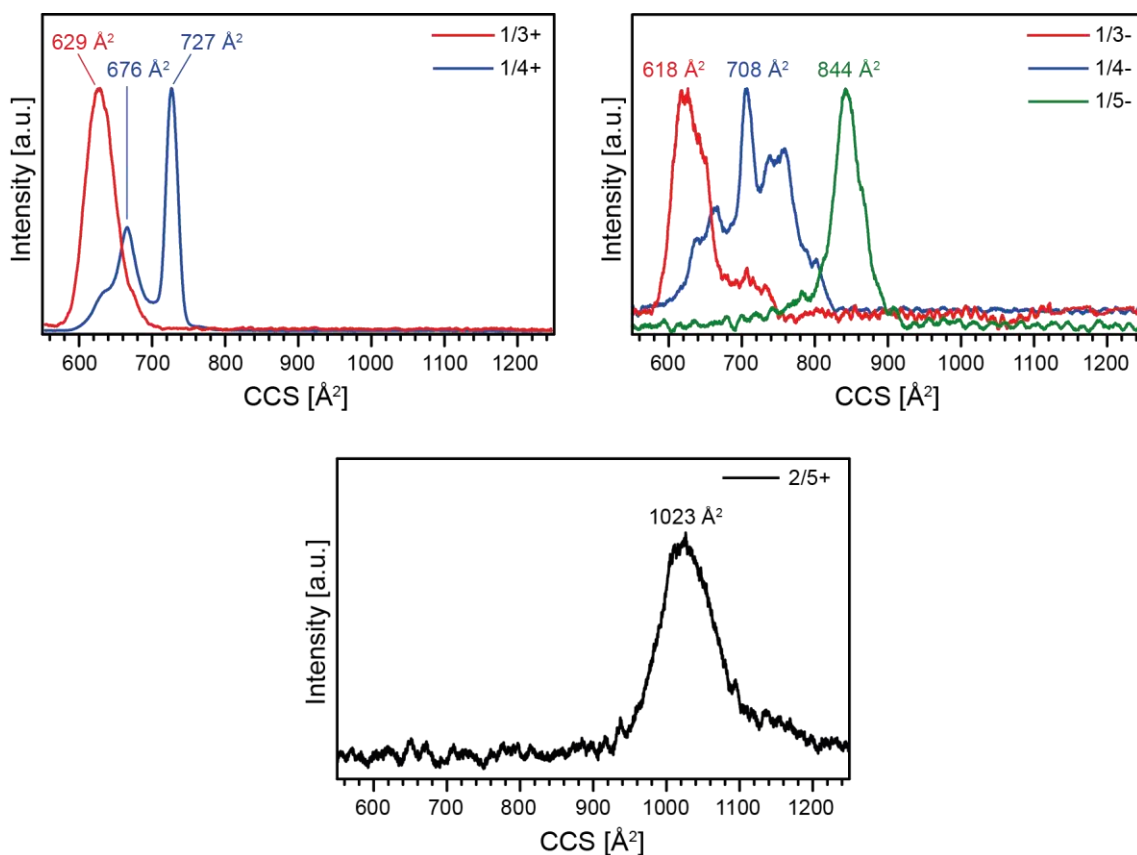
Figure 40: ATDs of the Abeta 40 species. Due to the polymorphic character of Abeta 40, the time axis was transformed into a CCS axis. The CCS for the highest intensities are labeled.

Independent from the ionization mode, the ATDs of the triply charged monomers are similar (red). Furthermore, the main conformers of the quadruply charged monomers are also in good agreement. This indicates a similar overall structure which is independent from the net charge (positive or negative). The determine CCS values are in good agreement with previously reported values.[4] Additionally, the CCS of the monomers increased with higher charge state. This increase might be caused due to a charge-induced unfolding which leads to non-native structures, such as 1/5- and 1/6-. The IM-MS analysis only provides information on the tertiary level, whereas secondary structure information is obtained by gas-phase IR spectroscopy (Figure 41).
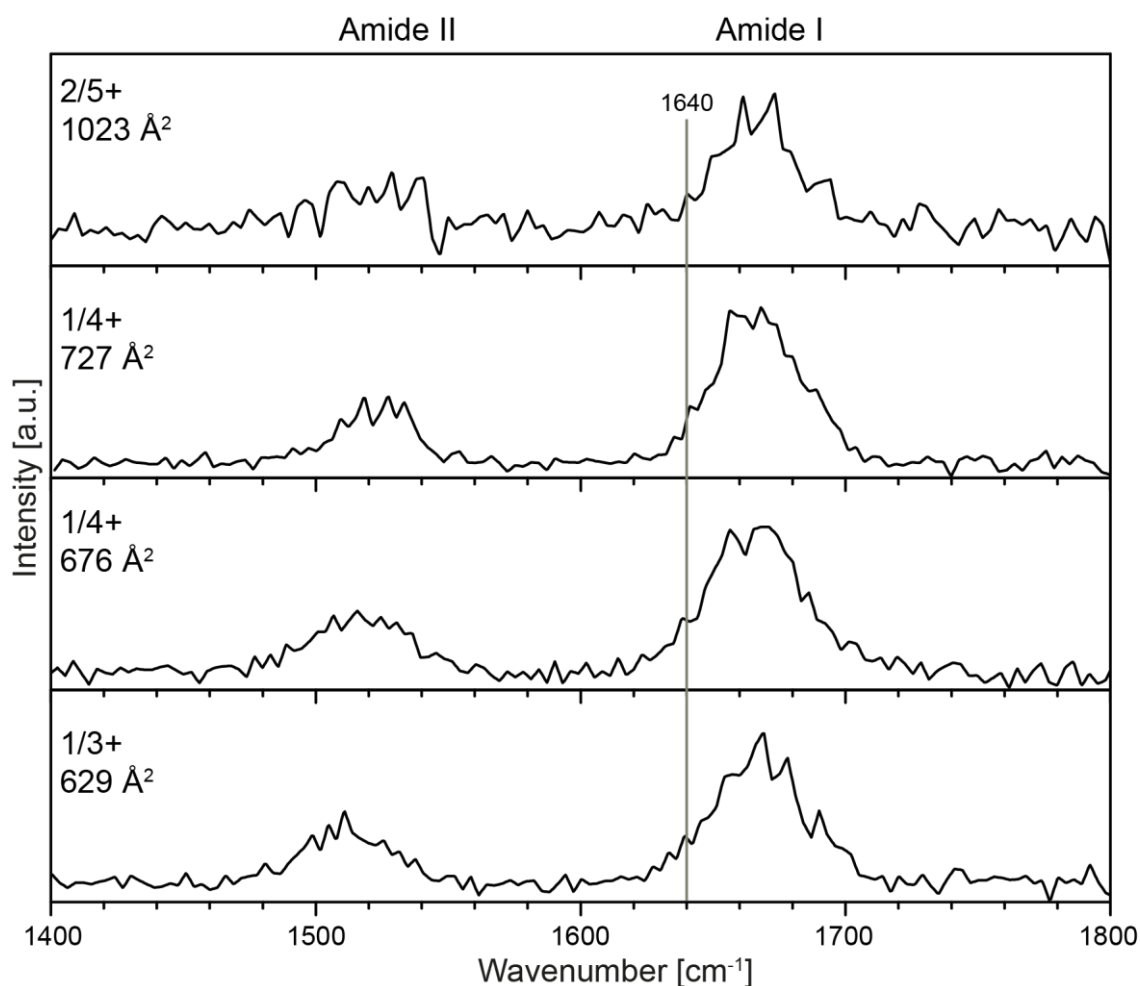
Figure 41: Depiction of the IRMPD spectra of the measured Abeta 40 oligomers. All measured spectra are similar and do not show features around 1640 cm^{-1}, which would be characteristic for β-sheet motif.

The spectra of the measured Abeta 40 species are all very similar and do not depend on the respective charge-state. The amide I and II band are observable at ~1670 and ~1520 cm^{-1} respectively. Although a possible back folding of the C-terminus is reported[51] leading to the formation of a parallel β-sheet motif for the monomer[74], no abundant amine I feature at around 1610 - 1640 cm^{-1} is observed. Thus, the here investigated Abeta 40 monomers and dimer adopt turn-like conformations.

The mass spectra (MS) in the positive as well as negative mode for Abeta 42 are shown in Figure 42. In positive mode, monomers with a charge state from three to five were observed, whereas in negative mode only the triply and quadruply charged monomers were observed. Especially for the MS in the negative ionization mode, oligomeric states up to the dodecamer (12/30-) are reported for Abeta 42, which could not be reproduced with the instrument used for this study.[4]
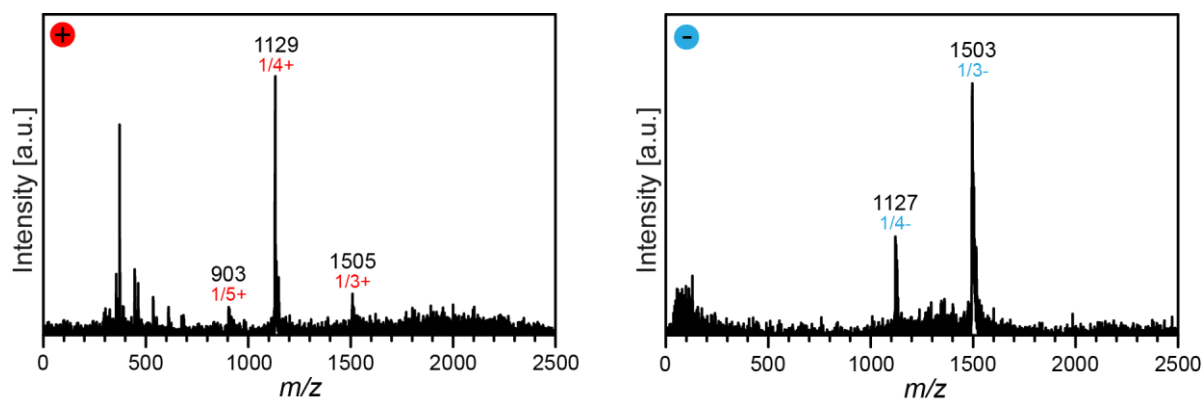
Figure 42: Mass spectra of the Abeta 42 peptide in the positive mode (red) as well as the negative mode (blue). The sample (50 μM) was each sprayed from aqueous ammonium acetate solution (10 mM).

As for Abeta 40, triply and quadruply charged monomers were detected in both ionization modes. Additionally, a quintuply charged monomer was present in the positive mode. In general, also for Abeta 42 multiple conformations for the same oligomeric state are observed (Figure 43). They show a similar tendency as Abeta 40 monomers, but they are larger in size due the two additional amino acids isoleucine (Ile) and alanine (Ala). In contrast to recently reported results[4, 65], only monomers and no higher oligomeric states of Abeta 42 were observed.
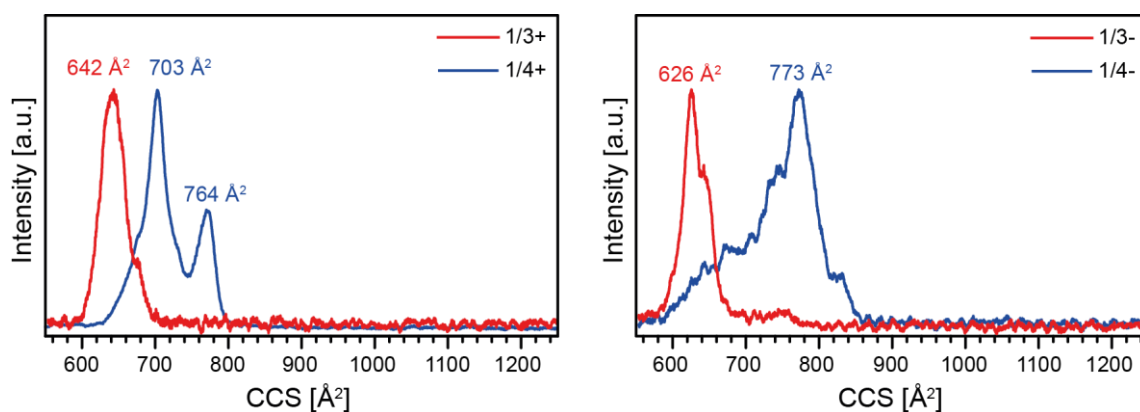
Figure 43: ATD plots of the observed Abeta 42 species. Due to the polymorphic character, the time axis was transformed into a CCS axis, to give a CCS range for it. The CCS for the highest intensities are labeled.

The Abeta 42 monomer IRMPD spectra (positive mode) are shown in Figure 44. Usually, the amide II band is lower in intensity compared to the amide I band. Due to generally low intensity in the spectra and therefore low intense fragments, the amide II band is not readily observable under the noisy baseline. The amide I position (~1665 cm⁻¹) points towards the formation of turn-like, unordered monomers, similar to the Abeta 40 monomers. Since both

Abeta peptides (Abeta 40 and 42) show similar gas-phase IR monomer spectra, they likely adopt very similar monomer conformations. The last two additional residues (Abeta 42) therefore do not have a significant influence on the tertiary structure (similar CCS values) as well as secondary structure level (similar IR spectra). However, the two additional amino acids in the Abeta 42 sequence might be responsible for a variety of new interactions within Abeta 42 oligomers. Those interactions can in turn lead to new structured aggregates and account for the faster aggregation of Abeta 42 into highly ordered amyloid fibrils.
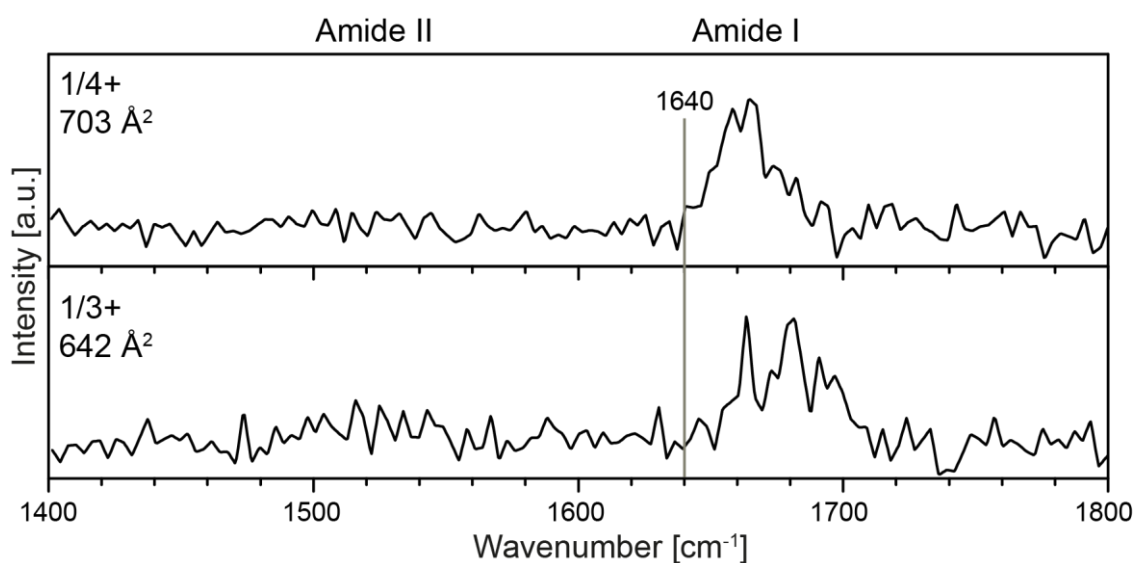
Figure 44: IRMPD spectra of Abeta 42 monomers. The spectra are similar and did not shown a β-sheet motif (band below 1640 cm^{-1}). Due to the low intensity during the measurement, the spectra have a low signal-to-noise ratio and the amide II bands are hidden in the noisy background.

7. Conclusion

Alzheimer´s disease is the second widespread disease in the Western world. A hallmark of the disease is the misfolding and aggregation of unstructured Abeta 42 monomers into highly β-sheet rich amyloid fibrils. The aggregation pathway and the oligomeric structures are, however, barely understood. Previous H/D exchange studies, which rely on the solvent accessibility, have shown that the central hydrophobic core as well as the C-terminus of Abeta 42 undergo almost no H/D exchange during the aggregation cascade. Thus, those domains are involved in strong hydrogen bonds and are major driving factors for the assembly into β-sheet rich structures. In this thesis, a hydrophobic core fragment and several fragments derived from the C-terminus of Abeta were investigated using traditional condensed-phase and elaborated gas-phase methods. The here applied condensed-phase methods show that during the aggregation the hydrophobic core fragment $_{16}$KLVFFAE$_{22}$ forms high β-sheet containing species. Surprisingly, the gas-phase data only reveal the presence of spherical, unstructured aggregates for oligomers (n = 1-10). This discrepancy might be a result of an insufficient transition of larger, probably β-sheet rich and fast-aggregating oligomers from the solution into the gas phase.

The C-terminal peptide $_{37}$GGVVIA$_{42}$, derived from the last six amino acids of Abeta 42, shows the formation of β-sheet rich species in solution. This observation agrees with the gas-phase data, indicating the presence of extended and more structured conformations for oligomers as small as four to nine subunits. On the other hand, the hexapeptide $_{35}$MVGGVV$_{40}$, which represents the last six amino acids of Abeta 40, shows only amide I features, representing unordered/turn-like structures. This is also further supported by the gas-phase data, which indicate that only compact, unstructured, spherical aggregates are formed by $_{35}$MVGGVV$_{40}$. Consequently, the last two amino acids (isoleucine and alanine) have a huge influence on the aggregation characteristics of the Abeta 42 peptide. It is, however, reported that oxidized methionine (Met 35) can inhibit the Abeta fibril formation.[77] In order to exclude an inhibition effect of the methionine residue, the $_{35}$MVGGVV$_{40}$ peptide was extended by the last two amino acids of Abeta 42 ($_{35}$MVGGVVIA$_{42}$). The FT-IR spectra of this octapeptide still shows the presence of highly, β-sheet rich intermediates, which are formed during the incubation time. In fact, $_{35}$MVGGVVIA$_{42}$ aggregates significantly faster than the shorter $_{35}$MVGGVV$_{40}$ and as a

result, no oligomers are transferred into the gas phase. This result further supports, that the last two amino acids and not the methionine residue are crucial for the formation of structured aggregates.

To determine which of both amino acids is the main actor for the Abeta 42 aggregation, the hexapeptide $_{36}$VGGVVI$_{41}$, which does not contain the alanine residue (Ala 42), were investigated. The condensed-phase as well as the gas-phase data reveal that $_{36}$VGGVVI$_{41}$ only forms compact, spherical unstructured aggregates. Thus, only the last alanine (Ala 42) residue or the combination of both isoleucine (Ile 41) and alanine (Ala 42) are crucial for the aggregation into amyloid fibrils. The Ile 41 residue is not sufficient to trigger the aggregation cascade of the Abeta 42 peptide. Table 3 shows an overview of the obtained data of all peptide fragments.

Table 3: Overview of the IM-MS and FT-IR data for all C-terminal fragments. The presence of extended oligomers (IM-MS) and β-sheet structures (FT-IR) is indicated by a "+", whereas unstructured aggregates are represented by a "-".

IM-MS (growth trend)	Peptide		FT-IR (β-sheet content)
no data	$_{35}$MVGGVV	IA$_{42}$	++
-	$_{35}$MVGGVV$_{40}$		-
-	$_{36}$VGGVV	I$_{41}$	-
+	$_{37}$GGVV	IA$_{42}$	+

The full-length Abeta assembly starts with the formation of a dimer by association of two Abeta monomers. Thus, it is crucial to understand the involved monomer and dimer structures. A fundamental understanding might help to stabilize those structures and thereby inhibit a further oligomerization. In this thesis, it was shown that the Abeta peptides (Abeta 40 and Abeta 42) form multiple monomer conformations, while also the formation of dimers was observed for Abeta 40. The presence of multiple conformations does not depend on the applied ionization modes (positive or negative). IM-MS data reveal that all Abeta monomer conformations (Abeta 40 and Abeta 42) are similar in shape. In addition, they also exhibit a similar secondary structure. The gas-phase IR analysis of size- and mass-selected species

reveal a predominant turn-like/unordered character for Abeta monomers and Abeta 40 dimers. This is in line with previous studies, which showed that the Abeta monomer adopts an unstructured conformation in solution, whereas β-sheet rich structures are formed later in the aggregation cascade.[66]

8. Outlook

In this thesis, small hexapeptides derived from the C-terminus of Abeta 42 and Abeta 40 were investigated using traditional condensed-phase and elaborated gas-phase methods. The data supports that the last two amino acids of Abeta 42 are crucial for the fibril formation. The truncated hexapeptide $_{36}$VGGVVI$_{41}$, however, does not form β-sheet rich aggregates. Thus, either the Ala 42 residue alone or the combination of both Ile 41 and Ala 42 are major factors that trigger the aggregation of Abeta 42. Future studies, aimed at investigation of small hexapeptides with glycine substitutions (e.g. $_{37}$GGVV**G**A$_{42}$ *versus* wild type; $_{37}$GGVV**I**A$_{42}$), are required. Those studies could support that the alanine residue (Ala 42), not the combination of both amino acids (Ile and Ala), is the most important factor for the aggregation into structured oligomers.

In addition, full-length Abeta oligomers might be observed in the gas phase after an instrumental modification (improvement of ion transmission/sensitivity). This would enable the structural characterization of presumably toxic Abeta 42 dodecamers and would lay the foundation for effective drug developments.

9. References

[1]   J. T. Giurleo, X. He, D. S. Talaga, *J. Mol. Biol.* **2008**, *381*, 1332-1348.

[2]   W. Hoffmann, G. von Helden, K. Pagel, *Curr. Opin. Struct. Biol.* **2017**, *46*, 7-15.

[3]   J. Seo, W. Hoffmann, S. Warnke, X. Huang, S. Gewinner, W. Schollkopf, M. T. Bowers, G. von Helden, K. Pagel, *Nat. Chem.* **2017**, *9*, 39-44.

[4]   S. L. Bernstein, N. F. Dupuis, N. D. Lazo, T. Wyttenbach, M. M. Condron, G. Bitan, D. B. Teplow, J. E. Shea, B. T. Ruotolo, C. V. Robinson, M. T. Bowers, *Nat. Chem.* **2009**, *1*, 326-331.

[5]   M. R. Sawaya, S. Sambashivan, R. Nelson, M. I. Ivanova, S. A. Sievers, M. I. Apostol, M. J. Thompson, M. Balbirnie, J. J. Wiltzius, H. T. McFarlane, A. O. Madsen, C. Riekel, D. Eisenberg, *Nature* **2007**, *447*, 453-457.

[6]   B. T. Ruotolo, J. L. Benesch, A. M. Sandercock, S. J. Hyung, C. V. Robinson, *Nat. Protoc.* **2008**, *3*, 1139-1152.

[7]   T. Wyttenbach, N. A. Pierson, D. E. Clemmer, M. T. Bowers, *Annu. Rev. Phys. Chem.* **2014**, *65*, 175-196.

[8]   A. J. Heck, *Nat. Methods* **2008**, *5*, 927-933.

[9]   C. Uetrecht, R. J. Rose, E. van Duijn, K. Lorenzen, A. J. Heck, *Chem. Soc. Rev.* **2010**, *39*, 1633-1655.

[10]   S. Warnke, Ph. D. thesis, Freie Universität Berlin (Berlin), **2015**.

[11]   W. Hoffmann, Master thesis, Freie Universität Berlin (Berlin), **2015**.

[12]   J. D. Sipe, A. S. Cohen, *J. Struct. Biol.* **2000**, *130*, 88-98.

[13]   Friedreich, Kékulé, *Virchows Arch.* **1859**, *16*.

[14]   M. P. Langevin, *Ann. Chim. Phys.* **1905**, *8*, 245-288.

[15]   M. P. Langevin, *Ann. Chim. Phys.* **1903**, *7*, 289-384.

[16]   M. Jucker, Hertie-Institut für klinische Hirnforschung (HIH) Zentrum für Neurologie, Universitätsklinikum Tübingen, Tübingen, **2014**.

[17]   D. Eisenberg, M. Jucker, *Cell* **2012**, *148*, 1188-1203.

[18]   W. T. Astbury, W. A. Sisson, *Proc. R. Soc. A* **1935**, *150*, 533-551.

[19]   L. A. Woods, S. E. Radford, A. E. Ashcroft, *Biochim. Biophys. Acta* **2013**, *1834*, 1257-1268.

[20]   P. Arosio, T. P. Knowles, S. Linse, *Phys. Chem. Chem. Phys.* **2015**, *17*, 7606-7618.

[21]   R. V. Pappu, X. Wang, A. Vitalis, S. L. Crick, *Arch. Biochem. Biophys.* **2008**, *469*, 132-141.

[22]   D. Zhu, J. Shang, X. Ye, J. Shen, *Sci. Rep.* **2016**, *6*, 39124-29134.

[23]   L. S. Wolfe, M. F. Calabrese, A. Nath, D. V. Blaho, A. D. Miranker, Y. Xiong, *Proc. Natl. Acad. Sci. U.S.A.* **2010**, *107*, 16863-16868.

[24]   M. Biancalana, S. Koide, *Biochim. Biophys. Acta* **2010**, *1804*, 1405-1412.

[25]   R. Nelson, M. R. Sawaya, M. Balbirnie, A. O. Madsen, C. Riekel, R. Grothe, D. Eisenberg, *Nature* **2005**, *435*, 773-778.

[26]   Y. Xiao, B. Ma, D. McElheny, S. Parthasarathy, F. Long, M. Hoshi, R. Nussinov, Y. Ishii, *Nat. Struct. Mol. Biol.* **2015**, *22*, 499-505.

[27]   M. A. Walti, F. Ravotti, H. Arai, C. G. Glabe, J. S. Wall, A. Bockmann, P. Guntert, B. H. Meier, R. Riek, *Proc. Natl. Acad. Sci. U.S.A.* **2016**, *113*, E4976-4984.

[28]   J. S. Schreck, J. M. Yuan, *Int. J. Mol. Sci.* **2013**, *14*, 17420-17452.

[29]   K. Tsemekhman, L. Goldschmidt, D. Eisenberg, D. Baker, *Protein Sci.* **2007**, *16*, 761-764.

[30]   T. Luhrs, C. Ritter, M. Adrian, D. Riek-Loher, B. Bohrmann, H. Dobeli, D. Schubert, R. Riek, *Proc. Natl. Acad. Sci. U.S.A.* **2005**, *102*, 17342-17347.

[31]   N. Carulla, G. L. Caddy, D. R. Hall, J. Zurdo, M. Gairi, M. Feliz, E. Giralt, C. V. Robinson, C. M. Dobson, *Nature* **2005**, *436*, 554-558.

[32]   J. Hofmann, H. S. Hahm, P. H. Seeberger, K. Pagel, *Nature* **2015**, *526*, 241-244.

[33]   R. Cumeras, E. Figueras, C. E. Davis, J. I. Baumbach, I. Gracia, *Analyst* **2015**, *140*, 1376-1390.

72

[34]   P. Atkins, J. d. Paula, *Physical Chemistry for the Life Sciences*, Freeman and Company, New York, **2006**.

[35]   R. Chang, *Physical Chemistry for the Biosciences*, University Science Books, Sausalito, **2005**.

[36]   E. Mack, *J. Am. Chem. Soc.* **1925**, *47*, 2468-2482.

[37]   G. Kaur-Atwal, G. O'Connor, A. A. Aksenov, V. Bocos-Bintintan, C. L. Paul Thomas, C. S. Creaser, *Int. J. Ion Mobil. Spectrom.* **2009**, *12*, 1-14.

[38]   C. Lapthorn, F. Pullen, B. Z. Chowdhry, *Mass Spectrom. Rev.* **2013**, *32*, 43-71.

[39]   K. Pagel, E. Natan, Z. Hall, A. R. Fersht, C. V. Robinson, *Angew. Chem. Int. Ed. Engl.* **2013**, *52*, 361-365.

[40]   T. D. Do, N. E. de Almeida, N. E. LaPointe, A. Chamas, S. C. Feinstein, M. T. Bowers, *Anal. Chem.* **2016**, *88*, 868-876.

[41]   C. Bleiholder, N. F. Dupuis, T. Wyttenbach, M. T. Bowers, *Nat. Chem.* **2011**, *3*, 172-177.

[42]   P. R. Kemper, N. F. Dupuis, M. T. Bowers, *Int. J. Mass spectrom.* **2009**, *287*, 46-57.

[43]   S. Warnke, J. Seo, J. Boschmans, F. Sobott, J. H. Scrivens, C. Bleiholder, M. T. Bowers, S. Gewinner, W. Schollkopf, K. Pagel, G. von Helden, *J. Am. Chem. Soc.* **2015**, *137*, 4236-4242.

[44]   J. Oomens, B. G. Sartakov, G. Meijer, G. Von Helden, *Int. J. Mass spectrom.* **2006**, *254*, 1-19.

[45]   B. Lucas, G. Gregoire, J. Lemaire, P. Maitre, F. Glotin, J. P. Schermann, C. Desfrancois, *Int. J. Mass spectrom.* **2005**, *243*, 105-113.

[46]   N. C. Polfer, J. Oomens, *Mass Spectrom. Rev.* **2009**, *28*, 468-494.

[47]   J. M. J. Madey, *J. Appl. Phys.* **1971**, *42*, 1906.

[48]   S. G. Biedron, W. Schöllkopf, S. Gewinner, H. Junkes, A. Paarmann, G. von Helden, H. Bluem, A. M. M. Todd, *The new IR and THz FEL facility at the Fritz Haber Institute in Berlin, Vol. 9512*, **2015**.

[49]   The FHI free-electron laser (FEL) facility, http://fel.fhi-berlin.mpg.de/, **2017**, Access: 20.02.2017.

[50]   M. Hesse, H. Meier, B. Zeeh, *Spektroskopische Methoden in der organischen Chemie, Vol. 8*, Georg Thieme Verlag KG, Stuttgart, **2012**.

[51]   M. Ahmed, J. Davis, D. Aucoin, T. Sato, S. Ahuja, S. Aimoto, J. I. Elliott, W. E. Van Nostrand, S. O. Smith, *Nat. Struct. Mol. Biol.* **2010**, *17*, 561-567.

[52]   R. I. Litvinov, D. A. Faizullin, Y. F. Zuev, J. W. Weisel, *Biophys. J.* **2012**, *103*, 1020-1027.

[53]   M. Jackson, H. H. Mantsch, *Crit. Rev. Biochem. Mol. Biol.* **1995**, *30*, 95-120.

[54]   A. Barth, *Biochim. Biophys. Acta* **2007**, *1767*, 1073-1101.

[55]   A. Brangule, K. A. Gross, *Iop. Conf. Ser-Mat. Sci.* **2015**, *77*, 012027.

[56]   M. Prince, A. Wimo, M. Guerchet, G.-C. Ali, Y.-T. Wu, M. Prina, *Vol. 1*, Alzheimer´s Disease International (ADI), London, **2015**.

[57]   J. Hardy, D. J. Selkoe, *Science* **2002**, *297*, 353-356.

[58]   S. Lesne, M. T. Koh, L. Kotilinek, R. Kayed, C. G. Glabe, A. Yang, M. Gallagher, K. H. Ashe, *Nature* **2006**, *440*, 352-357.

[59]   A. Poling, K. Morgan-Paisley, J. J. Panos, E. M. Kim, E. O'Hare, J. P. Cleary, S. Lesne, K. H. Ashe, M. Porritt, L. E. Baker, *Behav. Brain Res.* **2008**, *193*, 230-234.

[60]   S. A. Kotler, P. Walsh, J. R. Brender, A. Ramamoorthy, *Chem. Soc. Rev.* **2014**, *43*, 6692-6700.

[61]   G. Grasso, *Mass Spectrom. Rev.* **2011**, *30*, 347-365.

[62]   L. Hong, T. M. Carducci, W. D. Bush, C. G. Dudzik, G. L. Millhauser, J. D. Simon, *J. Phys. Chem. B* **2010**, *114*, 11261-11271.

[63]   P. Faller, *Chembiochem.* **2009**, *10*, 2837-2845.

[64]   M. Y. Stepanichev, Y. V. Moiseeva, N. A. Lazareva, M. V. Onufriev, N. V. Gulyaeva, *Brain Res. Bull.* **2003**, *61*, 197-205.

[65]   M. M. Murray, S. L. Bernstein, V. Nyugen, M. M. Condron, D. B. Teplow, M. T. Bowers, *J. Am. Chem. Soc.* **2009**, *131*, 6316-6317.

[66]   Y. Zhang, D. L. Rempel, J. Zhang, A. K. Sharma, L. M. Mirica, M. L. Gross, *Proc. Natl. Acad. Sci. U.S.A.* **2013**, *110*, 14604-14609.

[67] K. Tao, J. Wang, P. Zhou, C. Wang, H. Xu, X. Zhao, J. R. Lu, *Langmuir* **2011**, *27*, 2723-2730.

[68] B. Barz, D. J. Wales, B. Strodel, *J. Phys. Chem. B* **2014**, *118*, 1003-1011.

[69] G. R. Hilton, J. L. Benesch, *J. R. Soc. Interface* **2012**, *9*, 801-816.

[70] H. Inouye, K. A. Gleason, D. Zhang, S. M. Decatur, D. A. Kirschner, *Proteins* **2010**, *78*, 2306-2321.

[71] J. P. Colletier, A. Laganowsky, M. Landau, M. Zhao, A. B. Soriaga, L. Goldschmidt, D. Flot, D. Cascio, M. R. Sawaya, D. Eisenberg, *Proc. Natl. Acad. Sci. U.S.A.* **2011**, *108*, 16938-16943.

[72] G. Zandomeneghi, M. R. Krebs, M. G. McCammon, M. Fandrich, *Protein Sci.* **2004**, *13*, 3314-3321.

[73] I. Kheterpal, K. D. Cook, R. Wetzel, *Methods Enzymol.* **2006**, *413*, 140-166.

[74] S. K. Maji, L. Wang, J. Greenwald, R. Riek, *FEBS Lett.* **2009**, *583*, 2610-2617.

[75] J. T. Berryman, S. E. Radford, S. A. Harris, *Biophys. J.* **2011**, *100*, 2234-2242.

[76] L. Zhu, M. Xu, M. Yang, Y. Yang, Y. Li, J. Deng, L. Ruan, J. Liu, S. Du, X. Liu, W. Feng, K. Fushimi, E. H. Bigio, M. Mesulam, C. Wang, J. Y. Wu, *Hum. Mol. Genet.* **2014**, *23*, 6863-6877.

[77] M. Palmblad, A. Westlind-Danielsson, J. Bergquist, *J. Biol. Chem.* **2002**, *277*, 19506-19510.

[78] A. T. Petkova, Y. Ishii, J. J. Balbach, O. N. Antzutkin, R. D. Leapman, F. Delaglio, R. Tycko, *Proc. Natl. Acad. Sci. U.S.A.* **2002**, *99*, 16742-16747.

[79] O. N. Antzutkin, R. D. Leapman, J. J. Balbach, R. Tycko, *Biochemistry* **2002**, *41*, 15436-15450.

[80] J. J. Balbach, A. T. Petkova, N. A. Oyler, O. N. Antzutkin, D. J. Gordon, S. C. Meredith, R. Tycko, *Biophys. J.* **2002**, *83*, 1205-1216.
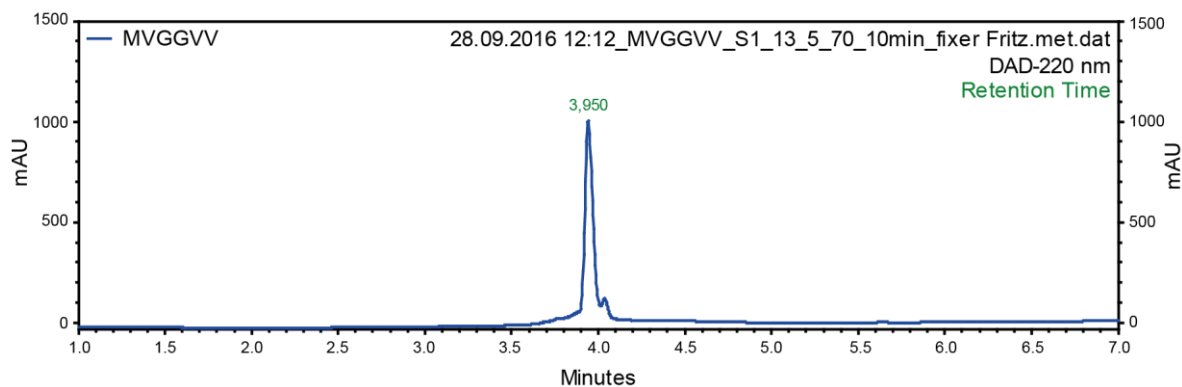
10. Appendix

## 10.1 Analytical-HPLC Chromatograms of the Purified $_{37}$GGVVIA$_{42}$ and $_{35}$MVGGVV$_{40}$ Abeta Peptides
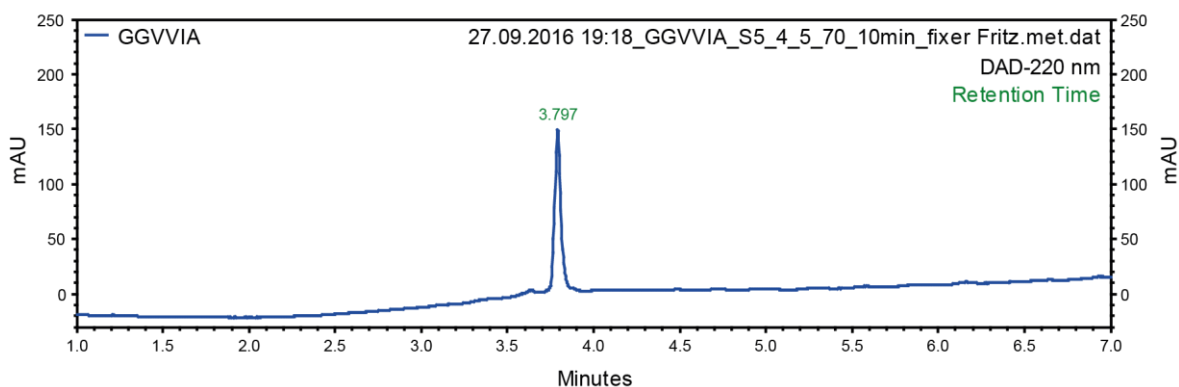
Figure 45: Analytical HPLC chromatogram of $_{37}$GGVVIA$_{42}$ after the clean-up procedure *via* preparative HPLC. A diode array detector (DAD) at 220 nm was used as detector.

**Figure 46:** Analytical HPLC chromatogram of $_{35}$MVGGVV$_{40}$ after the clean-up procedure *via* preparative HPLC. A diode array detector (DAD) at 220 nm was used as detector.

10.2 Mass spectra (MS) of the Purified 37GGVVIA42 and 35MVGGVV40 Abeta Peptides
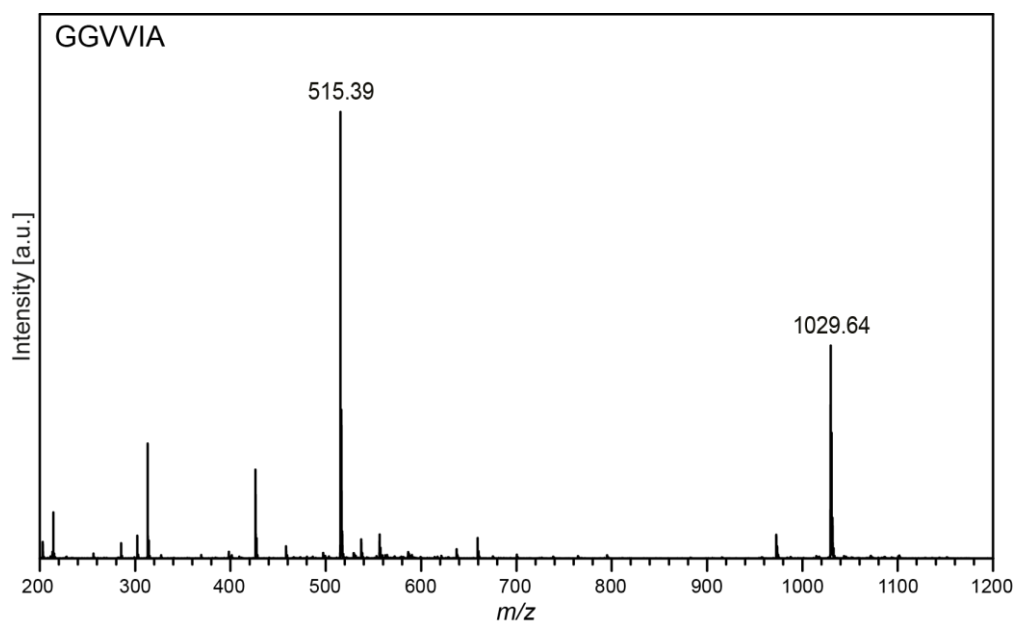
Figure 47: ESI-TOF mass spectrum (MS) in the positive mode of 37GGVVIA42 after the clean-up procedure *via* preparative HPLC. The singly charged dimer is assigned.
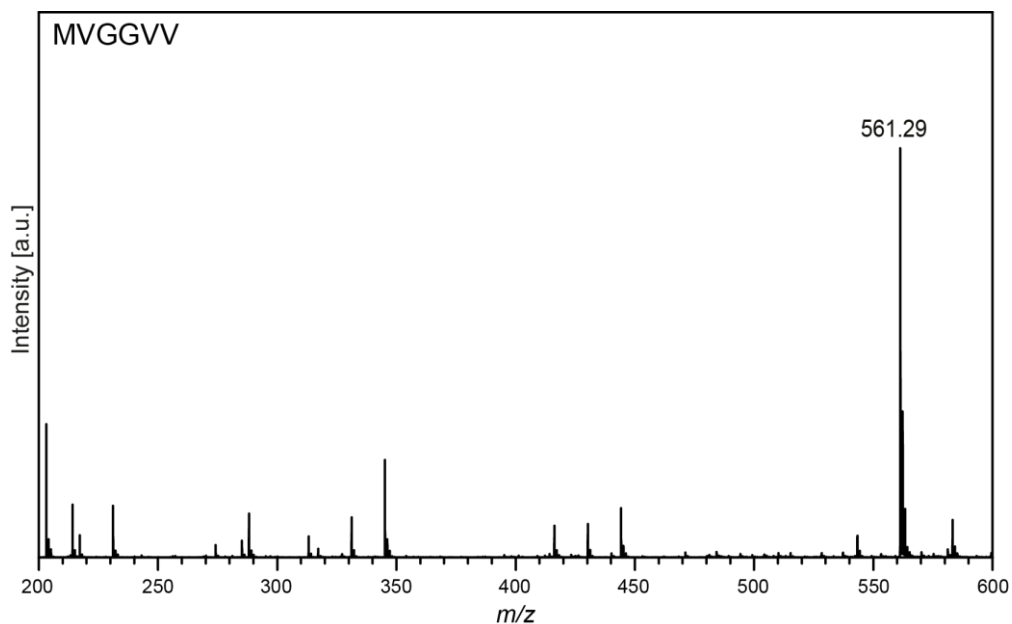
Figure 48: ESI-TOF mass spectrum (MS) in the positive mode of 35MVGGVV40 after the clean-up procedure *via* preparative HPLC.

10.3 Collision Cross Sections (CCSs) and Beta-Sheet Fractions of the Abeta Fragments

In the following, the "-" in the cells stand for "not measured".

10.3.1 $_{16}$KLVFFAE$_{22}$

Table 4: Collision cross-section (CCS) of the $_{16}$KLVFFAE$_{22}$ oligomers and their calculated β-sheet IR fraction.

n	z	CCS$_{exp.}$ [Å^2]	β-sheet fraction in amide I
1	1+	219	-
1	2+	215	-
2	1+	345	-
2	2+	343	-
2	3+	425	-
3	2+	460	0.0
3	2+	475	0.0
3	3+	494	-
4	2+	554	-
4	2+	568	-
4	3+	567	0.0
5	3+	641	0.0
5	3+	664	0.10
5	4+	671	-
6	3+	727	-
6	4+	742	-
7	3+	799	0.11
7	4+	817	0.15
8	4+	888	-
10	5+	1048	-

10.3.2 $_{37}$GGVVIA$_{42}$

Table 5: Collision cross-section (CCS) of the $_{37}$GGVVIA$_{42}$ oligomers and their calculated β-sheet IR fraction.

n	z	CCS$_{exp.}$ [Å²]	β-sheet fraction in amide I
1	1+	148	0.0
2	1+	245	0.0
3	1+	317	0.0
3	2+	339	0.09
4	2+	403	-
5	2+	460	0.07
6	2+	513	-
6	3+	528	-
6	3+	534	-
7	2+	563	0.04
7	3+	587	0.12
9	3+	673	-
10	3+	709	0.11
10	4+	752	-
12	4+	846	-
14	4+	929	-

10.3.3 $_{35}$MVGGVV$_{40}$

Table 6: Collision cross-section (CCS) of the $_{35}$MVGGVV$_{40}$ oligomers and their calculated β-sheet IR fraction.

n	z	CCS$_{exp.}$ [Å^2]	β-sheet fraction in amide I
1	1+	159	0.0
2	1+	255	0.0
3	1+	340	0.0
3	2+	348	0.12
4	2+	406	-
5	2+	473	0.0
6	2+	534	-
7	3+	591	0.12
8	3+	626	0.03
9	3+	713	-

10.3.4 $_{35}$MVGGVVIA$_{42}$

Table 7: Collision cross-section (CCS) of the $_{35}$MVGGVVIA$_{42}$ oligomers.

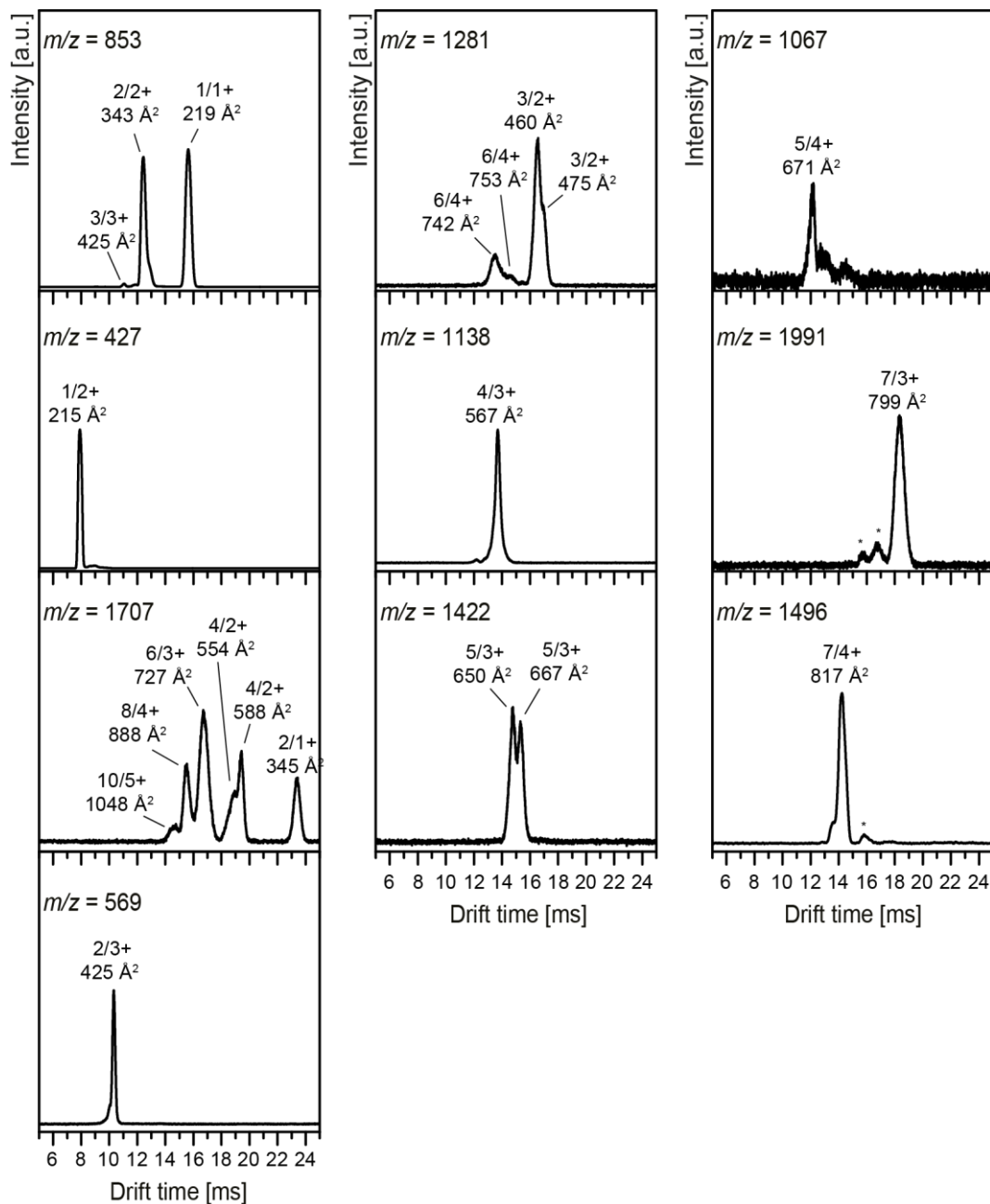| n	z	CCS$_{exp.}$ [Å^2]
1	1	194
2	2	332
2	2	343
3	3	462

10.3.5 $_{36}$VGGVVI$_{41}$

Table 8: Collision cross-section (CCS) of the $_{36}$VGGVVI$_{41}$ oligomers and their calculated β-sheet IR fraction.

| n	z	CCS$_{exp.}$ [Å^2]	β-sheet fraction in amide I
1	1	157	0.0
2	1	282	0.0
2	2	269	-
3	1	339	0.0
3	2	354	0.08
4	2	400	-
4	2	416	-
5	2	464	0.14
5	2	479	0.14
6	2	546	-
9	3	725	-

10.4 Arrival Time Distributions (ATD)

10.4.1 KLFVVAE

Figure 49: Arrival time distributions (ATDs) of the 16KLVFFAE22 oligomers and their collision cross-sections (CCSs). All ATDs are shown at the same drift voltage and were measured in helium. The asterisks (*) stands for unknown species and impurities.
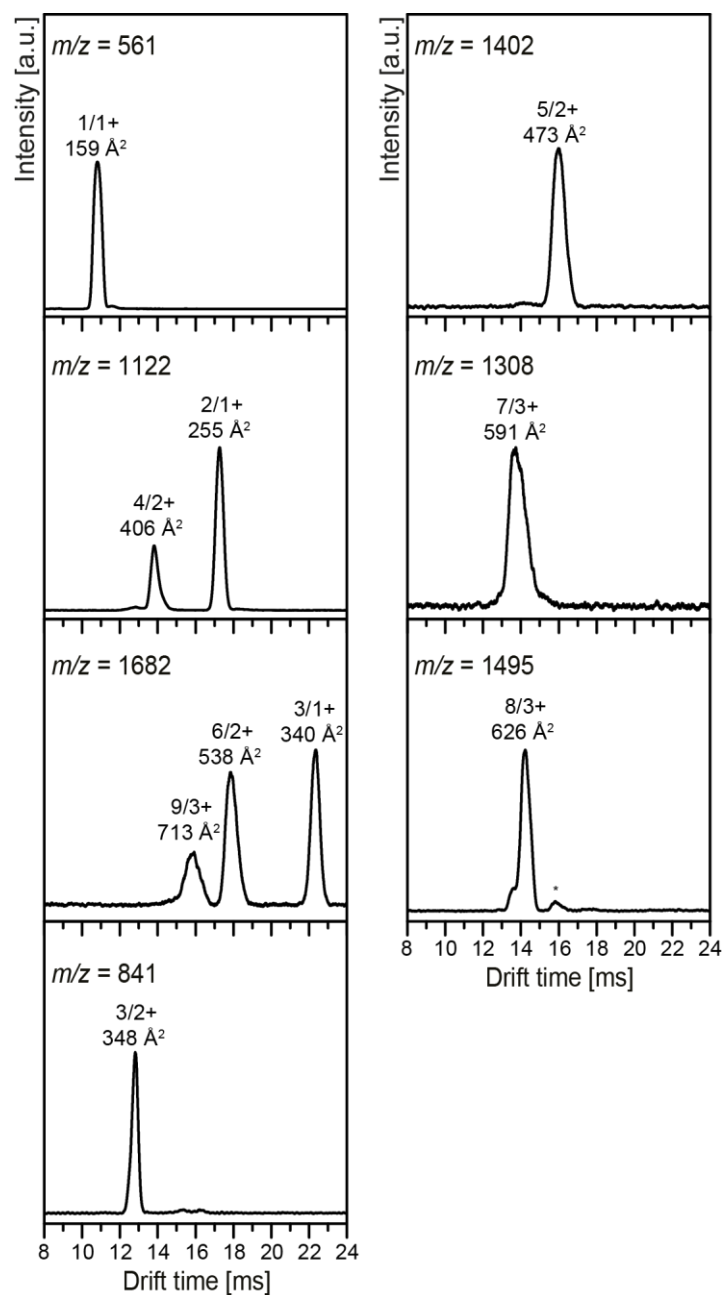
10.4.2 $_{37}$GGVVIA$_{42}$
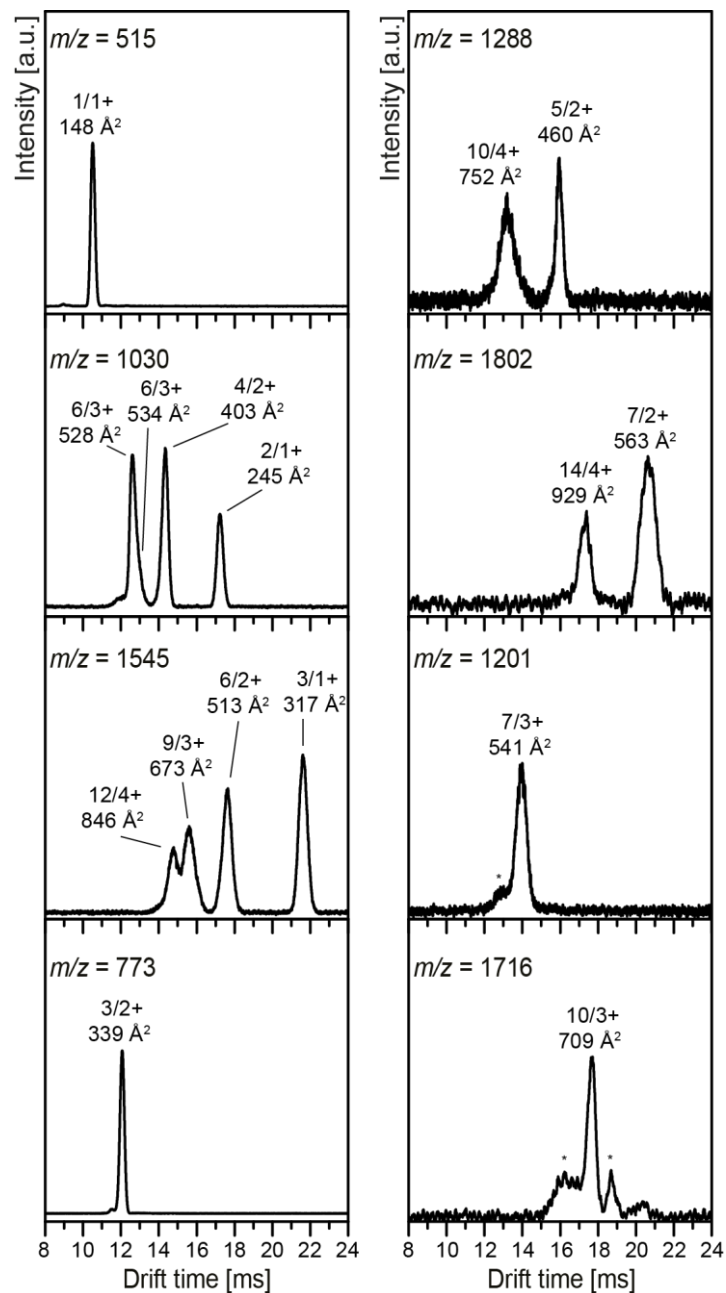
Figure 50: Arrival time distributions (ATDs) of the $_{37}$GGVVIA$_{42}$ oligomers and their collision cross-sections (CCS). All ATDs are shown at the same drift voltage and were measured in helium. The asterisks (*) stands for unknown species and impurities.
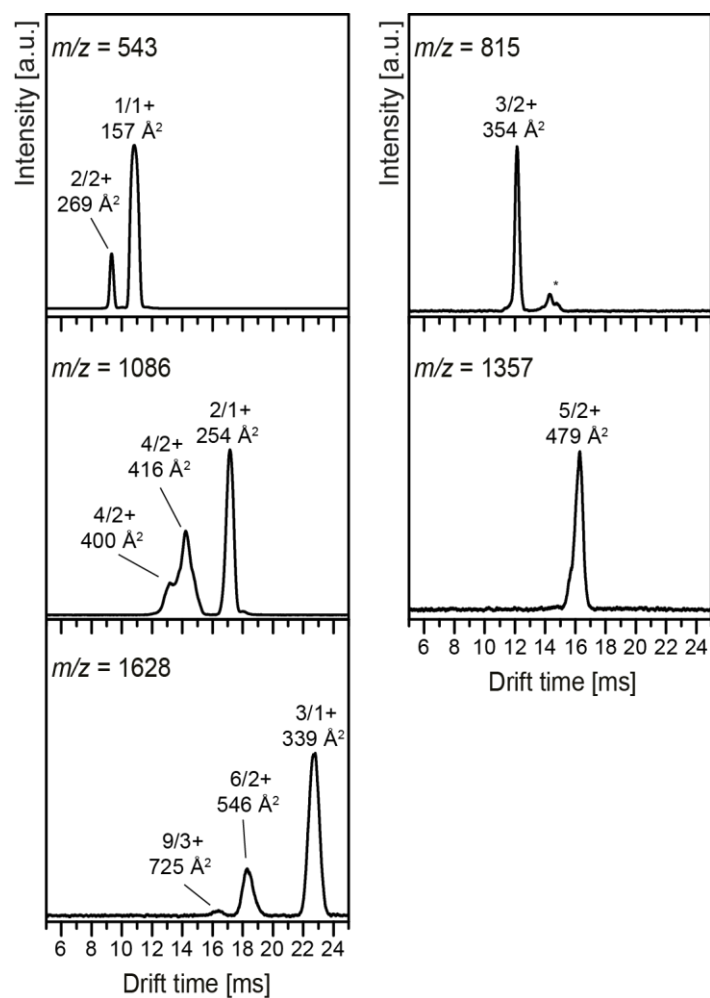
10.4.3 $_{35}$MVGGVV$_{40}$

Figure 51: Arrival time distributions (ATDs) of the $_{35}$MVGGVV$_{40}$ oligomers and their collision cross-sections (CCS). All ATDs are shown at the same drift voltage and were measured in helium. The asterisks (*) stands for unknown species and impurities.

10.4.4 36VGGVVI41

Figure 52: Arrival time distributions (ATDs) of the 36VGGVVI41 oligomers and their collision cross-sections (CCS). All ATDs are shown at the same drift voltage and were measured in helium. The asterisks (*) stands for unknown species and impurities.